NSK Technical Journal

Motion & Control

No. 28 June 2017

ISSN1342-3630

NSK

MOTION & CONTROL No. 28
NSK Technical Journal
Printed and Published: June 2017
ISSN1342-3630
Publisher: NSK Ltd., Ohsaki, Shinagawa, Tokyo, JAPAN
Public Relations Department
TEL +81-3-3779-7050
FAX +81-3-3779-7431
Editor: Hirotoshi ARAMAKI
Managing Editor: Hitoshi EBISAWA
Design, Typesetting & Printing: Kuge Printing Co., Ltd.

NSK Technical Journal

Motion & Control

No. 28

June 2017

NSK

Contents

Preface

Technical Articles

New Products

Preface

NSK Commemorates its Centennial

Hirotoshi Aramaki
Executive Vice President
NSK TECHNICAL JOURNAL Editor

NSK commemorated its centennial in November 2016. Reflecting on our anniversary, I would like to take this opportunity to express my sincere appreciation to partners, senior colleagues, and old friends who have extended their continued guidance, cooperation, and other support in the advancement of our products and R&D activities.

Our magazine *NSK BEARING JOURNAL* was first published in early 1954, a time when Japan's economy had recovered to prewar levels and its rapid economic growth was set to begin. Against this backdrop, the then president of NSK in his message in the first issue stressed the importance of analyzing, systematizing, and theorizing in various areas by forming a trinity among manufacturers, researchers, and consumers while honoring creativity and autonomy in scientific culture. The first issue of the publication included articles on bearings used in the automotive and rail sectors while also providing information about technologies that at the time were integral to the expansion of Japan's transport infrastructure. In 1985, in response to the rapidly broadening scope of our product technologies, the magazine was renamed *NSK TECHNICAL JOURNAL*, of which there have been 89 issues. The English version, *Motion & Control*, was first published in 1996 and has been printed 28 times. In those days, the publication carried with it our mission to introduce NSK's technological achievements, not only products but systematized and theorized technologies as well. Moreover, we made an effort to provide information that deepened understanding of our products and have remained committed to editing the content in such a way that it can be valuable in academic activities. Personally, I want the magazine to benefit all readers on many levels.

Since joining NSK in 1984, I have been involved primarily in R&D. In the 80s, computer technologies were being developed rapidly, but the speed of technological evolution is now faster and more diversified than ever before. We live in an era of great change, often represented by such advancements as Industry 4.0, IoT, AI, and automated driving. Conversely, we are faced with a myriad of unresolved issues across the world, including global warming, population-related problems, resource depletion, and matters affecting the supply of food. We must therefore renew our resolve in order to contribute to society through our technological innovation while at the same time continuing to share our findings with you.

Hirotoshi Aramaki

Advanced Technology for Lubricant Film Formation by Grease and Application to Improve Bearing Wear Resistance under Severe Conditions

Michita Hokao, Atsushi Yokouchi, and Katsuhiro Konno
NSK Ltd.

Abstract

The effects of thickener composition of grease on the oil film formation was investigated with optical interferometry under low speed and high load conditions. As a result, a new thickener composition of grease was revealed, which improves the oil film thickness and flow properties of grease. This knowledge was applied in the development of bearings, and under severe low speed and high load conditions as well as water contamination, the wear resistance of the bearings improved due to increased oil film thickness of the grease.

This article has been approved for reprinting by the Proceedings of JAST Tribology Conference 2013–10, A19.

1. Introduction

It has been reported that lubricant film formation by grease in rolling contacts depends not only on base oil viscosity but also on thickener, and grease cloud forms thicker lubricant film in a low speed range than lubricating oil[1]. Also, Aihara et al. reported that grease is more likely than oil to result in starved lubrication, and if grease amount is insufficient to fill the inlet conjunction, the grease film thickness will become thinner than that of the base oil film[2].

Particularly under low speed and high load conditions, more concerns may be raised about the possibility of wear due to the contact of bearing metal surfaces.

For the purpose of maintaining a thick oil film for an extended period under low speed and high load conditions, an investigation related to the effects of thickener composition of urea grease on the oil film formation under low speed and high load conditions have been undertaken.

Furthermore, this technique was applied for spherical roller bearings, which are prone to wear. A spherical roller bearing has two non-sliding pure rolling points in the contact surface, and uneven wear could occur[3]. In some steel manufacturing facilities, spherical roller bearings are exposed to water or heat during use under low speed and high load conditions, and the oil film is less likely to form sufficiently in such an environment. The evaluation results of wear resistance using spherical roller bearings is also reported on in this article.

2. Experiment

2.1 Tested grease

Table 1 shows the properties of grease used in the test. Grease A to E were prepared by mixing, at varied rates, Grease 1 and 2, which are different thickener types, so that the worked penetration became approximately 325. Grease F, which is commercially available, was used in the comparison.

Table 1 Tested greases

Grease	Base oil	Thickener	Worked penetration
1	Ether oil	Urea 1	324
2		Urea 2	330

Grease	Grease mix ratio (%)		Worked penetration
	Grease 1	Grease 2	
A	0	100	330
B	25	75	322
C	50	50	325
D	75	25	330
E	100	0	324
F	—	—	350

2.2 Test Method

2.2.1 Measurement of EHL oil film thickness

A ball-on-disk type tribometer with optical interferometry was used to measure grease film thickness. A glass disk and SUJ2 ball were used.

2.2.2 Measurement of inlet distance of grease

Inlet distance was measured to evaluate grease replenishment. Inlet distance was defined as the grease replenishment from the tip of contact ellipse to the interface of grease and air at the contact inlet that can be observed when a ball rolls on a grease-applied glass disk. The evaluation condition was set at an initial grease application thickness of 0.2 mm, a maximum Hertzian pressure of 1 GPa, a sliding ratio of 17%, and a disk rolling speed of 0.01 m/s. The minimum inlet distance was measured over a 10-minute period.

2.2.3 Measurement of degree of separation

The oil film formation in a bearing was evaluated by the capacitance method. Degree of separation was defined as the proportion of the measured voltage to the applied voltage. By using a spherical roller bearing (inner diameter ϕ25 mm × outer diameter ϕ62 mm × width 17 mm), the degree of separation was measured at 2 rpm to 50 rpm.

3. Results and Discussion

3.1 Measurement of oil film thickness

Figure 1 shows the measurement results of grease film thickness and the calculated value of the base oil using the Hamrock and Dowson film thickness formula. The film thickness of each grease at a rolling speed of 1.0 m/s to 0.04 m/s decreased in correlation with decreases in rolling speed. This was also the case for the base oil of each grease. At a rolling speed of 0.03 m/s or slower, however, the film thickness decreased in the base oil, whereas grease A to E formed thicker films than that of the base oil. At a speed of 0.003 m/s or slower, Grease F formed a thicker film than that of the base oil. A report was made on the behavior of grease that forms a thicker film than that of the base oil at a certain speed or slower, and therein thicker agglomeration passed through a contact ellipse at a lower speed range[1]. Also, in this test, thicker agglomerations were confirmed to pass through the contact area, which indicates that the thickener in each type of grease contributed to increasing the film thickness at a speed of 0.03 m/s or slower.

At a speed of 0.03 m/s or slower, Grease C, D, and E, which have Urea 1-containing Grease 1 mixed at the rate of 50% or more, formed thicker films than those of Grease A and B. It was therefore confirmed that Urea 1 contributes to increasing the film thickness more than Urea 2 at a slower speed range.

From these results, it was confirmed that Urea 1 has a greater effect on the formation of oil film thickness compared to Urea 2.

3.2 Inlet distance of grease

Figure 2 shows the measurement results of closest inlet distance. The longer the inlet distance, the more grease that is present at the inlet conjunction, which improves grease replenishment and prevents starvation. The results for Grease A to E show that the more Urea 2 containing Grease 2 is mixed, the longer the closest inlet distance becomes, and the better grease replenishment. As for Grease F, replenishment was similar to that of Grease D.

From these results it was confirmed that increased composition of Urea 2 improves grease replenishment.

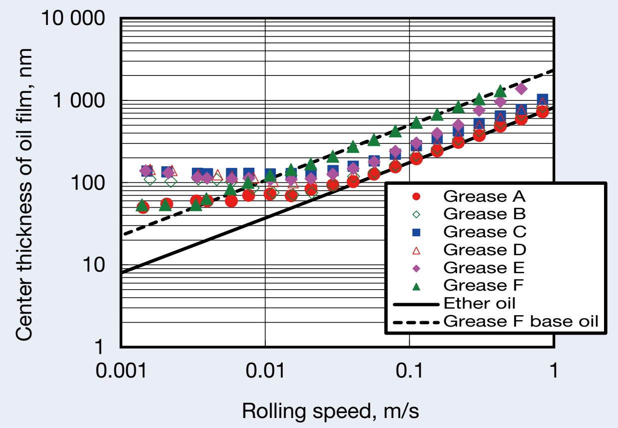

Fig. 1 Oil film thickness

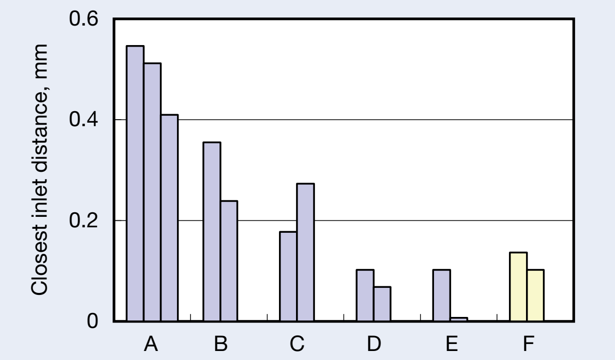

Fig. 2 Inlet distance of grease

4. Applications for Improvement of Wear Resistance

Grease C, D, and E formed thicker films than those of Grease A and B at a rolling speed of 0.03 m/s or slower, and Grease A, B, and C replenished better than Grease F. This indicates that Grease C, having formed a thicker oil film in a slow speed range with a better reflow property, is excellent in the forming of an oil film. Grease C1 was subsequently prepared by mixing additives with Grease C so that the film formation property and wear resistance of grease in the bearing could be evaluated. A test condition emulated steel manufacturing facilities, where bearings are used under low speed and high load conditions.

The measurement results for degree of separation, shown in Figure 3, indicate that the higher the separation degree, the less metal contact there is in the bearing, and a thicker oil film forms. Within a range of 50 rpm to 20 rpm, the degree of separation decreased in Grease C1 and F in step with decreases in speed. At a slower speed than this range, the degree of separation decreased to almost zero in Grease F, whereas Grease C1 showed a tendency to experience more separation as the rotating speed decreased. The assumed steel manufacturing facilities normally operate at around 10 rpm (equivalent to 0.01 m/s rotation speed), so it was determined that under this condition, Grease C1 has a better film formation property than that of Grease F. Furthermore, at 10 rpm, a combination of Grease C1 and water (30%) demonstrated a higher degree of separation compared to Grease F. It was therefore shown that Grease C1 is less likely to lose its film formation property even under a water contaminated condition.

Moreover, a spherical roller bearing (inner diameter ϕ55 mm × outer diameter ϕ100 mm × width 25 mm) was used to evaluate wear resistance. Grease was mixed with 30% water, and water was continuously fed to the bearing during an operation. Figure 4 shows the measurement results for the surface profile of the loading area of the outer ring after the test. The bearing with Grease F showed uneven wear with a maximum wear depth of 20 µm. However, for Grease C1 no such wear was observed and the maximum wear depth was 2 µm.

From these results, the improvement of oil formation by closely examining the thickener composition of grease, as well as the significant enhancement of the wear resistance of the bearing with the grease, has been confirmed.

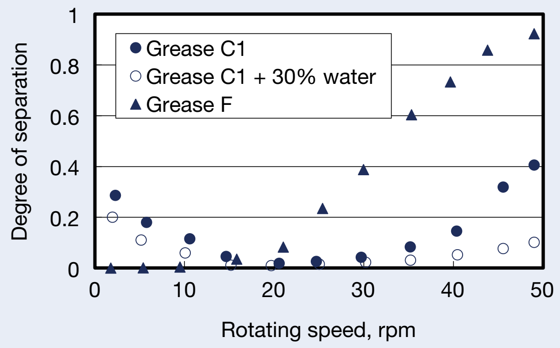

Fig. 3 Degree of separation

(a) Grease C1

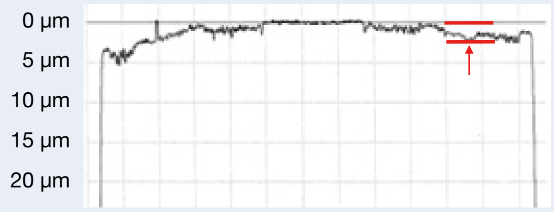

(b) Grease F

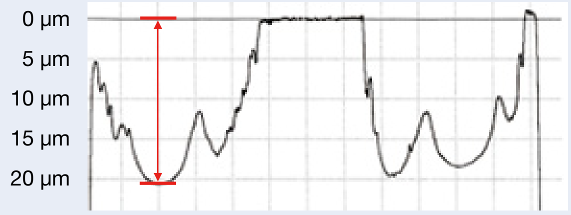

Fig. 4 Surface profile of the loading area of the outer ring

5. Conclusion

The following conclusion was obtained by ensuring the influence of the grease composition on the grease film thickness and grease replenishment.

- The composition of thickener that can improve grease film formation capacity under low speed conditions was revealed.
- The above composition of thickener improves the wear resistance of spherical roller bearings under low speed, high load, and water contaminated conditions.

6. Acknowledgment

We appreciate KYODO YUSHI CO., LTD. for the cooperation extended to this study.

References

1) Y. Kimura, T. Endo, and D. Dong, "EHL with grease at low speeds," Advanced Tribology, Proceedings of CIST 2008 & ITS-IFToMM2008 Beijing (2009) 15–19.
2) S. Aihara and D. Dowson, "An experimental study of grease film thickness under elasto-hydrodynamic conditions (Part 2) Mechanism of grease film formation," Journal of Japan society of lubrication engineers, 25-6 (1980) 379–386.
3) K. Yamamura, M. Oohori, "Development of high wear resistant SWR Bearing," NSK Technical Journal, 671 (2001) 30–34.

Michita Hokao

Atsushi Yokouchi

Katsuhiro Konno

White Structure Flaking in Rolling Bearings for Wind Turbine Gearboxes

Hiroki Yamada and Hideyuki Uyama
NSK Ltd.

Abstract

Bearing failures in wind turbine gearboxes were investigated and rolling contact fatigue tests to reproduce them using a hydrogen-charge method were conducted. Two main failure modes in wind turbine gearbox bearings were white structure flaking and axial cracking, which were involving a microstructural change. Both failure modes can be reproduced by using specimens charged with hydrogen. Operating conditions, which can induce hydrogen generation from lubricant and penetration of the bearing steel were discussed. Effects of bearing material on white structure flaking life were suggested as one of the countermeasures.

Translated and reprinted from Technical Paper 13FTM15 with the approval of the American Gear Manufacturing Association (1001 N. Fairfax Street, 5th floor, Alexandria. Virginia, USA 22314).

1. Introduction

Premature failures of rolling bearings occasionally occur in wind turbine gearboxes(1). One of the main failure modes is flaking involving a microstructural change. This type of flaking is called white structure flaking (WSF) or white etching crack (WEC) because the area of the microstructural change observed in the flaking cross sections looks white after etching. Therefore, understanding the mechanism of white structure flaking is important for wind turbine gearbox reliability.

Flaking in rolling bearings occurs due to rolling contact fatigue and it is a similar phenomenon as spalling in gears. Flaking is generally classified to subsurface originated flaking, which is initiated at nonmetallic inclusions in materials and surface originated flaking, which occurs under contaminated or poor lubrication conditions(2). However, recently white structure flaking can be seen in several applications, which is a different type of flaking from the subsurface and surface originated flaking mentioned above. For example, it is known that white structure flaking sometimes occurs in bearings for automotive electrical accessories as shown in Fig. 1(3). There are many studies about the failure mechanism and the countermeasure for white structure flaking in automotive bearings. Some of them suggested that this type of flaking is induced by hydrogen generated by decomposition of the lubricating oil, grease, or water in the lubricant and that this phenomenon is concerned with hydrogen embrittlement(4)–(11).

Axial cracks are also observed in failed bearings for wind turbine gear boxes(12). This failure mode is very unique and it is seldom found in other applications. The same microstructural change as seen in white structure flaking is often observed in the cross sections around the axial cracks.

However, it is unclear whether the mechanisms of white structure flaking and axial cracking are the same or not. In this study, rolling contact fatigue tests were performed in order to reproduce white structure flaking and axial cracking by using specimens charged with hydrogen. From the view of hydrogen theory, influencing factors in operating conditions were discussed and effects of materials on bearing life were suggested as the countermeasure.

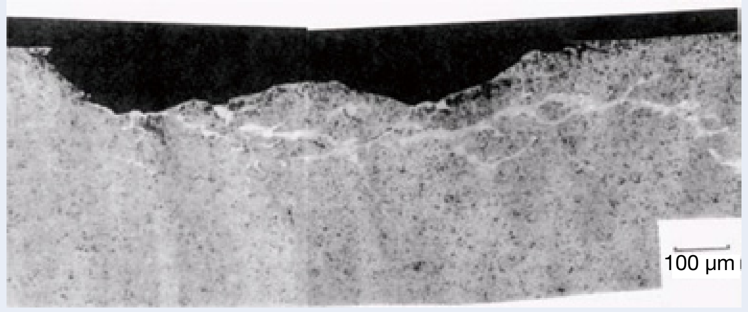

Fig. 1 An Example of the cross section of white structure flaking in an automotive electrical accessory bearing(3).

2. Observation results of failed bearings for wind turbine gearboxes

Failed bearings used in wind turbine gearboxes have been observed and two types of failures were mainly observed, which are classified as white structure flaking and axial cracking.

Figure 2 shows the observation results of a failed cylindrical roller bearing, which were used on the high speed shaft in wind turbine gearboxes. A small flaking was seen in the raceway surface as shown in Fig.2 (a). Figure 2 (b) shows the cross section of the flaking area at the dotted line in Fig. 2 (a). A microstructural change called white structure was observed at the flaking. Flaking morphology of failed bearings in wind turbine gearbox and automotive electrical accessories seem to be very similar as shown in Fig.1 and Fig.2 (b) although bearing types and size are quite different. Namely, small size ball bearings are used for automotive electrical accessory and large size roller bearings are used for wind turbine gearboxes. Figure 2 (c) shows the cross section of an area without flaking in the same bearing as shown in Fig. 2 (a) and (b). White structure was observed even in this area, which is most likely to be the prior stage to flaking. Therefore it is presumed that this type of flaking in wind turbine gearboxes is initiated at the white structure.

Figure 3 shows the observation results of the other failed bearing, which is also a cylindrical roller bearing and used on the high speed shaft in wind turbine gearboxes. There were several large cracks longer than 10mm and many small cracks around 1–3 mm in the axial direction on the raceway surface of the inner ring. Figure 3 (a) shows two small cracks chosen of many axial cracks, which were observed on the raceway surface. The small cracks seem to be an early stage of crack propagation. A small axial crack was chosen for the cross section observation because small cracks are easier than large cracks to find the location of the crack initiation. Figure 3 (b) shows the cross section including the small axial crack area. White structure was seen and it is seemed that a crack propagated along the white structure and reached the raceway surface. This crack is seen as the axial crack on the raceway surface.

Crack reached raceway surface

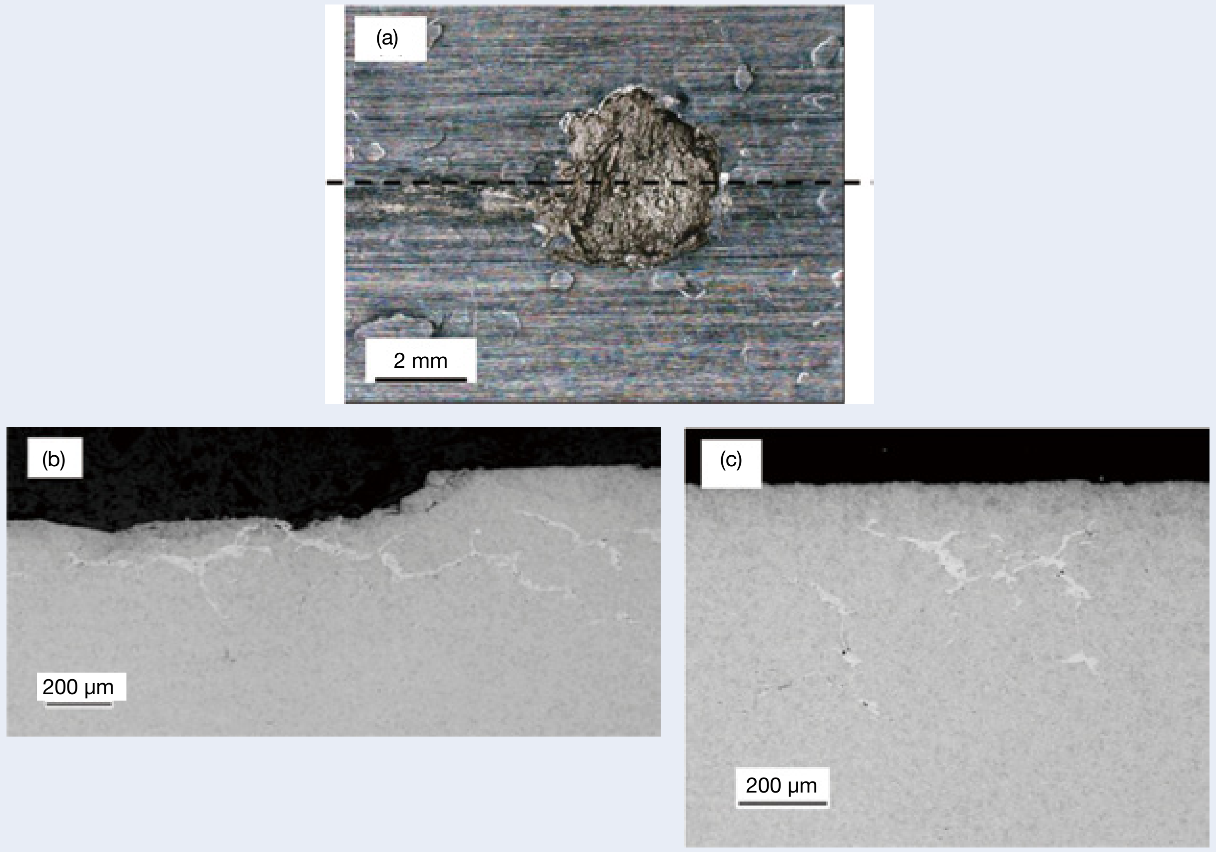

Fig. 2 The raceway and the cross section of a failed bearing with white structure.
(a) Raceway surface of flaking area
(b) Cross section of the dotted line in Fig.2 (a)
(c) Cross section of no flaking area

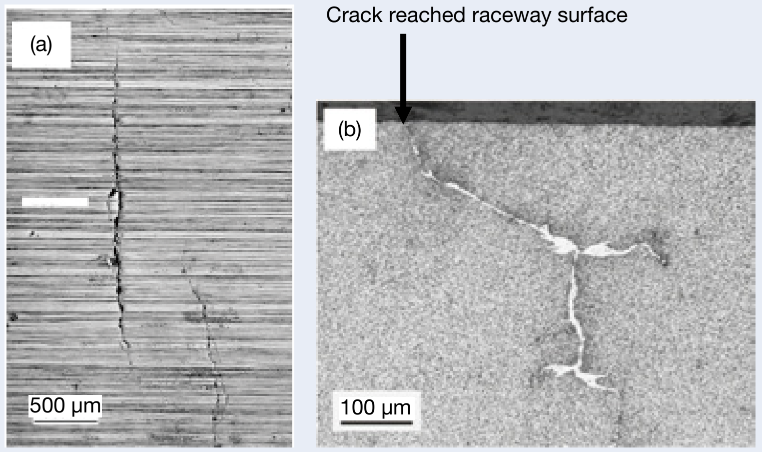

Fig. 3 The raceway surface and the cross section of a failed bearing with axial cracks.
(a) Axial cracks on the raceway surface
(b) The cross section through the cracks

3. Rolling contact fatigue tests to reproduce white structure flaking and axial cracking

Reproduction of the bearing failure mode is important to know the failure mechanism and to find the most appropriate countermeasure. We carried out two kinds of rolling contact fatigue tests in order to reproduce white structure flaking and the axial cracks. Hydrogen is utilized in these tests because microstructural changes called white structure were seen in both of these failure modes.

3.1 Experiment to reproduce white structure flaking

Flat disk type specimens with a diameter of 65 mm and a thickness of 6 mm were used in rolling contact fatigue test. The specimens were made of JIS-SUJ2 bearing steel, equivalent to SAE52100 and DIN-100Cr6. The specimens were quenched and tempered to produce a final hardness of 740 HV and the surface was ground and then lapped.

Before rolling contact fatigue testing, the specimens were charged with hydrogen by immersing them in NH4SCN aqueous solution at 323 K for 24 h.

The specimens were immediately assembled into the thrust bearing test machine after having been charged with hydrogen as shown in Fig. 4. The upper race was a 51305 thrust bearing ring and the lower race was the specimen mentioned above. The rolling elements were 6 balls with a diameter of 9.525 mm. The retainer used was made of brass. The lubricating oil used was ISO-VG68. The maximum contact pressure was 3.8 GPa and the rotating speed was 1 000 min^{-1}.

3.2 Test result of rolling contact fatigue to reproduce white structure flaking

Figure 5 shows the result of thrust type rolling contact fatigue tests using the hydrogen-charged specimen and uncharged specimen. Flaking occurred in the hydrogen-charged specimens, and the rolling contact fatigue life was much shorter than in the uncharged specimen.

Figure 6 (a) shows the microstructure of the flaking cross section in the hydrogen-charged specimen. White structure was observed around the flaking area. White structure was observed also in the cross section of an area without flaking as shown in Fig. 6 (b). Therefore, it is presumed that this flaking was initiated from white structure formed subsurface. On the other hand, flaking did not occur and the tests were suspended in the uncharged specimen. There was no microstructural change in the uncharged specimen. Therefore, it is presumed that hydrogen induced microstructural change and decreased rolling contact fatigue life. It seems that these microstructural changes observed in the rolling contact fatigue tests using hydrogen-charged specimens are the same microstructure as seen in failed bearings of wind turbine gearboxes and automotive electrical accessories.

It is reported that hydrogen enhances localized plasticity and this mechanism is known as the HELP theory[13)]. Therefore, it is supposed that white structure represents a localized microstructural change by interaction between cyclic plasticity and hydrogen in the rolling contact fatigue process[11)].

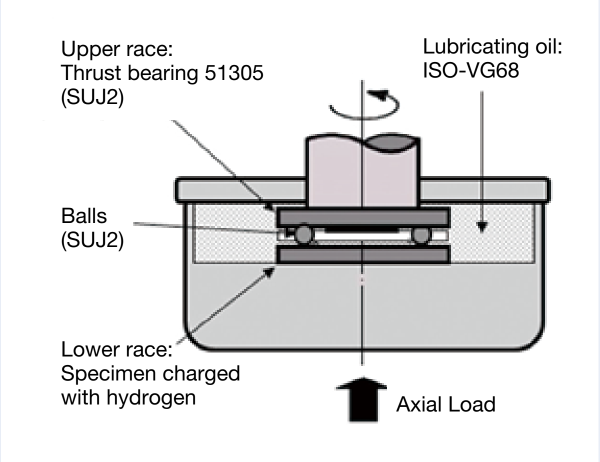

Fig. 4 Schematic of the thrust type rolling contact fatigue test machine.

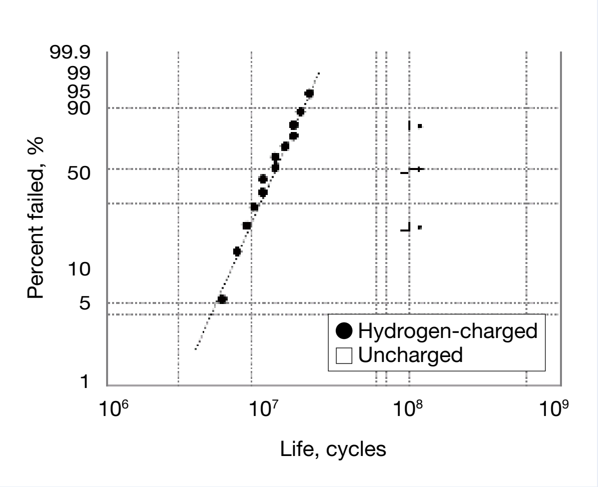

Fig. 5 The results of thrust type rolling contact fatigue tests

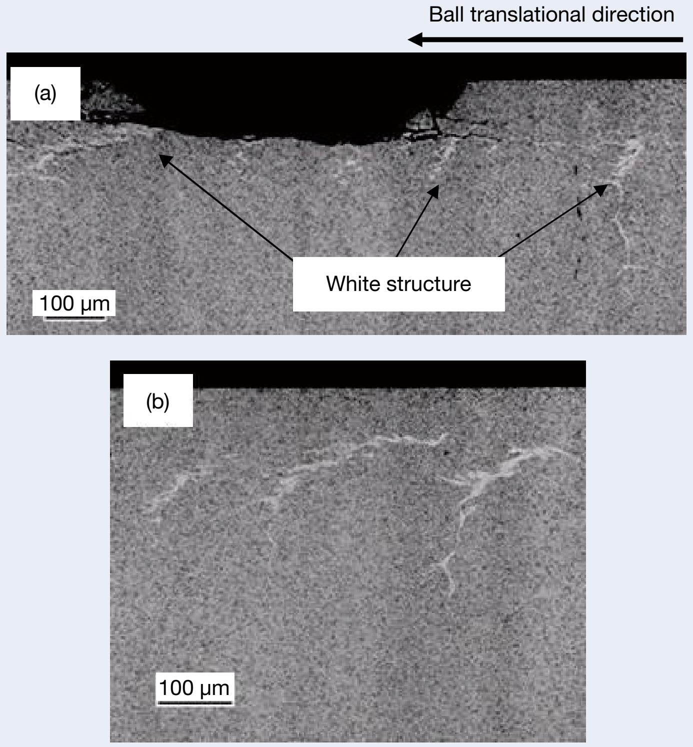

Fig. 6 The cross section of hydrogen-charged specimen.
(a) Flaking area, (b) No flaking area

3.3 Experiment to reproduce the axial cracks

Cylindrical roller bearings are used for the experiment to reproduce the axial cracks, because they are often used for wind turbine gearboxes and the axial cracks have not been seen in ball bearings. Although, white structure flaking has been observed in ball bearings. Bearing number of N308 made of JIS-SUJ2 bearing steel, equivalent to SAE52100, were used as the test bearings with a bore diameter of 40 mm and an outside diameter of 90 mm. Only the outer ring was separated and charged with hydrogen by the same method mentioned previously and the inner ring and the rollers were uncharged, and then the test bearing was set on the radial type bearing test machine as shown in Fig. 7. The reason why the outer ring was chosen for hydrogen charge is that hydrogen in the outer ring is more difficult to diffuse out of the steel than the inner ring as the temperature of outer rings are normally lower than of inner rings. The lubricating oil used was ISO-VG150. The maximum contact pressure on the outer raceway was 2.1 GPa and the rotating speed was 3 000 min^{-1}.

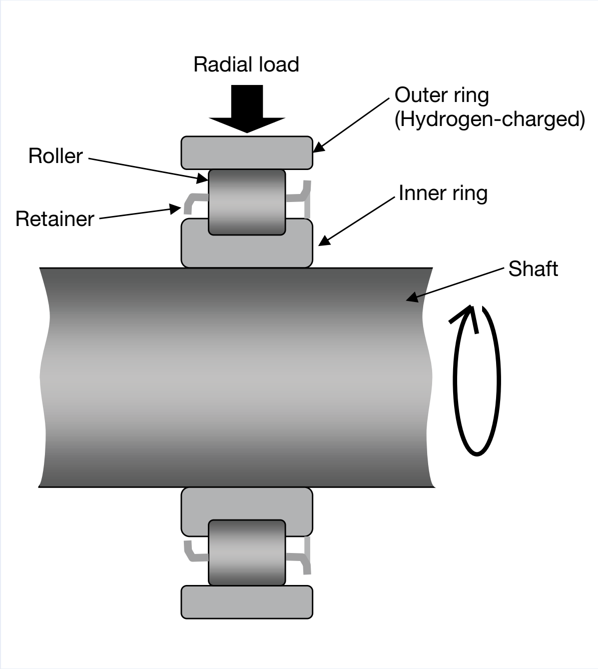

Fig. 7 A schematic of radial type bearing test machine.

3.4 Test result of bearing life test to reproduce axial cracks

Bearing life test of the hydrogen-charged bearing was stopped by detecting the vibration at the testing time of 280 h. On the other hand, the test of the uncharged bearing was suspended at the testing time of more than 1 000 h because there was no sign of bearing failure.

Figure 8 shows the outer ring raceway surface which was charged with hydrogen. One large crack and two small cracks were observed. These cracks propagated straight in the axial direction and were identical to the axial cracks in the failed bearings of wind turbine gearboxes.

Figure 9 (a) shows the cross sections of the cracking area including the position 2 in Fig. 8 (a). The large crack propagated in the depth direction. White structure was observed independently in Fig. 9 (a) position 1 to the left of the large crack magnified in Fig. 9 (b). And also, Figure 9 (c) is the magnification of the position 2 in Fig. 9 (a) and including the small axial crack in Fig. 8 (c). The small crack connected with white structure. Therefore it is supposed that white structure was formed first such as in Fig. 9 (b) and then a small crack initiated from the white structure and propagated to the raceway surface such as Fig. 9 (c) and finally the crack propagated in the axial and depth directions such as is visible in Fig. 8 (a) and Fig. 9 (a). Figure 9 (d) shows the cross section including the small axial crack in Fig. 8 (b). White structure was observed also in this area and it seems that the crack initiated at the white structure and propagated to the surface. However, white structure was not observed on the cross section of the large axial cracks. This reason is supposed that the initiation of the large axial crack would be white structure, but it is difficult to observe the cross section pinpointing the crack initiation. It is much easier to observe the cross section of the crack initiation in the small axial cracks.

Failure mode of the axial cracks is very unique and is seldom seen in other applications except for wind turbine gearboxes. However, it seems that the hydrogen-charge method does reproduce it. This method is very simple and the other effects on rolling contact fatigue are small. Therefore, it is supposed that axial cracks seen in wind turbine gearbox bearings are also caused by hydrogen. The patterns of white structure due to hydrogen are random, so that cracks along the white structure can propagate in various directions. It is supposed that some cracks mainly propagate in a horizontal direction to the rolling element's translational direction and finally cause flaking, and that other cracks mainly grow in the vertical direction to the rolling element's translational direction and results in the axial cracks on the raceway surface as shown in Fig. 10.

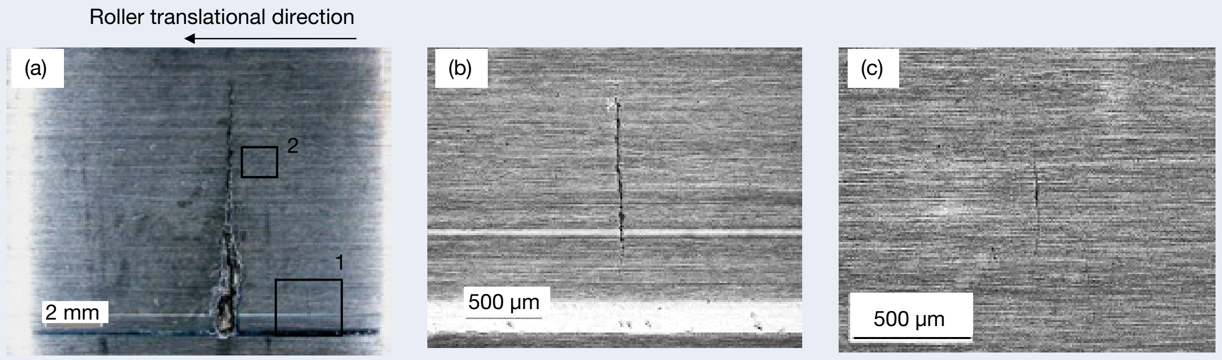

Fig. 8 The raceway surface of the hydrogen-charged outer ring.
(a) Large axial crack
(b) Magnification of position 1 in Fig. 8 (a)
(c) Magnification of position 2 in Fig. 8 (a)

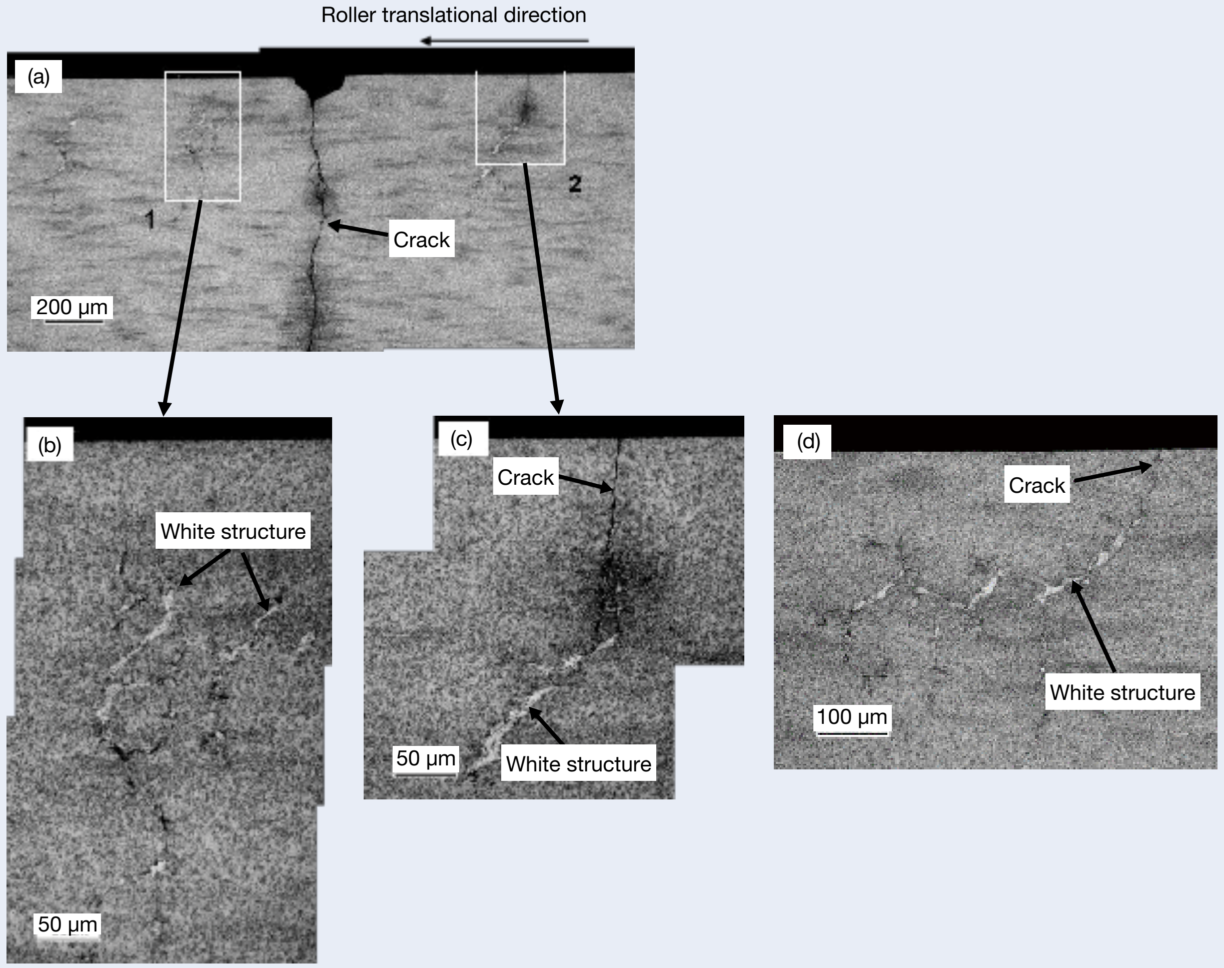

Fig. 9 The cross section of the cracked area of a hydrogen-charged outer ring
(a) The cross section of position 2 in Fig. 8 (a)
(b) Magnification of position 1 in Fig. 9 (a)
(c) Magnification of position 2 in Fig. 9 (a)
(d) The cross section of the small crack in Fig. 8 (b)

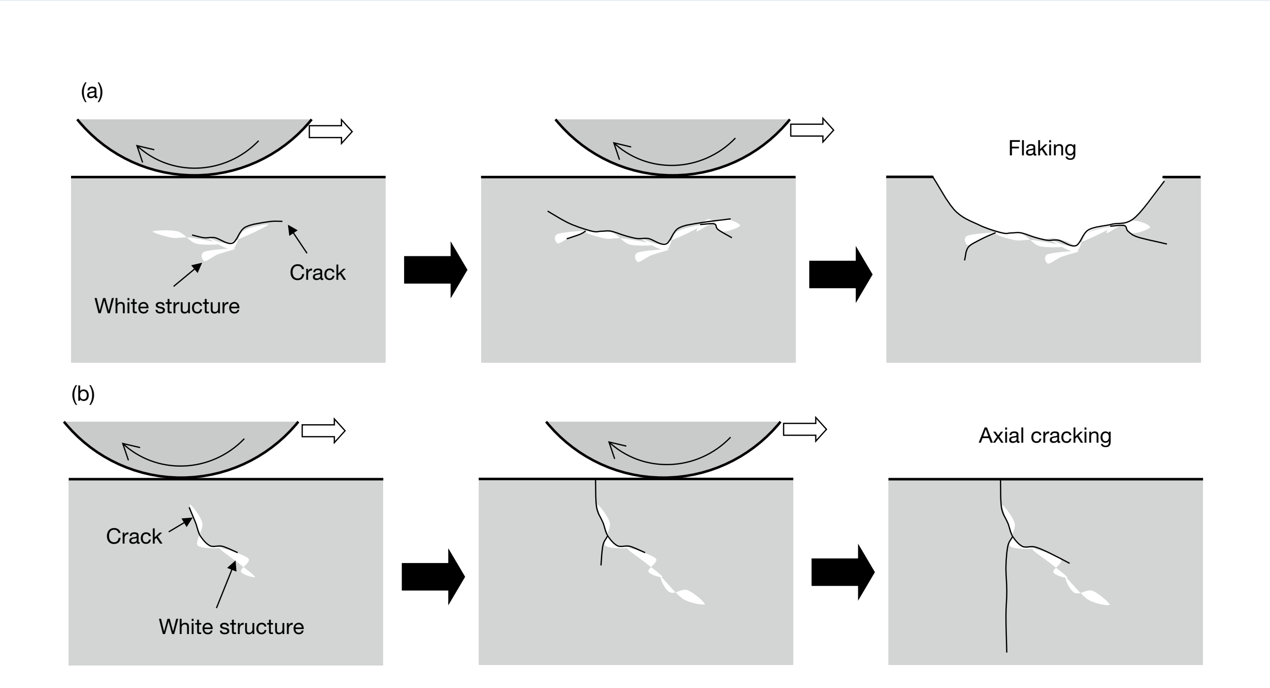

Fig. 10 Schematics of the failure process of white structure flaking and axial cracking
(a) The case of flaking, (b) The case of axial cracking

4. Operating condition inducing white structure flaking

The bearing failures in wind turbine gearboxes are more likely to be caused by hydrogen as shown in the rolling contact fatigue tests to reproduce white structure flaking and axial cracking. Therefore, it is important to know the causes of hydrogen generation and penetration into the bearing steel, although there is no direct evidence that hydrogen is generated and penetrated into the steel in wind turbine gearbox bearings. It is reported that hydrogen is generated by decomposition of lubricant and it is enhanced by the type of lubricant, water in the lubricant, slip, vibration, and electric current[3–9, 14]. These previous studies are mainly conducted for automotive bearings. However, influencing factors are basically common also to wind turbine gearbox bearings.

4.1 Type of lubricant

It is reported that lubricant is decomposed by a chemical reaction with a fresh metal surface, which is formed by local metal-to-metal contact and thereby generates hydrogen[4–9, 14]. Bearing life of white structure flaking is depending on additives included in the lubricant[4, 5, 8, 9, 14]. Some additives decrease bearing life and other additives increase it. The effect of extended life is more likely due to the oxidation film formed by a tribochemical reaction. Oxidation film can prevent a fresh metal surface from being exposed to lubricants and keeping the raceway surface chemically stable as some kinds of additives enhance to form the oxidation film on the fresh metal surface.

4.2 Slip and vibration

Slip between rings and rolling elements and bearing vibration can cause local metal-to-metal contact resulting in the exposure of a fresh metal surface. In the study about automotive ball bearings, it is reported that white structure was not formed at the bottom center of the raceway where maximum contact pressure was subjected, but instead near the raceway shoulders where large differential slip occurred[6, 7, 9].

Slip between rings and rollers are relatively small in cylindrical roller bearings and tapered roller bearings, which are normally used for wind turbine gearboxes. However large slip may occur during rapid acceleration and deceleration of a rotating shaft.

4.3 Electric current

The problem of white structure was well known first in bearings for automotive electrical accessories. Static electricity was believed as the cause of hydrogen generation because frictional electrification can occur between the pulley and the drive belt made of rubber. It is reported that ceramic ball and an insulated pulley to shut out electric current prevented white structure flaking and that the grease containing nano-carbon powders with conductivity was also very effective because it can keep static electricity neutralizing and prevent the electric discharge at metal-to-metal contact[8]. Electric discharge forms a fresh metal surface where the steel surface is locally melted by a spark.

Electrical corrosion in rolling bearings only occasionally occurs in generators of wind turbines[1]. Stray currents from the generator may affect gearbox bearings.

5. Effects of material on white structure flaking

Hydrogen is most likely to be a concern with bearing failures in wind turbine gearboxes as mentioned previously. Prevention of hydrogen generation and penetration into the bearing steel is very effective countermeasures for white structure flaking; however it is currently unclear which operating conditions induce wind turbine gearbox white structure failures. Material improvement with a strong resistance to hydrogen is also a candidate as another countermeasure.

5.1 Effect of chemical composition of steel

Figure 11 shows the result of a rolling contact fatigue test using the flat disk specimens charged with hydrogen and the thrust type rolling contact fatigue test machine in the same way as shown in Fig. 4. Four kinds of steels were used for the specimens; JIS-SUJ2 equivalent to SAE52100, steel A, B and C. Chemical compositions were different in them; steel A contains more Mn, steel B contains more Si and steel C contains more Cr. Rolling contact fatigue life of steel A, B and C were extended comparing to JIS-SUJ2. This result suggests that white structure flaking life can be extended by improvement of chemical composition of steel and it can delay formation of the white structure.

5.2 Effect of heat treatment

Figure 12 shows the result of a rolling contact fatigue test using hydrogen-charged specimens in the same way. Two kind of specimens with the same chemical composition of steel (JIS-SUJ2) and a different heat treatment were used, namely one data set used was through hardened specimens and the other was carbonitriding specimens. The rolling contact fatigue life of the carbonitriding specimens was longer than the through hardened specimens. It is supposed that compressive residual stress and larger amounts of retained austenite near the surface, which were formed by the carbonitriding heat treatment were effective against white structure flaking. Compressive residual stress can delay crack propagation initiated at the white structure, resulting in an extended time from crack initiation to flaking. Retained austenite can delay hydrogen from concentrating in high subsurface shear stress areas because the hydrogen diffusion rate in an austenitic structure is much slower than in a martensitic structure[15].

These results suggest that an optimum combination of chemical composition of the steel and heat treatment condition can produce long life bearings resistant to the formation of white structure flaking.

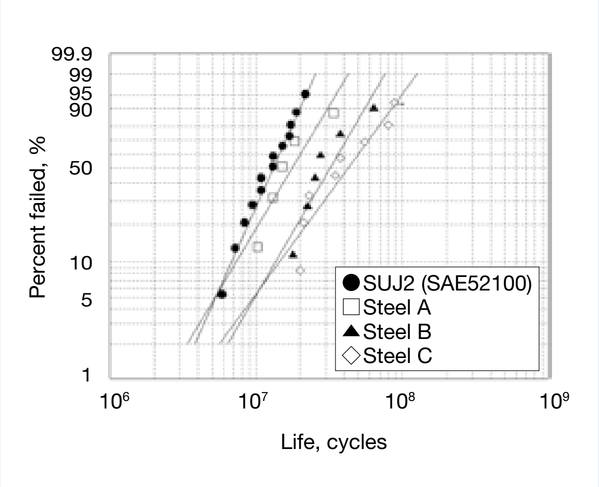

Fig. 11 The effect of the chemical composition of steel on white structure flaking life.

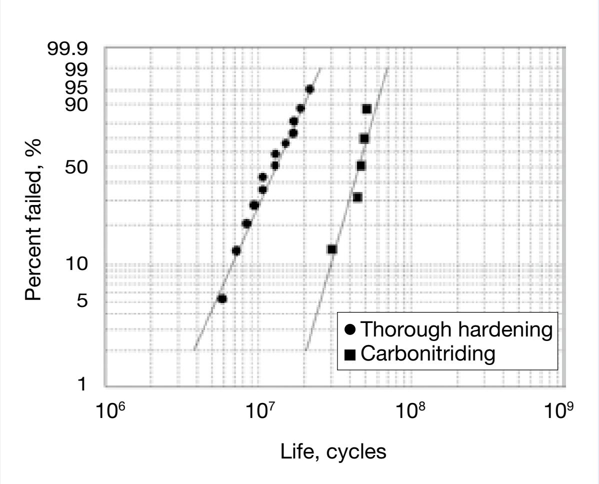

Fig. 12 The effect of heat treatment on the white structure flaking life.

6. Conclusions

The following conclusions were obtained from investigating failed bearings in wind turbine gearboxes, conducting rolling contact fatigue tests to reproduce the failure modes, and estimating material effects on the flaking life.

(1) Failure modes of wind turbine gearbox bearings were mainly classified as white structure flaking and axial cracking on the raceway. Both of them were involving a microstructural change called white structure.

(2) White structure flaking and the axial cracking were reproduced by using specimens charged with hydrogen in rolling contact fatigue tests. The axial cracks also seem to be initiated at the white structure. Therefore it is supposed that both failure modes in wind turbine gearbox bearings were caused by hydrogen.

(3) Additives in lubricants, slip, vibration and electric current can induce hydrogen generation by decomposing lubricant and penetrating into the bearing steel, although there is no direct evidence of this in wind turbine gearbox bearings.

(4) Improvement of the chemical composition of steel can extend the white structure flaking life and it is supposed that the suitable addition of the alloying elements delays the progression of microstructural change. Carbonitriding heat treatment was also effective against the formation of white structure flaking, because it is presumed that compressive residual stress near the surface can delay crack propagation and larger amounts of retained austenite can delay hydrogen concentration in areas of high shear stress.

7. References

(1) M. H. Evans, "White structure flaking (WFS) in wind turbine gearbox bearings: effects of butterflies and white etching cracks (WECs)," Material Science and Technology, 28–1 (2012) 3–22.

(2) K. Furumura, Y. Murakami and T. Abe, "The Development of Bearing Steels for Long Life Rolling Bearings under Clean Lubrication and Contaminated Lubrication," Proceedings of 4th International Symposium on Bearing Steels, San Diego, Creative Use of Bearing Steels, ASTM STP 1195 (1993) 199–210.

(3) Y. Murakami etc., "Long Life Bearings for Automotive Alternator Applications," SAE Technical Paper Series, 950944 (1995) 1–14.

(4) M. Kohara, T. Kawamura and M. Egami, "Study on Mechanism of Hydrogen Generation from Lubricants," Tribology Transactions, 49 (2006) 53–60.

(5) KK. Tamada and H. Tanaka, "Occurrence of Brittle Flaking on Bearings Used for Automotive Electrical Instruments and Auxiliary Devices," Wear, 199 (1996) 245–252.

(6) N. Kino and K. Otani, "The Influence of Hydrogen on Rolling Contact Fatigue Life and Its Improvement," JSAE Review, 24 (2003) 289–294.

(7) S. Fujita, N. Mitamura and Y. Murakami, "Research of New Factors Affecting Rolling Contact Fatigue Life," Proceedings of WTC 2005, Washington-63400 (2005).

(8) K. Iso, A. Yokouchi and H. Takemura, "Research Work for Clarifying the Mechanism of White Structure Flaking and Extending the Life of Bearings," SAE Technical Paper Series, 2005-01-1868 (2005) 1–11.

(9) S. Tanaka, "Pulley Support Bearings for Push-Belt CVTs," NSK Technical Journal Motion & Control, 19 (2006) 13–19.

(10) S. Fujita, H. Tanaka, "Long-Life Materials Countering White Structure Flaking," NSK Technical Journal Motion & Control, 19 (2006) 20–26.

(11) H. Uyama, H. Yamada, H. Hidaka and N. Mitamura, "The Effects of Hydrogen on Microstructural Change and Surface Originated Flaking in Rolling Contact Fatigue," Tribology Online, 6–2 (2011) 123–132.

(12) J. Gegner, "The Bearing Axial Cracks Root Cause Hypothesis of Frictional Surface Crack Initiation and Corrosion Fatigue Driven Crack Growth," NREL Work Shop, Wind Turbine Tribology Seminar-Broomfield-November-2011.

(13) H. K. Birnbaum and P. Sofronis, "Hydrogen Enhanced Localized Plasticity – a Mechanism for Hydrogen Related Fracture," Materials Science and Engineering, A176 (1994) 191–202.

(14) R. Lu, H. Nanao, K. Kobayashi, T. Kubo and S. Mori, "Effect of Lubricant Additives on Tribochemical Decomposition of Hydrocarbon Oil on Nascent Steel Surfaces," Journal of the Japan Petroleum Institute, 53–1 (2010) 55–60.

(15) D. J. Fisher, "Hydrogen Diffusion in Metals," Scitec Publication, Switzerland (1999).

Hiroki Yamada

Hideyuki Uyama

Development of New-Type Oxide Ceramic Ball for Bearings

Yuichi Endo, Yasuyuki Shimizu, and Koji Ueda
NSK Ltd.

Abstract

The rolling contact fatigue life of oxide ceramics such as alumina and zirconia is known to be inferior to silicon nitride, which is used as a standard bearing ceramic material. Therefore, we have developed a new type of oxide ceramic material by creating a composite of alumina and zirconia with rolling contact fatigue properties and toughness equal to silicon nitride.

Translated and reprinted from the ITC, TOKYO2015, Extended Abstract, with the approval of the Japan Society of Tribologists.

1. Introduction

The rolling contact fatigue life and static capacity of silicon nitride are similar to standard bearing steel. Therefore, it is used as the standard ceramic material for bearings. In addition to silicon nitride, oxide ceramics are also used as a bearing material. However, the rolling contact fatigue life of the oxide ceramics is inferior to silicon nitride and therefore there use is limited to a relatively small number of applications. We therefore developed a new type of oxide ceramic material by producing a composite of alumina and zirconia, which is able to achieve productivity and functionality as a bearing material. We will report in this paper about the rolling contact fatigue properties and fracture toughness of the new type of oxide ceramic material.

2. Test method

Life testing was conducted on 51305 thrust ball bearings with a 25mm bore diameter and a 52mm outside diameter. Each bearing was composed of a combination of ceramic rolling elements and steel ring raceways. Alumina, zirconia, composite oxide (alumina-zirconia), and silicon nitride were used for the ceramic rolling elements. The ring raceways were made in through-hardened and tempered SAE52100 steel. The test conditions were as follows; 4.4kN axial load, 1 000 min^{-1} rotating speed, 3/8 inch (9.525mm) ball size, 3 balls per test, ISO-VG68 lubrication oil and plastic cages. After life testing, the ceramic balls were examined for damage using a scanning electron microscope (SEM).

Fracture toughness was measured by the IF method based on ASTM F 2094-06 using a Vicker's indenter with a load of 196N and a dwell time of 30s. The measurements were made on a polished cross-section of a ceramic ball; 3 measurements per ceramic ball type. To observe crack propagation, a crack was produced in the surface of sample balls using a Vicker's indenter with a load of 196N and dwell time of 30s. This was done after highlighting the grain boundaries of the sample balls made in alumina, zirconia and composite oxide by thermally etching at a temperature of 1573K and keep time of 30 min. After this procedure, the crack propagation was observed by SEM.

3. Result and Discussion

Fig.1 shows the results of the life test for the ceramic ball bearing sets in the form of a Weibull plot.

The bearings with alumina and zirconia balls were damaged at less than 1/100 of the L_{10} life of the bearing with silicon nitride balls, whereas the bearing with composite oxide balls achieved an L_{10} life 1×10^8 cycles, which was as long as the bearing with silicon nitride balls.

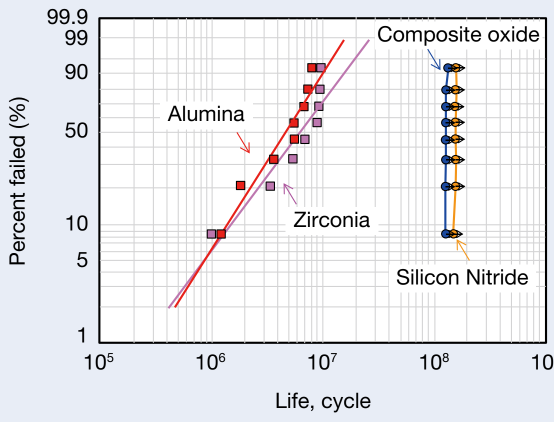

Fig. 1 Result of life test

Fig.2 shows the appearance of damaged ceramic balls after life testing. The grain dropout was observed on the surface of alumina balls as shown in Fig. 2(a). The concentric flaking was observed on zirconia balls.

As for the composite alumina-zirconia balls and silicon nitride balls, life testing with a higher load was conducted until they became damaged. As a result, concentric flaking were observed as with zirconia balls on both these ball types as shown in Fig. 2 (c) and (d).

The damage condition of the higher toughness material tended to be concentric flaking as shown in Fig. 2 and Table 1. Toughness is considered to be one of the factors affecting the damage condition. There is a report which states that the toughness depends on grain size and alumina with a smaller grain size has higher toughness[1]. We therefore compared the grain size and the condition of crack propagation of each type of ceramic ball. The grain size of the zirconia and composite oxide is smaller than that of alumina Fig. 3 (a), (b) and (c).

All crack propagation occurred along the grain boundaries as shown in Fig. 3 (a), (b), (c) and (d). As the grain size reduces so the number of grain boundaries along which the crack has to propagate increases.
This makes it more difficult for the crack to propagate due to the increase in energy needed to divide the grain boundaries. As a result, it is estimated that the toughness value becomes high[2].

There was a clear difference in the contact fatigue life of composite oxide and zirconia, even if the toughness and damage condition were similar. The reason for the difference is the quantity of internal defects and the effects of residual compressive stress achieved by combining alumina and zirconia, which have different thermal expansion coefficients[3].

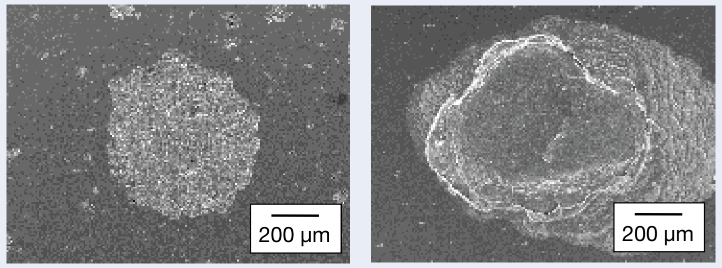

(a) Alumina (b) Zirconia

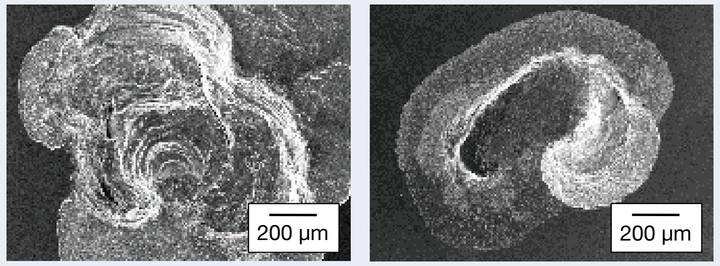

(c) Composite Oxide (d) Silicon Nitride

Fig. 2 Appearance of damaged ceramic ball

Table 1 Fracture toughness of ceramic ball

Ceramic ball	Fracture Toughness, $\mathrm{MPa{\cdot}m^{1/2}}$
Alumina	4.0 - 4.3
Zirconia	6.3 - 6.6
Composite Oxide	6.4 - 6.9
Silicon Nitride	6.5 - 7.2

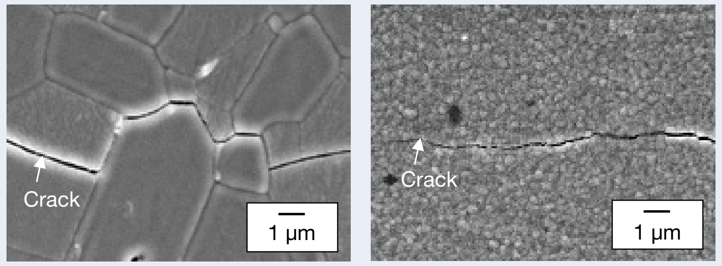

(a) Alumina (b) Zirconia

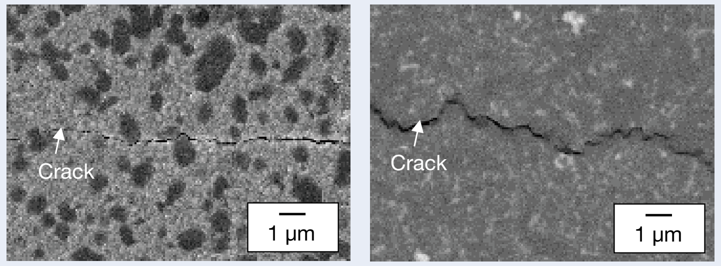

(c) Composite oxide (d) Silicon Nitride

Fig. 3 Microstructure of ceramic ball

4. Conclusions

The rolling contact fatigue properties of a new type of oxide ceramic were investigated in this study. The conclusions were as follows:

1. The life of the composite oxide was improved compared to conventional alumina and zirconia and similar to silicon nitride.
2. The damage condition depends on toughness with grain dropout observed on the surface of alumina balls and concentric flaking observed on the surface of the tougher ceramic materials such as zirconia, composite oxide and silicon nitride.
3. The toughness depends on grain size. If the grain size is small, the number of grain boundaries along which the crack has to propagate is large, which makes it difficult for the crack to propagate. As a result, it is estimated that toughness value is high.

5. References

1) K. Hayashi, K. Gotoh, T. Nishikawa, “Grain size dependence of fracture toughness in polycrystalline alumina,” Journal of the Ceramic Society of japan, 99–7 (1991) 620–624.
2) T. Nishida, I. Kameyama, “Evaluation of fracture toughness for structural ceramics using SEPB specimens (Part 4),” Journal of the Ceramic Society of japan, 100–3 (1992) 276–281.
3) K. Tanaka, M. Matsui, R. Shikata, T. Nishikawa, “X-ray measurement of triaxial residual phase stress in zirconia-alumina composite ceramics,” Journal of The Society of Materials Science,Japan, 41–464 (1992) 593–599.

Yuichi Endo

Yasuyuki Shimizu

Koji Ueda

Correlations Between the Porosity and Friction Performance of Wet Friction Materials

Takayuki Hiramoto (Current Enrollment: Core Technology R&D Center)
NSK-Warner K.K. Core Material Development Department
Kenichi Iso
Core Technology R&D Center

Abstract

Wet friction materials are used in the clutches of automatic transmissions because of their high porosity and high elasticity. The porosity is significant, as it directly affects friction performance and durability. With X-ray CT, it is now possible to measure the three-dimensional distribution of the pores of friction materials in a way that has not been done before. Furthermore, the magnitude of porosity and pore diameter as well as three-dimensional distribution have been confirmed as important factors in terms of friction performance.

1. Introduction

In recent years in the automotive world, priority has been increasingly given to improving fuel efficiency and reducing emissions to address global environmental and resource-related concerns. Engineering development has been promoted to achieve weight saving, high efficiency, and improved drivability in automatic transmissions (ATs) that transmit engine drive force. Wet friction materials are used in clutches and brakes in ATs to efficiently transmit engine drive force (Figure 1). The number of requirements for heat resistance and durability in wet friction materials has risen year after year, as heat generation from clutches tends to increase due to its increased engaging frequency and high revolution engagement. There is also growing demand to multiply the number of shift steps toward improving AT efficiency and drivability[1–3].

Wet friction materials are made of paper containing fiber, filler, and friction modifier and are hardened with a thermo-setting resin such as phenol. They have high elasticity due to high porosity (Figure 2). Automatic transmission fluid (ATF) is absorbed and discharged through the pores when a clutch engages or disengages. The oil film underlying the friction interface is therefore significantly affected by the porosity, and friction performance varies depending on the pores[4]. Furthermore, ATF absorption and discharge through the pores lowers the temperature of the friction interface and prevents heat accumulation, and so the porosity of the friction material affects its longevity.

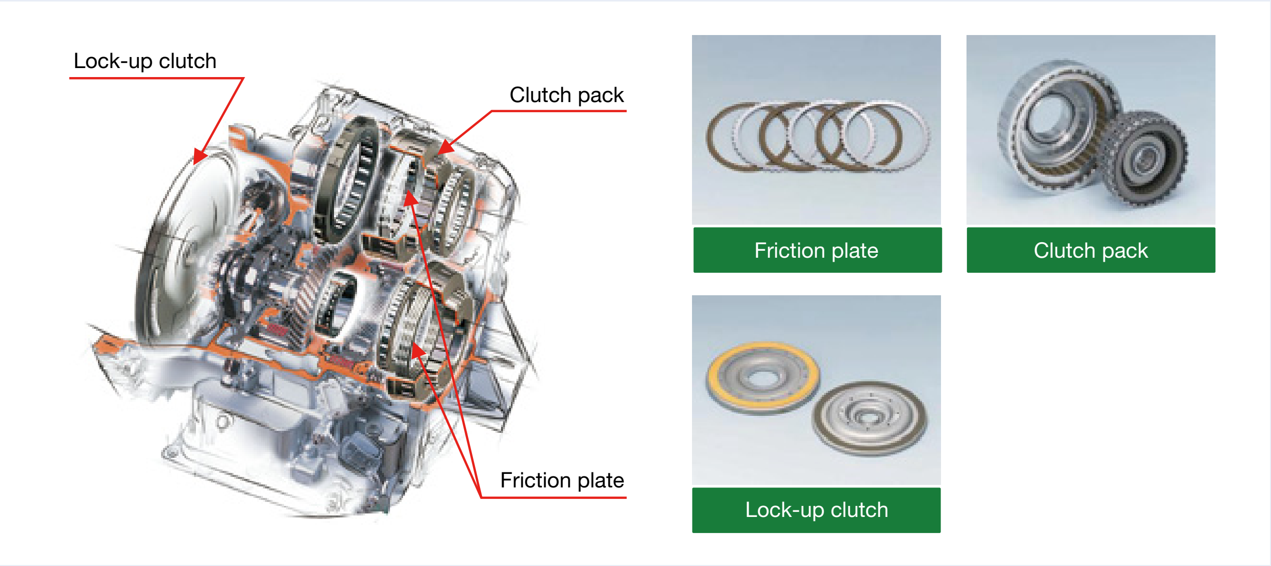

Fig. 1 Automatic transmission and friction materials

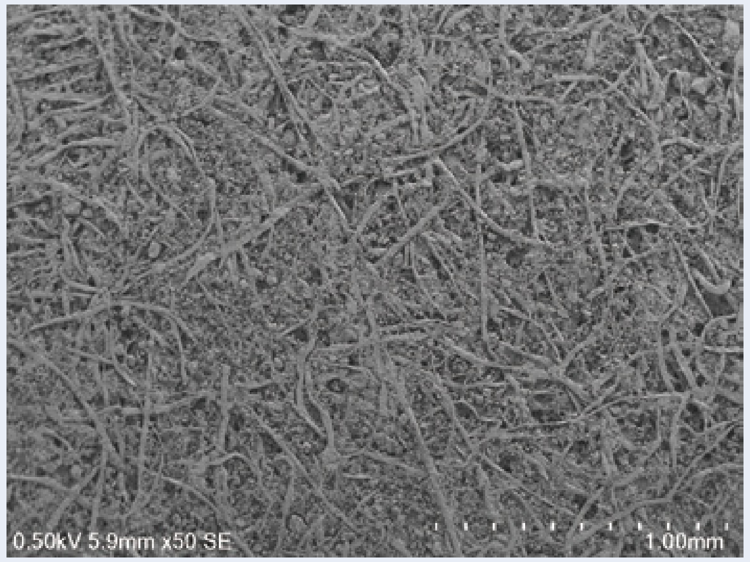

Fig. 2 Wet friction material

Measuring the porosity of friction materials was previously carried out using a mercury porosimeter (mercury intrusion technique). This allows for measuring the porosity of an entire friction material and pore diameter alone; however, it cannot be used to measure three-dimensional pore distribution. This article describes the inner structure of friction materials observed using X-ray CT as well as three-dimensional pore distribution and reports on correlations between porosity and friction performance.

2. Method of Measuring Porosity

2.1 Mercury porosimeter

With a mercury porosimeter, pore diameter can be calculated using Washburn's formula consisting of the applied pressure into pores and the surface tension. Equation 1 represents Washburn's formula and Figure 3 shows the schematic diagram of measurement.

$$D = \frac{-4\sigma\cos\theta}{P} \qquad (1)$$

D: Pore diameter, P: Pressure, θ: Contact angle, σ: Surface tension

There are some disadvantages to using a mercury porosimeter. For example, a sample may become deformed when pressure is applied. Also, the diameter of aperture through which the mercury passes is considered to be the pore diameter. This means that measuring the diameter of the inside pore is not possible, even if the area under the aperture is wider or narrower than the diameter.

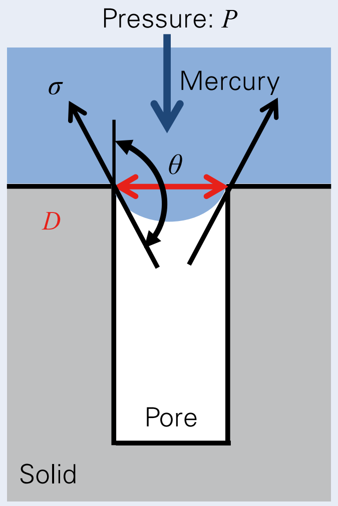

Fig. 3 Mercury intrusion technique

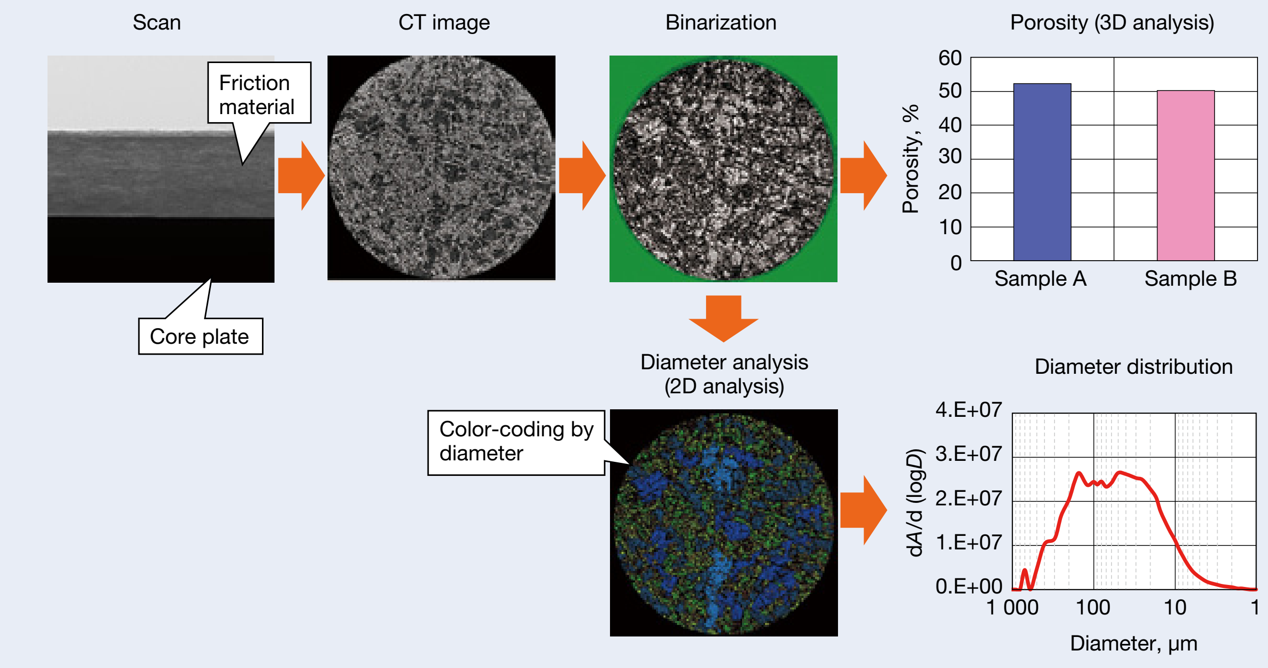

Fig. 4 Porosity analysis flow

2.2 X-ray CT

Figure 4 shows the workflow used for the porosity analysis with X-ray CT. The CT images are in grayscale and have been processed according to radiolucency. The low radiolucent fibers and fillers are bright and the high radiolucent materials, including air, are dark. The CT images were binarized through image processing, and the pores and materials were separated as either black or white. The porosity and pore diameter were analyzed in accordance with the binarized images. The porosity was calculated using three-dimensional analysis, while the pore diameter was determined using two-dimensional analysis. Since pores are interconnected in friction materials, individual pore diameter cannot be determined through three-dimensional analysis. Therefore, the pore diameters were analyzed using the cross-dimensional CT images of the friction materials and then calculated used the data that was obtained.

With X-ray CT, the above-mentioned problems can be avoided, including sample deformation and limited capability when measuring the aperture diameters alone.

3. Experiment

3.1 Friction material

Two types of friction material, with different porosity due to paper making processes, were used. Sample A had an even porosity and pore diameter, whereas Sample B was intentionally designed to be paper so that the construction would have an uneven structure with different porosity and pore diameter at various depths. Both materials had the same composition, and so the observed difference would be solely in porosity. Table 1 shows the composition and porosity of each material.

3.2 Pore measurements

Using a mercury porosimeter and X-ray CT, porosity was evaluated. In the X-ray CT evaluation, five different layers were analyzed at varying depths of both friction materials in order to determine pore distribution.

3. 3 Durability test

To determine the durability of each friction material, a continuous slip tester was used to measure temporal changes in the friction coefficient. Conditions for the evaluation were 400 rpm, a torque of 77 N·m, a flow of 1.0 L/min, an engagement time of 25 seconds, a disengagement time of 30 seconds, and a total heat generation of 16 850 kJ/cm^2.

Table 1 Sample composition and porosity[5)]

	Sample A	Sample B
Aramid fiber [mass, %]	28.5	28.5
Diatom earth [mass, %]	28.5	28.5
Phenol resin [mass, %]	45	45
Porosity [vol., %]	52.2	50.2
Porosity distribution	uniform	non-uniform

4. Results and Discussion

4.1 Distribution of pores

Figure 5 shows the pore diameter distribution that was measured using the mercury porosimeter. Sample A has a peak in pore diameter, whereas Sample B has two peaks. In addition, the pore diameter is greater in Sample B than in Sample A.

Figure 6 shows the CT images of the first (surface) layer and fifth layer of each friction material. The CT images were binarized through image processing to make the pores more distinctive. As the result, the pores are represented in black. Figure 7 shows the distribution of pore diameters in the first and fifth layers, which was calculated based on the CT images. Sample A shows little difference in the pore diameters in the first and fifth layers. Sample B has very large pores in the first layer compared to those in the fifth layer. It is evident that the larger diameter peak measured by the mercury porosimeter represents the pores in the first layer.

Figure 8 shows the porosity in each layer. In Sample A, the difference in porosity among the five layers is approximately 4%, showing an even porosity distribution. On the other hand, in Sample B, the difference is greater among the five layers, showing an uneven porosity distribution. The first layer showing particularly large pores has significant porosity, amounting to 10% more than that of the fifth layer.

The mercury porosimeter only revealed the difference that the porosity in Sample B is greater than that in Sample A. However, X-ray CT revealed that Sample A has an even distribution in both pore diameter and porosity, and that larger pores gather on the upper surface in Sample B with an uneven porosity distribution. Therefore, X-ray CT made the detailed porosity of friction materials observable, which had previously been unobservable by mercury porosimeter.

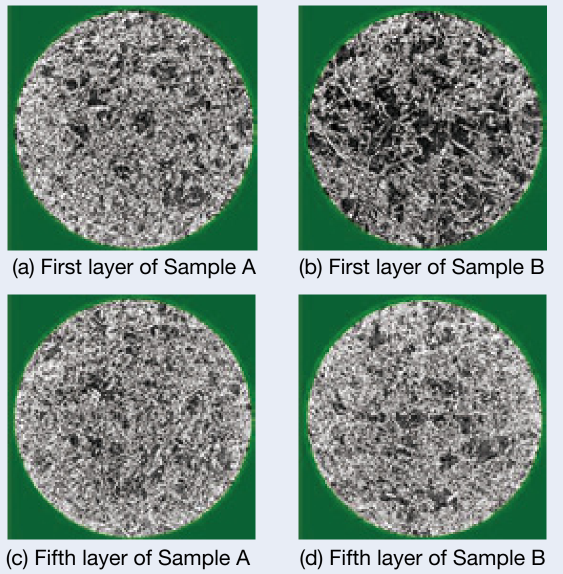
(a) First layer of Sample A
(b) First layer of Sample B
(c) Fifth layer of Sample A
(d) Fifth layer of Sample B

Fig. 6 Binary cross-sectional images of samples[5)]

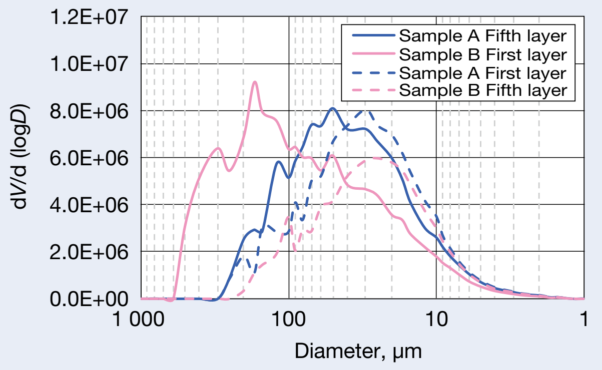

Fig. 7 Distribution of pore diameters in the first and fifth layers

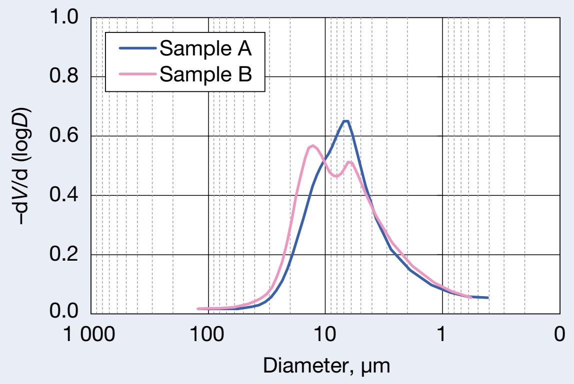

Fig. 5 Pore diameter distribution measured by a mercury porosimeter[5)]

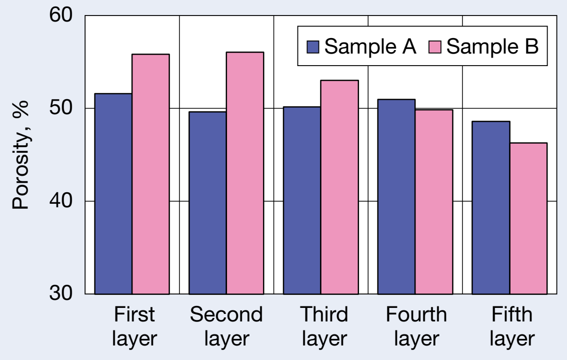

Fig. 8 Porosity distribution

4.2 Durability evaluation results

Figure 9 shows the temporal change in friction coefficient in a slip test. In Sample A, which has an even distribution of pore diameter and porosity, the friction coefficient is stable in the early phase of the test and gradually decreases from the middle to the late phase. In Sample B, however, where the pore diameter and porosity are both uneven, the friction coefficient continues to decrease from the early phase, which leads to a 10% or greater difference from Sample A.

It has been considered that the greater the pore diameter, the longer the life becomes due to less impact of clogging by sludge caused by ATF. However, this experiment has produced the opposite result in that the friction coefficient decreased earlier in Sample B, which has a larger pore diameter. The difference in surface density is a suggested cause of producing the gap in durability. Sample B has pores concentrated in the surface layer, and so the surface density becomes far lower compared to in Sample A. Therefore, it was confirmed that the friction coefficient decreased sooner because the surface pores were crushed by pressure at the early stages of the test.

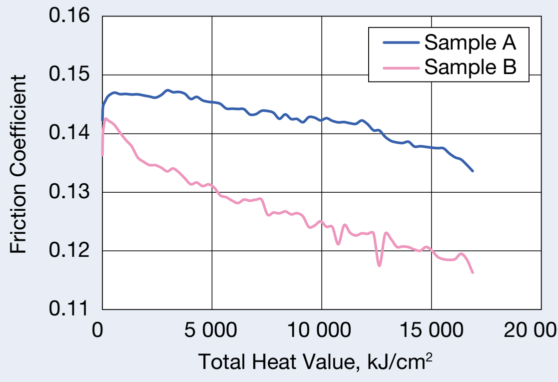

Fig. 9 Change in friction coefficient[5]

5. Afterword

With X-ray CT, measuring the three-dimensional distribution of the pores of the friction material is now possible. Furthermore, the magnitude of porosity and pore diameter as well as the three-dimensional distribution were all confirmed to be important factors in terms of determining the friction properties.

We will continue to develop high-performance friction materials as we further clarify the correlations between pore distribution and friction performance and by improving paper-making techniques to control pore distribution.

References

1) S. Kitahara and K. Maruo, “Recent technology of wet friction materials applied to automatic transmission,” JSDE journal “Design Engineering,” 49–10 (2014) 518–525.
2) S. Nagai, “Technology trends of friction materials for transmission,” THE TRIBOLOGY, shinjusha.info, No. 314 (2013) 21–23.
3) H. Suzuki, “Latest Technologies of Paper-Based Friction Material Applied to Automatic Transmission,” Journal of Chemical Engineering of Japan, 75–4 (2011) 53–55.
4) T. Miyoshi, “Friction characteristics and porosity of friction plate,” NSK Technical Journal, 655 (1993) 25–31.
5) T. Hiramoto, K. Iso, and K. Maruo, “Study of correlation between porosity distribution and friction performance,” International Tribology Conference TOKYO 2015 Extended Abstract.

Takayuki Hiramoto

Kenichi Iso

Development of a High-Power Two-Roller Traction Tester and Traction Curve Measurement

Hirofumi Itagaki, Masahiro Kita, and Hiroki Hashiguchi
Powertrain Technology Development Department

Abstract

Measuring and estimating the traction coefficient is necessary to improve transmission efficiency and to design compact, lightweight traction drive devices such as toroidal continuously variable transmissions. However, few attempts have been made to measure and estimate the traction coefficient under practical operating conditions, and the design of traction drive devices has used extrapolated values from the traction coefficient measured under low-power conditions. The question remains whether the estimated traction coefficient is applicable or not. Therefore, we developed a high-power two-roller traction tester to clarify the trends in variation of traction curves under various operating conditions similar to practical traction drive devices. This paper details the configuration of the tester and shows several resulting traction curve measurements. This traction tester contributes to building a traction curve database to make traction drive devices more compact, lightweight, and efficient.

1. Introduction

Thanks to their low-noise, low-vibration, continuously variable transmission, and other advantages, traction drive devices are used as acceleration/deceleration gear or transmission for automobiles, aircraft, and other industrial machines.

Figure 1 outlines the basic structure and power transmission principle of toroidal continuously variable transmission (T-CVT), a form of traction drive device. T-CVT is made up of multiple rolling elements (disks and power rollers) with a smooth surface. As shown in the enlarged illustration in Figure 1, a pair of disks and a power roller are in contact with each other with an axial force F_a applied in the disk axis direction. Thus, elasto-hydrodynamic lubrication film is formed in the contact area, and then a tangential force (traction force) F_t, generated as the shear resistance of the oil film, is transmitted between the disk and power roller. Traction force F_t is proportional to the contact surface normal component F_c (contact force) of which the proportional constant is called the traction coefficient. The coefficient μ is known to vary depending on creep caused between rolling elements, and the curve indicates the relationship between the two is called traction curve.

Figure 2 is a pattern diagram of the traction curve. The traction coefficient typically increases in a linear fashion in a relatively low creep rate range, and its gradient slows as the rate increases and starts to decline as soon as it reaches a maximum value (μ_{max}). In other words, traction drive devices are capable of transmitting drive force only in a low creep range below the maximum traction coefficient μ_{max}, and they experience gross slip (excessive slip) in a range over μ_{max}.

In designing traction drive devices, contact force and device dimension should be determined based on the required specifications of transmission torque. A parameter (μ_d), called design traction coefficient, is generally used to determine the contact force F_c needed for transmitting the torque T_r. A relational expression $F_c = T_r/(\mu_d \cdot R)$ holds, provided the rolling radius of the rolling element is R. If F_c is too great for a device to withstand, the dimensional data including R should be reconsidered.

To avoid gross slip, a design traction coefficient μ_d must be low enough with a certain margin against an estimated maximum traction coefficient μ_{max} under drive conditions (Figure 2). To ensure safety, however, if a design traction coefficient is set too low, a greater contact force F_c is required, as is clear from the above-mentioned relational expression $F_c = T_r/(\mu_d \cdot R)$. This is detrimental in that not only the dimension and weight of the device increase but the transmission efficiency and longevity decrease. Thus, to ensure the functionality of traction drive devices and improve their performance (more compact, lightweight, and efficient), it is imperative that an optimal design traction coefficient be determined by using the traction curves measured under practical operating conditions.

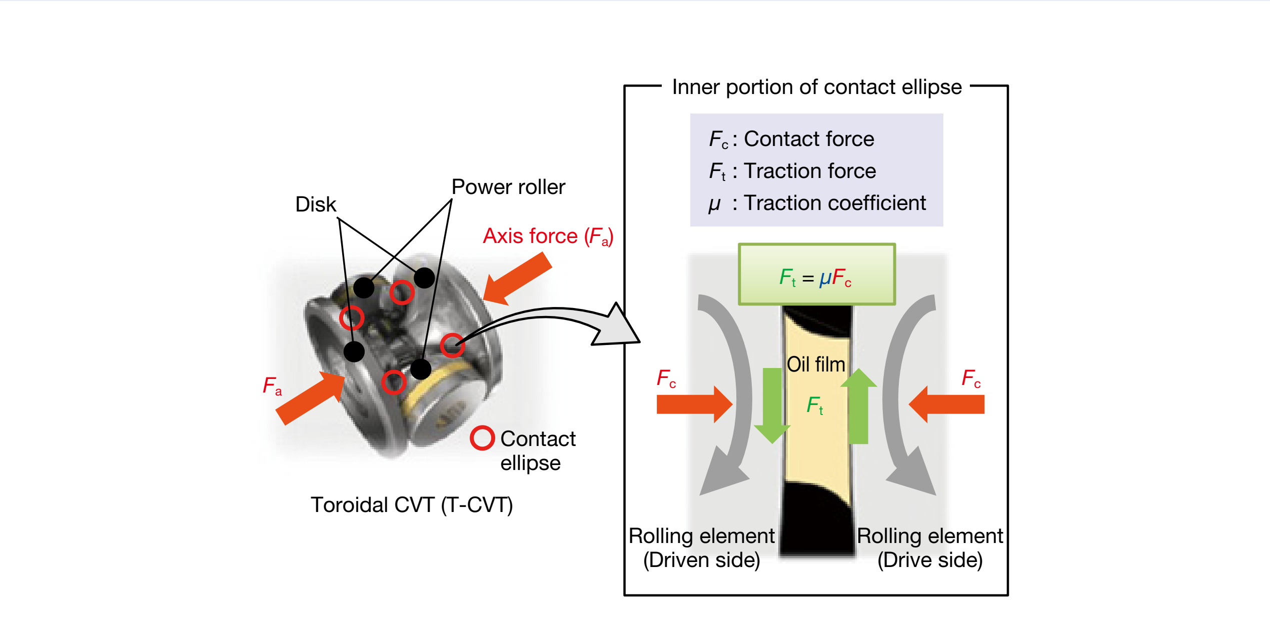

Fig. 1 Conceptual diagram of a T-CVT[19)]

Previous studies offered a large number of mathematical models[1–7)] to estimate the traction curve; however, as most of the models contain free parameters, the identification of which requires the actual measurement data of the traction curve. Many other studies address traction curve measurement, reporting that the traction curve geometry varies greatly depending on the operational conditions, including the type of traction oil, contact surface pressure, peripheral speed, and oil temperature, based on the measurement data obtained by using traction testers such as two-roller and four-roller traction testers[8–14)]. Also, in the case of continuously variable transmissions such as T-CVT, not just the operating parameters fluctuate by shift operation; they are also affected by spin caused in the rolling element. That is why studies have also been conducted on traction curve measurement at the spin-related contact area and on its theoretical analysis[15–18)].

In these studies, the traction curve measurement and the validity evaluation of the estimate method were performed using relatively low-power traction testers, which cannot sufficiently cover extensive operating conditions as actual traction drive devices face. In designing traction drive devices, although practical high-power operating conditions (e.g., 100 kW or more at each contact point) are needed to estimate the traction curve, the current state is that the estimation depends on the extrapolation of the traction curve measured under low-power conditions, which makes its applicability doubtful.

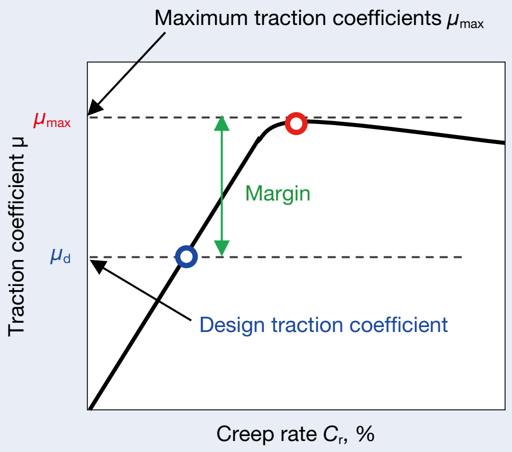

Fig. 2 Relationship between creep rate and traction coefficient (traction curve)

Therefore, we have developed high-power two-roller traction testers for the purpose of measuring and estimating the traction curves under unprecedented conditions, where actual operating conditions are presumed. This paper details the configuration of the developed tester and shows resulting traction curve measurement data.

2. High-power Two-roller Traction Tester

2.1 Configuration of tester

Figure 3 outlines the developed high-power two-roller traction tester. The tester consists of a chamber, electric motor, hydraulic cylinder, and oil circulation unit.

Inside the chamber, a flat-surface roller and spherical surface roller are in contact with each other, and the axis of each roller connects through the motor axis outside of the chamber via a gear box. The oil circulation unit consists of a tank, heater, pump, and other components that feed traction oil into the chamber (contact area of two rollers, gear, and bearing). The oil deposited at the bottom of the chamber is collected in the tank through an oil-drain port and supplied into the chamber again. During the test, traction oil was heated by the heater so that supply temperature and flow remained constant.

Figure 4 outlines the roller peripheral section. The rollers are made of bearing steel, and the contact surface of respective rollers is mirror finished with an arithmetic average roughness of 0.05 μm or less. The flat-surface roller's housing is fixed to the chamber bottom. On the other hand, the housing of the spherical-surface roller fixed on the stage supported by the linear guide can slightly move in the radial direction of the roller, making it capable of applying any amount of radial direction load (contact force) by means of the hydraulic cylinder. Moreover, the intersection angle of the spherical-surface roller and flat-surface roller ϕ can be changed freely; thus, the spin angular velocity ω_{sp} at the contact area of both rollers can be adjusted (Figure 4). The ratio of spin angular velocity ω_{sp} to the spherical-surface roller's ω_0 (spin ratio $\gamma = \omega_{sp}/\omega_0$) is expressed as $\gamma = \sin\phi$. If the intersection angle of the roller axes is 0°, the spin ratio is 0. In this paper, these test conditions are referred to as pure rolling conditions.

During the test, the two rollers were driven at various numbers of revolutions with contact force applied, and the resulting torque at the roller axes was measured. Contact force is measured by a load cell installed between the back of the spherical-surface roller's housing and the hydraulic cylinder. The number of revolutions are measured by an electromagnetic rotation sensor, and torque is measured by an inductive flange type torque sensor directly connected to the axis. In addition, the rollers' operational surface temperature can also be measured during a test. As shown in Figure 4, the contact-type temperature sensor is fixed to a position, and 90° shifted from the flat-surface roller's ellipsoidal contact end.

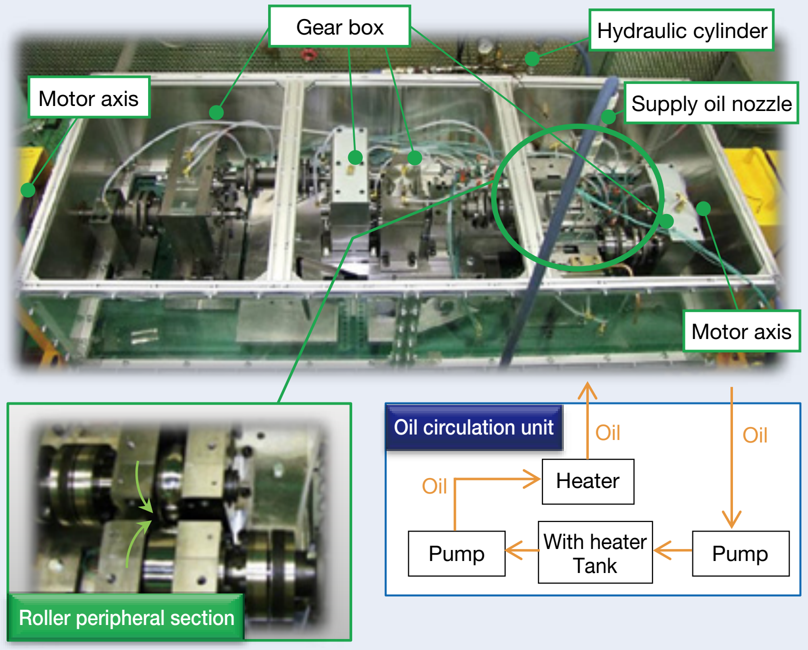

Fig 3. High-power two-roller traction tester[19)]

Table 1 and Figure 5 show the range (i.e., upper limit) of the operational conditions (contact surface pressure, peripheral speed, and spin ratio) that this tester can apply. A maximum contact surface pressure $P_{\max}$ at the rollers' contact area can be calculated with the rollers' dimension and contact force based on the Hertz contact theory. A maximum contact force measurable by the used load cell was 20 000 N, which, along with the dimensions of the rollers shown in Figure 4, leads to obtaining a maximum contact surface pressure ($P_{\max}$) of 3.52 GPa. Figure 5 shows the measurable range of the peripheral speed U and contact force F_c as well as transmission power Q ($= \mu F_c U$) on the assumption that a traction coefficient μ is 0.1. The figure also gives values measured by conventional testers in previous studies[11, 12], in addition to the values obtained by the tester. As shown in the figure, the tester has made it possible to measure traction curves under practical operating conditions where transmission power exceeds 100 kW, which had been impossible for conventional testers.

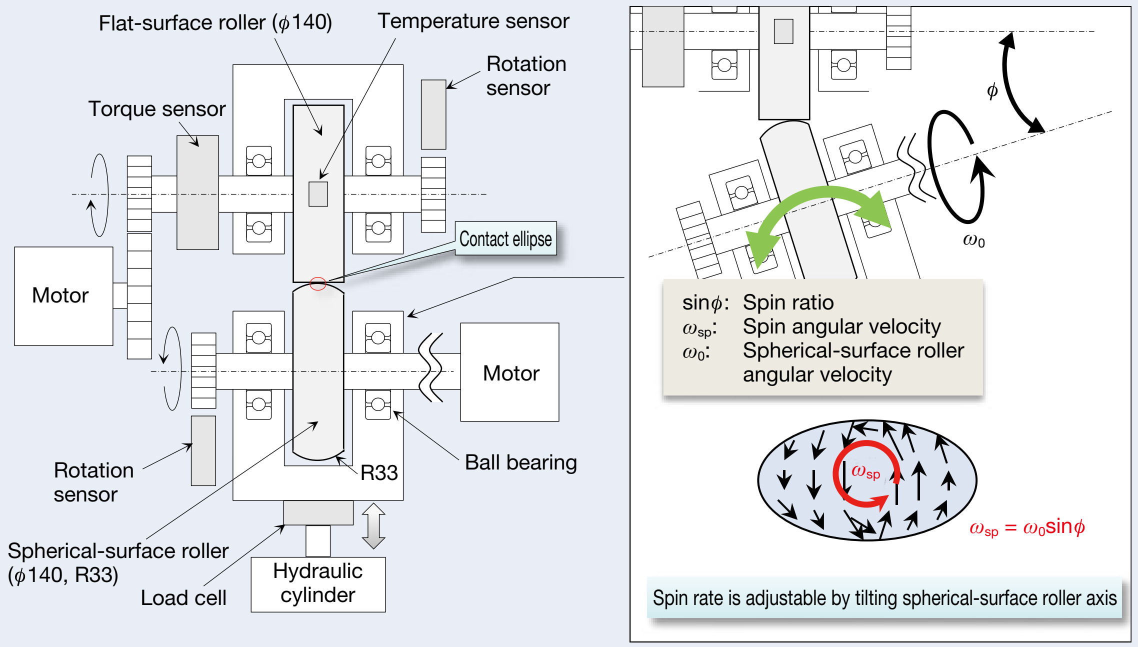

Fig. 4 Schematic view of the roller peripheral section of the high-power two-roller traction tester[19]

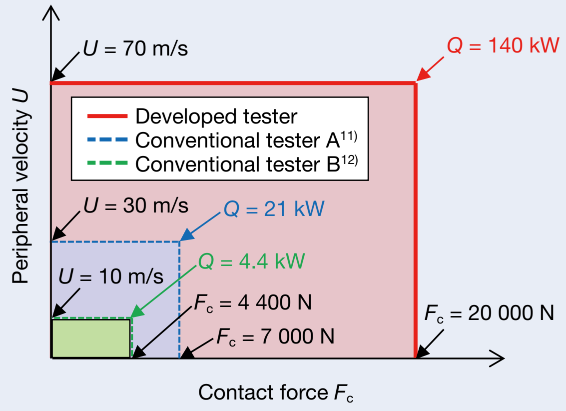

Fig. 5 Comparison of measurable contact forces and peripheral velocities[19]

Table 1 Measurable range of the developed tester (upper limit)

Operating conditions	Value
Maximum contact surface pressure $P_{\max}$	3.52 GPa
Peripheral velocity U	70 m/s
Contact force F_c	20 000 N
Spin ratio λ	0.29

2.2 Test method

This section describes the method of measuring the traction curves using the tester. In the test, while a certain contact force was being applied, the motor speed was controlled by the instructions, as indicated in Figure 6, in order to generate any degree of creep between the two rollers. Next, the steady response parts of the chronological data of the measured revolution of rollers, axis torque, surface temperature, and contact force were averaged and determined as the measurement value at each creep rate. A traction curve was then obtained by calculating the creep rate C_r, based on the measured revolution, and the traction coefficient μ, based on the measured torque and contact force. Creep rate is defined in this paper as the ratio of the difference in the peripheral velocity of two rollers to the peripheral speed of the flat-surface roller (see expression in Figure 6).

By means of the measurement method mentioned above, the traction curves were measured under various operating conditions. The properties of the traction oil used in the measurement are given in Table 2.

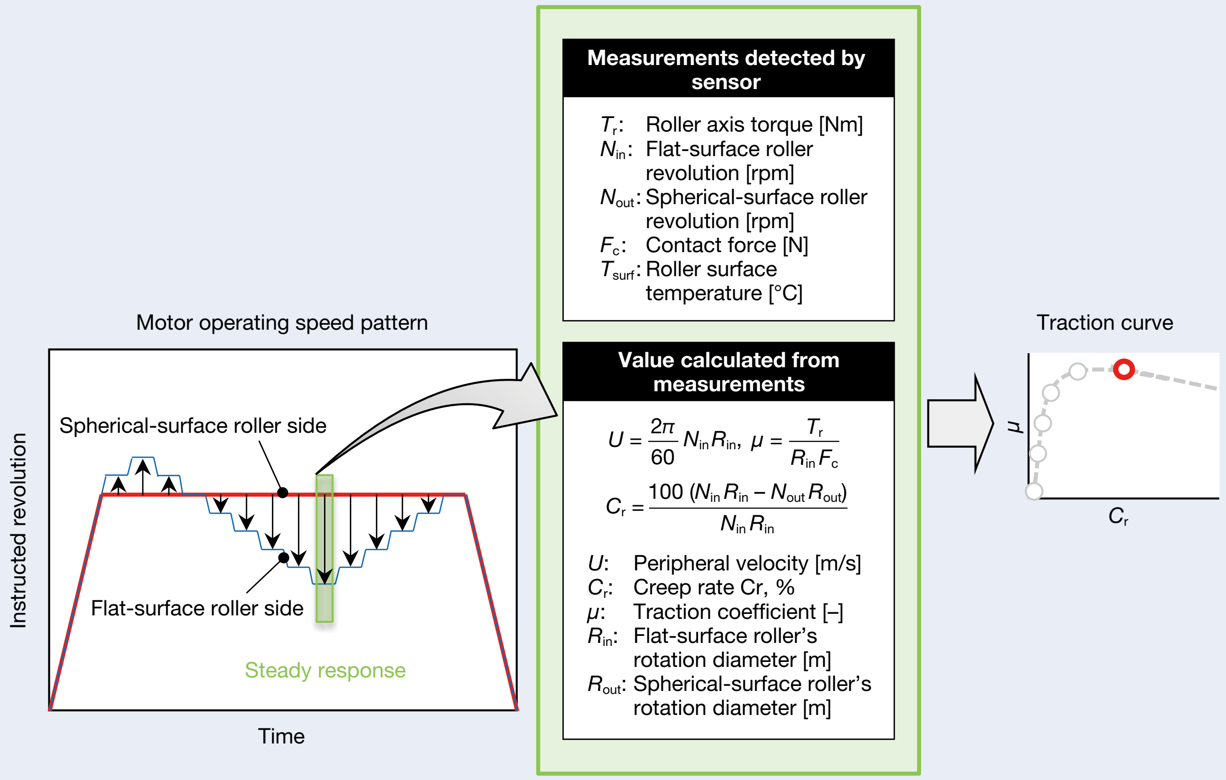

Fig. 6 Traction curve determination method[19]

Table 2 Rheological properties of traction oil

Rheological properties		Value
Density (15°C)		0.934 g/cm³
Kinetic viscosity	40°C	19.74 mm²/s
	100°C	4.45 mm²/s
Pressure viscosity coefficient	40°C	21.2 GPa⁻¹
	100°C	14.4 GPa⁻¹

3. Traction Curve under Pure Rolling Conditions

This section provides the measurement results of the traction curve under pure rolling conditions.

3.1 Comparison of traction curves

Figure 7 shows the traction curves measured at a supply oil temperature T_{oil} of 80°C. In the figure, measurements at a maximum contact surface pressure of 1.5 GPa are provided on the left (a) and at 3.5 GPa on the right (b). Comparing both (a) and (b) at the same peripheral speed, the greater a maximum contact surface pressure, the higher the traction coefficient becomes. A comparison under the same contact surface indicates that the faster the peripheral speed, the lower the traction coefficient. Moreover, after the traction coefficient reaches the greatest values, the reduction rate of the traction coefficient to the creep rate increases with the increase of peripheral speed. This is because the faster the peripheral speed, the greater the shear heat generation, which increases the temperature of oil film and decreases oil viscosity. On the other hand, few differences was observed in regard to the peripheral speeds when analyzing the start-up portion of the curves.

Figure 8 shows the traction curves measured at a peripheral speed of 70 m/s. In this figure, the measurements at a maximum contact surface pressure of 1.5 GPa are provided on the left (a) and at 3.5 GPa on the right (b). Figure shows that the lower a maximum contact surface pressure and the higher a supply oil temperature, the less the traction coefficient. Furthermore, it shows that the difference is more significant when the maximum contact surface pressure is low.

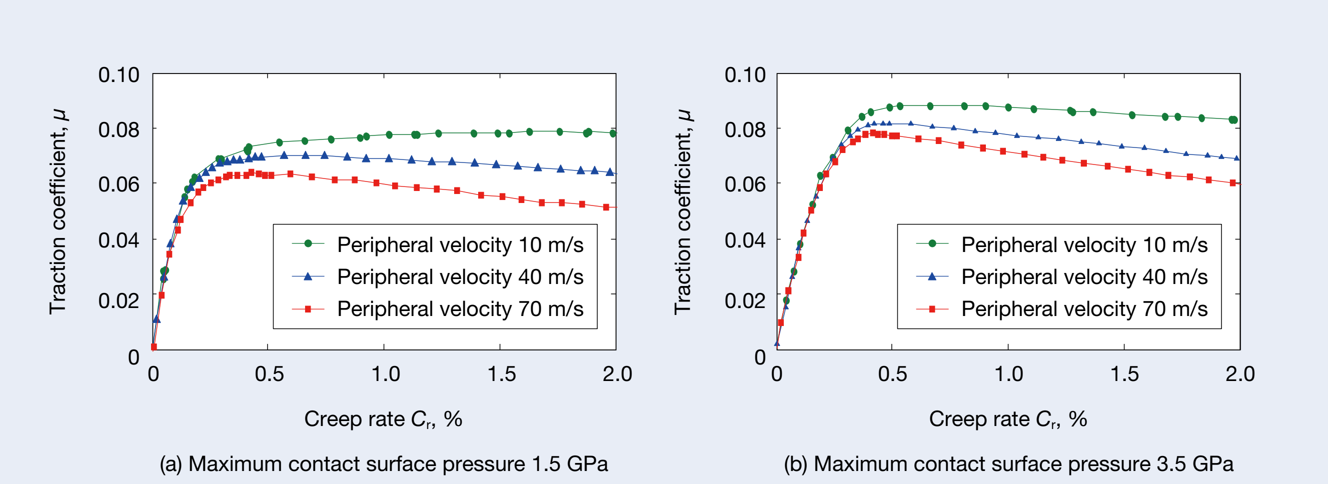

(a) Maximum contact surface pressure 1.5 GPa

(b) Maximum contact surface pressure 3.5 GPa

Fig. 7 Traction curves measured under pure rolling conditions (T_{oil} = 80°C)

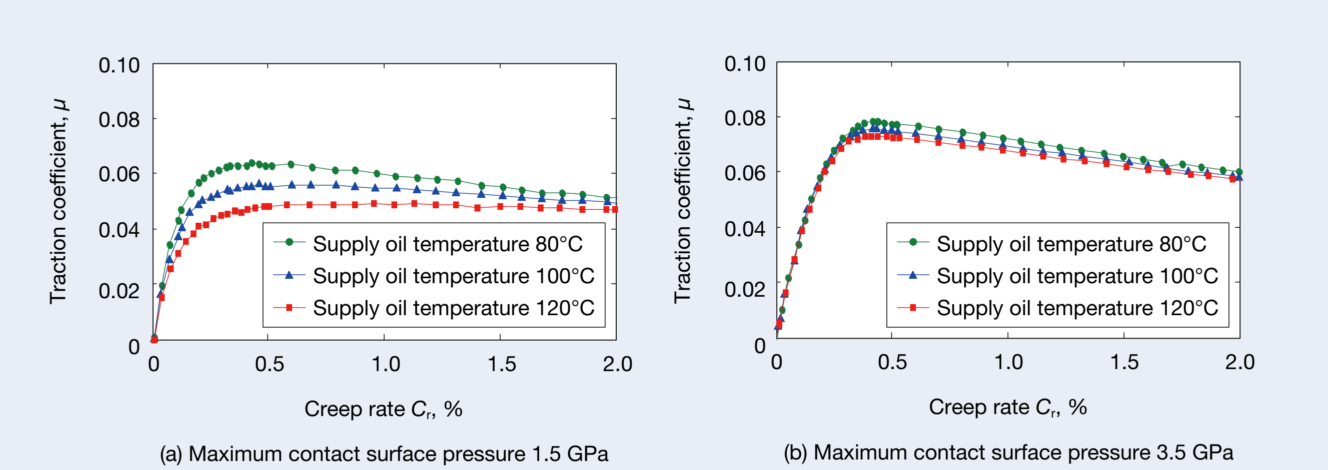

(a) Maximum contact surface pressure 1.5 GPa

(b) Maximum contact surface pressure 3.5 GPa

Fig. 8 Traction curves measured under pure rolling conditions (U = 70 m/s)

3.2 Comparison of maximum traction coefficients

The maximum traction coefficient μ_{max} and roller surface temperature at μ_{max} were obtained by measuring the traction curves, the results of which are shown in Figure 9. These were obtained under 42 different conditions combining two maximum contact surface pressures (1.5 and 3.5 GPa), 7 peripheral speeds (10, 20, 30, 40, 50, 60, and 70 m/s), and 3 supply oil temperatures (80, 100, and 120°C). The horizontal axis represents a maximum transmission power Q (= $\mu_{\mathrm{max}} F_c U$) under individual measurement conditions. As shown in Figure 9, the greater the transmission power, the higher the roller surface temperature; thus, the maximum traction coefficient decreases. The change rates of the roller surface temperature and that of the maximum traction coefficient are almost the same even under different supply oil temperatures, and they increase at lower maximum contact surface pressures.

The relationship between the roller surface temperature and maximum traction coefficient is shown in Figure 10. The figure also shows the measurement results obtained under 69 different conditions combining five maximum contact surface pressures (1.5, 2.0, 2.5, 3.0, and 3.5 GPa), 7 peripheral speeds (10, 20, 30, 40, 50, 60, and 70 m/s), and 3 supply oil temperatures (80, 100, and 120°C). As shown in Figure 10, the relationship between the roller surface temperature and maximum traction coefficient is represented linearly. Also, its gradient decreases with the increasing maximum contact surface pressure and becomes almost steady above certain maximum contact surface pressures.

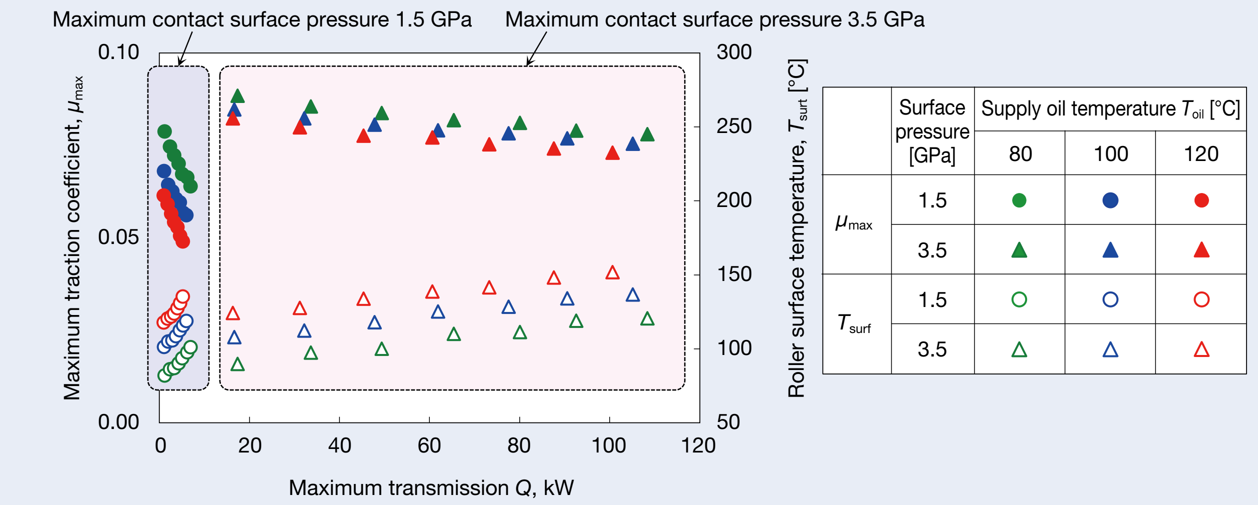

Fig. 9 Maximum traction coefficients and roller surface temperatures

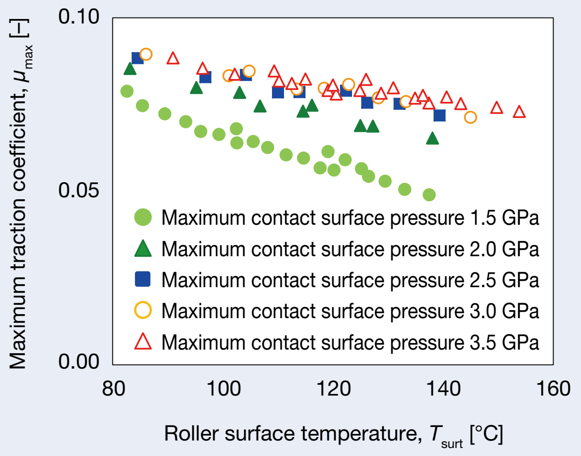

Fig. 10 Relationship between maximum traction coefficients and roller surface temperatures

4. Traction Curve under Spin Conditions

The high-temperature/high-power operational conditions of traction drive devices involve spin in most cases. That is why traction curves under spin conditions were measured in order to compare them with the measurements obtained under pure rolling conditions.

Figure 11 shows the measurements at a spin ratio of 0.29. In this figure, the measurements at a maximum contact surface pressure of 1.5 GPa are provided on the left (a) and at 3.0 GPa on the right (b). The figure also shows the results obtained at different peripheral speeds and supply oil temperatures as well as the data measured under pure rolling conditions.

As shown in Figure 11, at every peripheral speed, both the start-up portion of the gradients and the maximum traction coefficients are smaller in spin conditions than in pure rolling conditions. Also indicated is that the difference is more striking when a maximum contact surface pressure is high. In the high creep area after the traction coefficients reach the greatest values, the gradients are almost the same both in the pure rolling conditions and in the spin conditions. This is probably because the higher the creep rate, the greater the pure rolling component is against the spin component on the whole, which consequently produces less difference in the traction coefficients between the pure rolling conditions and the spin conditions.

5. Conclusion

In order to facilitate the R&D of more compact, lightweight, and efficient traction drive devices, we developed a two-roller traction tester to enable measurement of traction curves in ways that were never before possible under conditions similar to those faced by the practical traction drive. This paper details the configuration of the tester and shows several resulting traction curve measurements under varied operating conditions.

Data obtained by this high-power two-traction tester will make measuring and estimating traction curves under practical operating conditions possible, thereby contributing to ensuring the functionality of traction drive devices and promoting their optimal design.

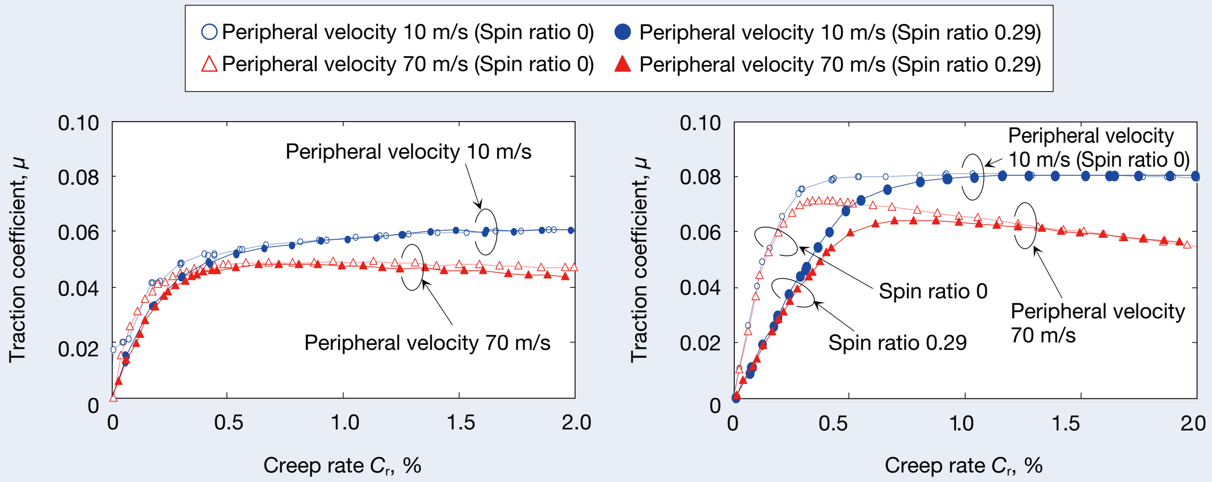

(a) Maximum contact surface pressure 1.5 GPa, supply oil temperature 120°C

(b) Maximum contact surface pressure 3.0 GPa, supply oil temperature 120°C

Fig. 11 Influence of spin motion on traction curves

References

1) T. Makino and T. Kawase, "A calculation of traction properties based on a non-linear viscoelastic model (Part 1) Measurement of traction and curve fitting," Journal of Japanese Society of Tribologists, 43–5 (1998) 421–428.
2) H. Tanaka, "Toroidal CVT," (2000) 13-24, CORONA PUBLISHING CO., LTD.
3) T. Mawatari, A. Nakajima, and H. Matsumoto, "Shear Stress Analysis of EHL Oil Films Based on Thermal EHL Theory—Effect of Inlet Oil Temperature" Tribology Online, 3, 5, (2008), 268–273.
4) M. Tomita, M. Tabuchi, and T. Sano, "Examination of the maximum traction coefficient prediction method (First report)," Proceedings of 2011 JSAE Annual Congress (Spring), 35–11 (2011) 1–4.
5) M. Tomita, T. Sano, and M. Inoue, "Examination of the maximum traction coefficient prediction method (Second report)," Proceedings of 2012 JSAE Annual Congress (Autumn), 119–12 (2012) 5–8.
6) T. Sano, M. Tomita, M. Inoue, Y. Takeuchi, and M. Yorinaga, "Study of the Prediction Method for Maximum Traction Coefficient," SAE International Journal of Passenger Cars—Mechanical Systems, 6, 2, (2013), 568–577.
7) M. Muraki and Y. Kimura, "Influence of temperature rise on shear behavior of an EHL oil film," Transactions of the JSME Ser. C, 56–528 (1990) 2,226–2,234.
8) K. Katoh, T. Iwasaki, M. Kato, and K. Inoue, "Evaluation of limiting shear stress of lubricants by roller test," Transactions of the JSME Ser. C, 58–546 (1992) 558–564.
9) H. Achiha, S. Natsumeda, Y. Nakamura, and I. Fujishiro, "Traction characteristics under high contact pressure, high rolling speed and high temperature," Proc. International Tribology Conference Yokohama 1995, 1, (1996), 139–144.
10) N. Oono, H. Achiha, S. Natsumeda, S. Aihara, and F. Hirano, "High pressure rheology and traction characteristics of traction oil," Journal of Japanese Society of Tribologists, 44–12 (1999) 965–972.
11) H. Hata, T. Gouda, and M. Koishi, "Traction Performance of Traction Fluid under the Severe Conditions," Proc. International Tribology Conference Nagasaki 2000, 1, (2000), 603–607.
12) L. D. Wedeven, G. G. Wedeven, S. H. Kratz, T. E. King, J. L. Linden, F. Caracciolo, and D. G. Mcwatt, "USCAR traction test methodology for traction-CVT fluids," SAE Technical Paper, No. 2002-01-2820, (2002), 1–31.
13) L. D. Wedeven, T. E. King, J. L. Linden, F. Caracciolo, and D. G. McWatt, "WAMhs Traction Machine and Test Methodology for USCAR," Proc. 13th International Colloquium Tribology, Esslingen, (2002), 1,873–1,887.
14) H. Hata, S. Aoyama, and T. Miyaji, "Performances and characteristics of Idemitsu Traction Oils," IDEMITSU TRIBO REVIEW 28 (2005) 1–21.
15) T. Makino and T. Kawase, "Effects of spin on traction characteristics," Journal of Japanese Society of Tribologists, 44-1 (1999) 53–60.
16) Sanda, S. and Hayakawa. K., "Traction Drive System and its Characteristics as Power Transmission," R&D Review of Toyota CRDL, 40, 3, 2005, 30–39.
17) R. Kawabata and M. Muraki, "Traction perpendicular to rolling direction based on spin and side-slip," Transactions of the JSME Ser. C, 71–708 (2005) 2,643–2,650.
18) Y. Nakamura and M. Funahashi, "Oil solidified high-pressure traction curve estimation with spin by elastic contact mechanics," Transactions of the JSME Ser. C, 72–717 (2006) 1,653–1,659.
19) H. Itagaki, H. Hashiguchi, M. Kita and H. Nishi, "Development of a High-Power Two-Roller Traction Tester and Measurement of Traction Curves," Tribology Online, 11, 6, (2016), 661–674.

Itagaki Hirofumi

Kita Masahiro

Hashiguchi Hiroki

New Technologies for Bearings in Electric Vehicle and Hybrid Electric Vehicle Powertrains

Takanori Ooshima and Satoshi Masuda
Automotive Powertrain Bearing Technology Center

Abstract

Recent emission controls of vehicle pollutants, such as CO_2 and NOx, have led to increased use of hybrid electric vehicles (HEVs) and electric vehicles (EVs) all over the world. The use of these vehicles is likely to spread further since they offer other advantages such as low fuel consumption and good acceleration performance. Bearings used in HEVs and EVs require good performance at high rotating speeds, high static strength, long life, low frictional torque, creep resistance, low noise, and low vibration. In this article, we will introduce some of NSK's latest bearing technologies created in response to these requirements.

1. Introduction

A solution for recent emission controls of vehicle pollutants such as CO_2 and NOx, hybrid electric vehicles (HEVs) and electric vehicles (EVs) have been in the spotlight and introduced worldwide as new drive systems that differ from automatic transmissions (ATs) and manual transmissions (MTs)[1].

HEVs and EVs have the advantage of improving fuel efficiency and acceleration performance, with equal or even less CO_2 and NOx emissions compared to gasoline and diesel vehicles. For these reasons, development of HEVs and EVs with various structures is expected, and both types of vehicles will likely become widely used around the world in the years ahead.

This paper takes a look at performance and new technology requirements for bearings used as key components for HEV and EV powertrains.

2. Performance Requirements of Bearings for HEV and EV Powertrains

HEVs and EVs are currently in the spotlight owing to their excellent environmental performance. However, to utilize their advantages, such as power performance, bearings must have a range of capabilities, as shown in Figure 1.

To illustrate how bearings for HEV and EV powertrain are used, Figure 2 shows a cross section of an HEV unit for an FF HEV[2]. Various types of bearings are used for such applications as motor support and power transmission gear support, and Table 1 shows a list of the related bearings in use.

More compact and lightweight

In view of improving fuel efficiency and packaging size, efforts have been made to make individual components more compact and lighter, which applies to bearings as well. However, the more compact and lightweight a bearing becomes, the lower its load capacity. Therefore, the life and static strength of the bearing is also reduced. Technologies that improve the life and static strength are thus vital in downsized bearings in order to ensure their durability and reliability.

Greater efficiency

Automakers are committed to improving the efficiency of powertrains by using various technologies, and automobile fuel mileage has also been improving year after year. To reduce the mechanical loss of the HEV or EV unit, demand is growing for a reduction in bearing torque (loss reduction), and companies are promoting efforts to improve each type of bearing, which includes a reduction of rolling or sliding friction and agitating loss.

Electrification

In view of improvements in efficiency and maximum motor-driven vehicle speed, efforts are being made to downsize motors and increase high-speed rotation. With the trend toward high-speed rotation of motors, there are cases in which bearings are used under conditions that exceed the conventionally permissible rotating speed. Various types of bearings must therefore be suitable for these high speeds.

Noise reduction

In motor-driven automobiles such as HEV and EV interiors, which are very quiet, there are cases in which the comfort of passengers can be affected due to operating noise from powertrains, previously almost unnoticeable. Reductions of noise and vibration are thus required in order for the bearings to be usable not only on their own but also with peripheral components.

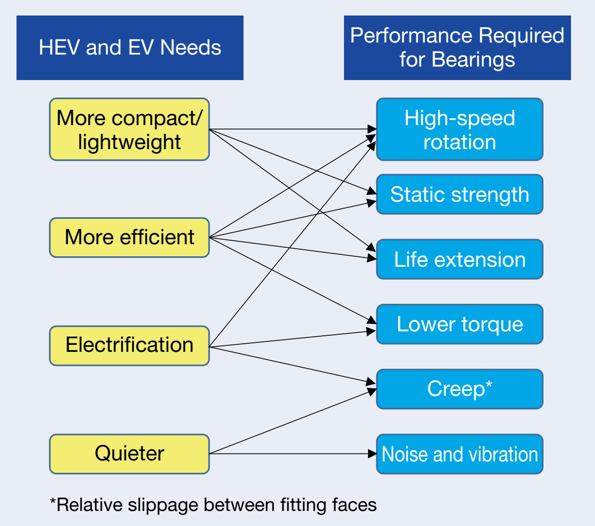

*Relative slippage between fitting faces

Fig. 1 Performance requirements of bearings for HEV and EV powertrains

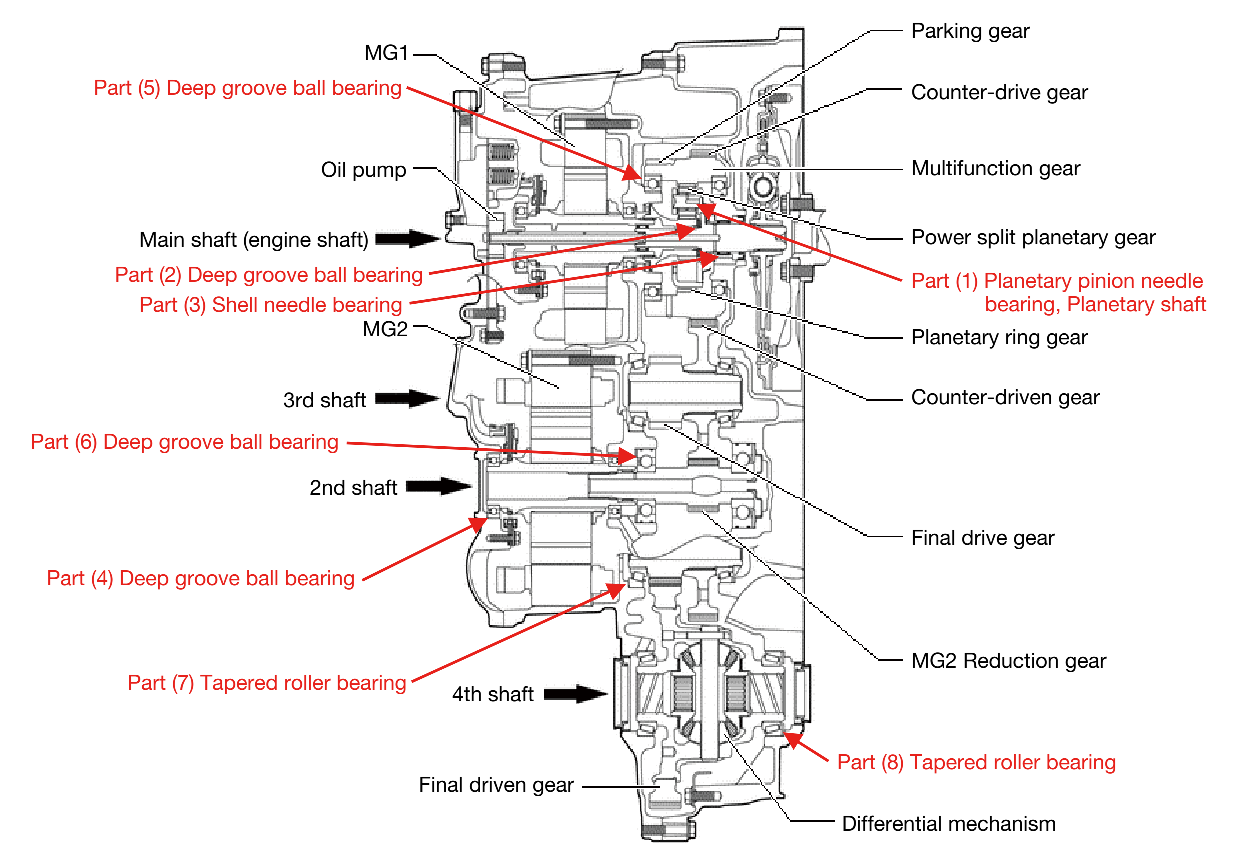

Fig. 2 Cross section of an FF HEV[2]

Table 1 Location of bearings in an FF HEV

Point of Use			Bearing Type
1	Planetary gear		Planetary pinion needle bearing Planetary pinion shaft
2	Between planetary gears		Thrust needle bearing
3	Shaft/ needle support	Main shaft	Shell needle bearing
4		Motor	Deep groove ball bearing
5		Counter-drive gear	Deep groove ball bearing
6		2nd shaft	Deep groove ball bearing
7		3rd shaft	Tapered roller bearing
8		4th shaft	Tapered roller bearing

3. Bearing Technology Trends in the Area of HEV and EV Powertrains

3.1 Measures for high-speed rotation

3.1.1 Ultra-high-speed planetary cage and roller

Cage and roller-type needle bearings are widely used in planetary gears, a power distribution mechanism that causes an input torque to branch into a direct path to the wheel axle and a path leading to the motor. Where the number of rotations and revolutions in a planetary gear increases as a result of the trend toward higher speeds, high-temperature friction heat is generated in the needle bearing cage and the moving part of planetary gear (Figure 3). This may cause damage to the moving surface from friction, such as galling and heat cracks[3)].

In response to demand for faster speeds, NSK developed a high-speed adaptable planetary cage and roller with improved cage wear resistance (Figure 4). The durability of the cage was improved by applying a chemical film onto the surface, which reduced the friction heat on the sliding surface[4)].

In recent years, along with ever-growing demand for faster speeds, other requirements are surging for lowering the viscosity and amount of oil in order to reduce the agitation resistance of the lubrication oil in the HEV and EV units. To address this, by applying another special film onto the upper layer of the aforementioned chemical film, NSK has developed and added to its portfolio an ultra-high-speed planetary cage and roller, which has about 1.5 times higher wear resistance compared to that of NSK's high-speed specification product. Table 2 shows NSK's product lineup for each cage specification, for the purpose of introducing optimal high-speed adaptable planetary cages and rollers, depending on the severity of the operating environment.

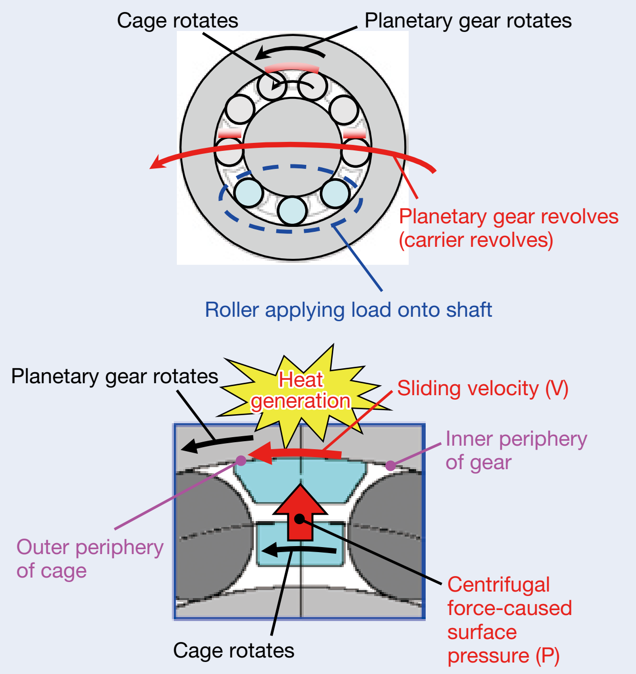

Fig. 3 Operating environment of the planetary cage and roller

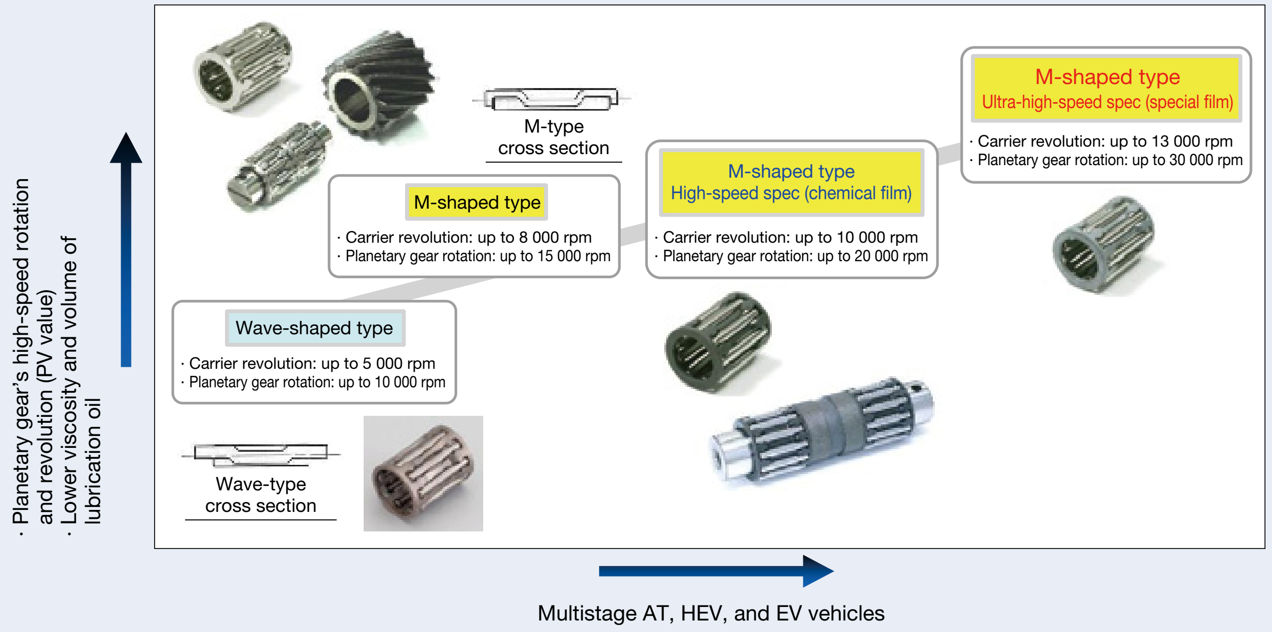

Fig. 4 Development history of the planetary cage and roller

Table 2 M-type cage and roller product lineup

	Conventional Technology		New Product
	Conventional product	High-speed spec	Ultra-high-speed spec
Appearance			
Cage surface texture	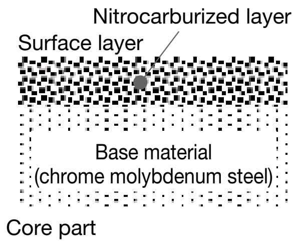	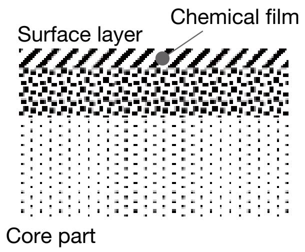	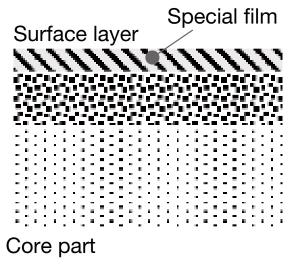
High-speed endurance (wear resistance)			1.5 times Twice

3.1.2 Ultra-high-speed ball bearing

The internal conditions of a bearing under high-speed rotation are shown in Figure 5, and there are cases in which inadequate lubrication or friction between the race surface and balls will result in abnormal heat generation, wear, and cage destruction as centrifugal force increases[5].

By controlling the oil flow inside the bearing and optimizing the internal dimensions, NSK developed an ultra-high-speed ball bearing that can be used even in a range that significantly exceeds the permissible rotating speed of conventional bearings.

To solve the inadequate lubrication problem in the inner ring side due to centrifugal force caused during ultra-high-speed rotation, a plate was installed onto the side surface on the lubricant inflow side in order to optimize an oil flow inside the bearing, as shown in Figure 6.

In addition, by optimizing the internal design such as the groove curvature of the raceway, ball diameter, and pitch diameter, the slip amount was reduced between the balls and raceway. This lowers the *PV* value (*P*: surface pressure, *V*: slip velocity) by approximately 30%. The cage, made of light plastic, is self-lubricating. Since there are cases in which a cage may become deformed and even destroyed due to excessive stress caused during high-speed rotation, the design of the cage was made in accordance with operating conditions in order to prevent fracture beforehand.

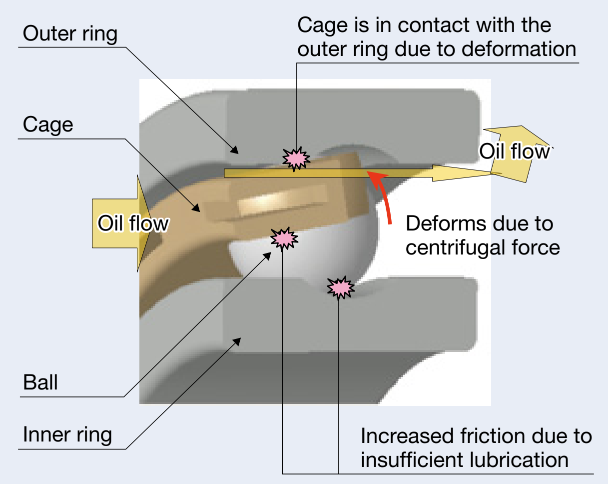

Fig. 5 Internal conditions of a bearing under high-speed rotation[5]

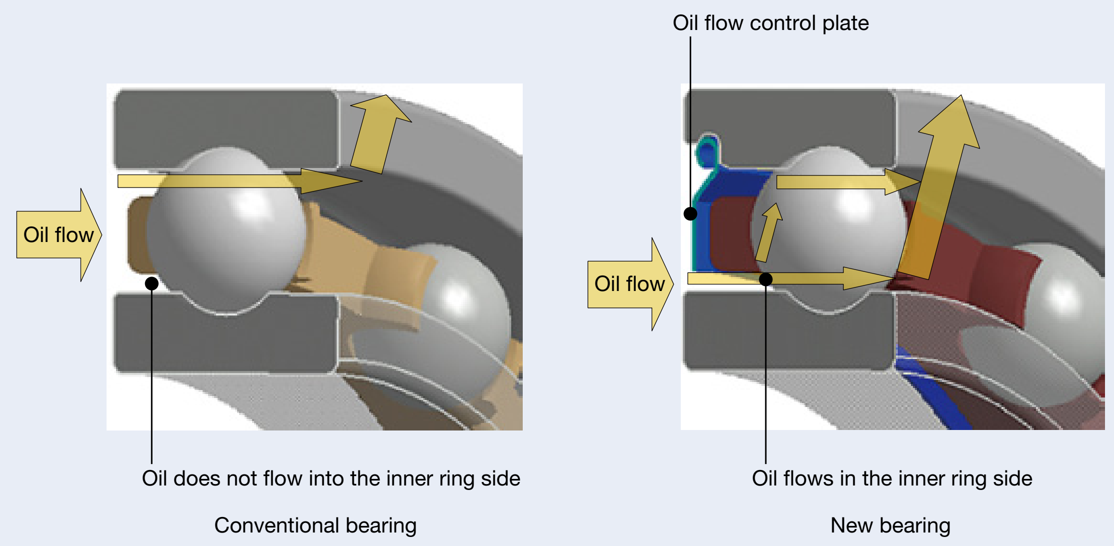

Conventional bearing

New bearing

Fig. 6 Comparison of lubricating conditions for the new and conventional bearings[5]

Figure 7 shows the results of a high-speed durability test of the new product. Heat seizure occurred in the inner ring raceway immediately after a conventional product was tested at a rotation of 30 000 rpm, whereas no damage, such as heat seizure, was observed in the new product, thus enabling the development of a product that is suitable for high-speed rotation.

3.2 Improvement of static strength

3.2.1 Tapered roller bearing with a special crowning

By using a special crowning on the raceway, NSK has developed a tapered roller bearing that is more compact and lightweight than conventional products, while also ensuring that the life and rigidity are equivalent to or better than those of conventional products.

When a load is applied to the contact face of the raceway and roller, as shown in Figure 8, a phenomenon called edge load occurs, increasing the contact surface pressure locally. This can result in premature failure due to stress concentration. For this reason, a slight convex shape, called "crowning," had been placed on the rolling contact surface to reduce the contact surface pressure. When used under high load conditions, however, edge load still occurred; thus, a larger bearing size was used to lower the contact surface pressure and suppress edge load.

In the new product, the raceway surface was processed into a barrel-shaped surface, called special crowning, and the internal design was also optimized in accordance with operating conditions. By doing this, the new product was designed to be suitable for high load conditions, as it is capable of suppressing edge load without having to be larger.

Figure 9 shows an application example of the new product. By applying the special crowning with additional crowning amount added at both ends, edge load is suppressed. Moreover, the optimization of the internal design achieved a weight reduction of approximately 20% compared to conventional products.

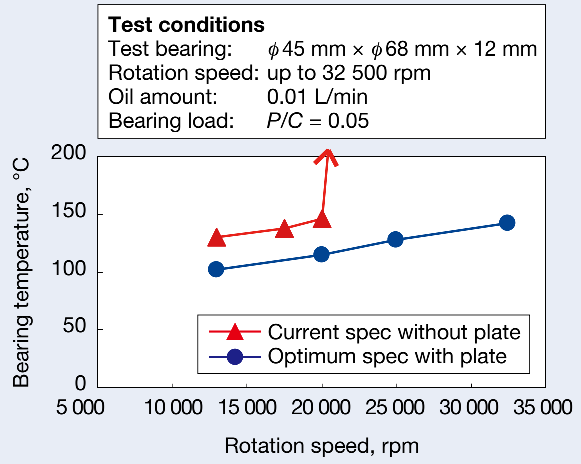

Fig. 7 Frictional-heat-generation test results[5]

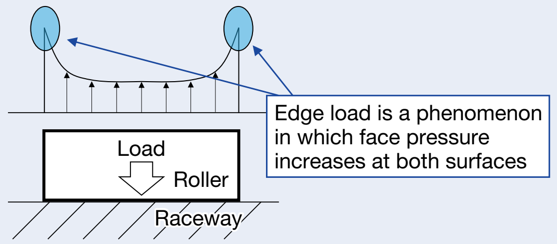

Fig. 8 Edge load on the contact face

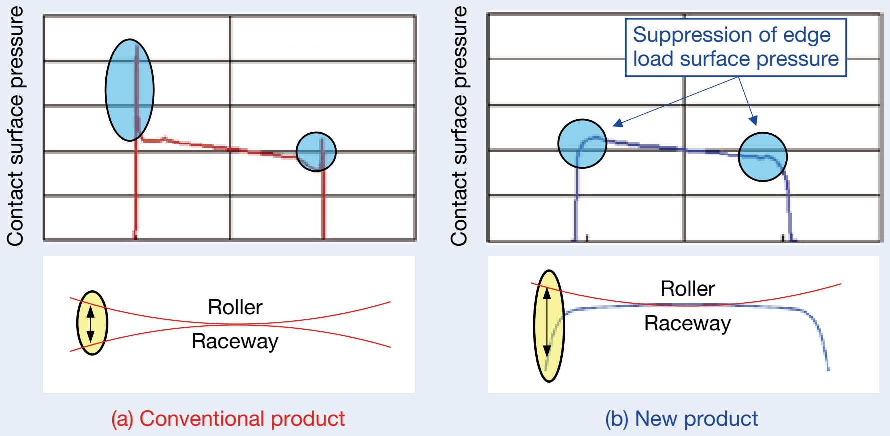

(a) Conventional product

(b) New product

Fig. 9 Contact pressure between the roller and raceway

3.3 Life extension

3.3.1 Extra Quality Tough Ball Bearings for Transmissions (EQTF)

For high-speed rotation of HEV and EV powertrains, when the lubrication environment degrades, flaking may occur at the surface due to a deterioration of the surface texture, which is caused by insufficient oil film between the race surface and balls.

Following a comprehensive study of the mechanism that results in surface-originated flaking, NSK developed EQTF, which extends bearing life by strengthening the rolling elements.

As shown in Figure 10, tangential force caused by the rolling element is acting at indentation fringes of the race surface, producing cyclic stress in association with the load movement. In regard to Figure 10, tangential force-induced tensile stress that is greater than compressive stress causes a crack at the right fringe[6] and flaking. Figure 11 shows the results of a test conducted to confirm the influence of tangential force on bearing life when the surface texture is changed against the raceway under the same indentation conditions. It was found that the coarser the ball's surface roughness, the greater the tangential force acting on the indentation fringes of the raceway, and life is thus shortened[7].

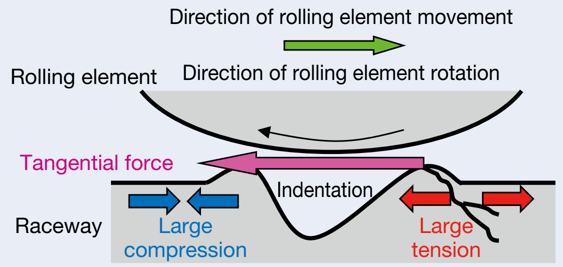

Fig. 10 Tangential force acting on the race surface

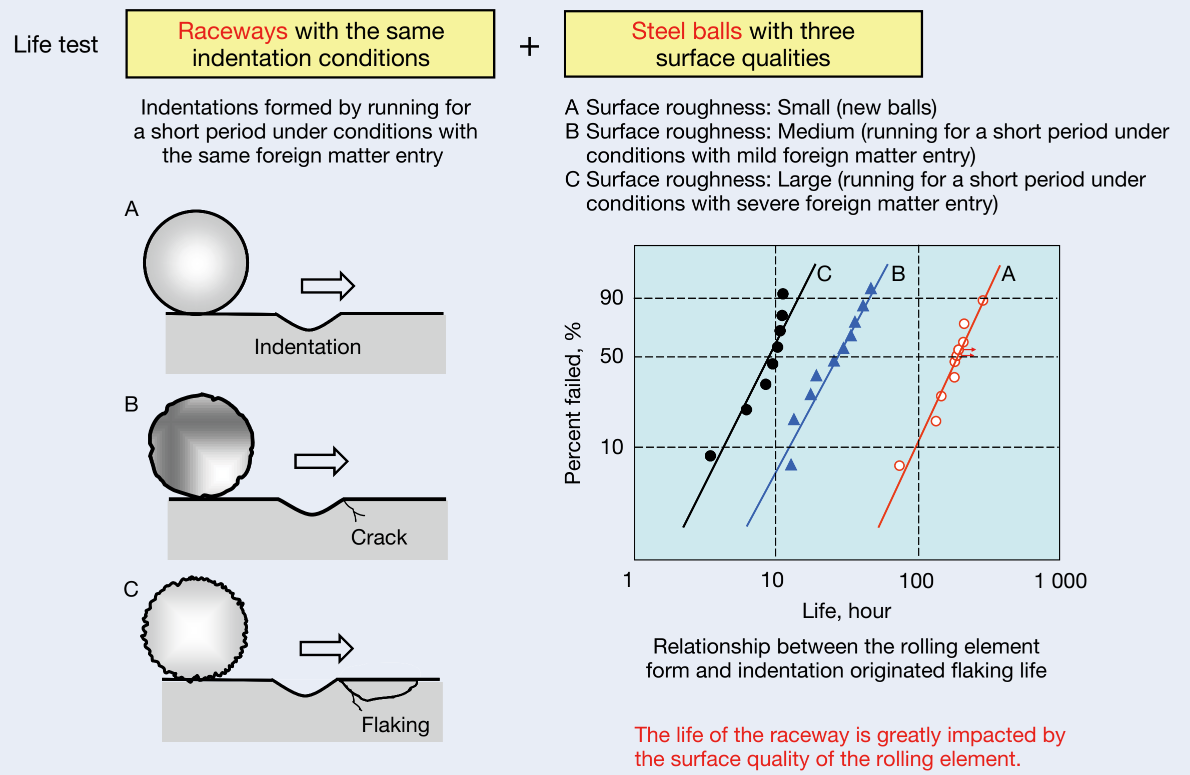

Relationship between the rolling element form and indentation originated flaking life

The life of the raceway is greatly impacted by the surface quality of the rolling element.

Fig. 11 Impact of rolling element surface roughness on flaking life

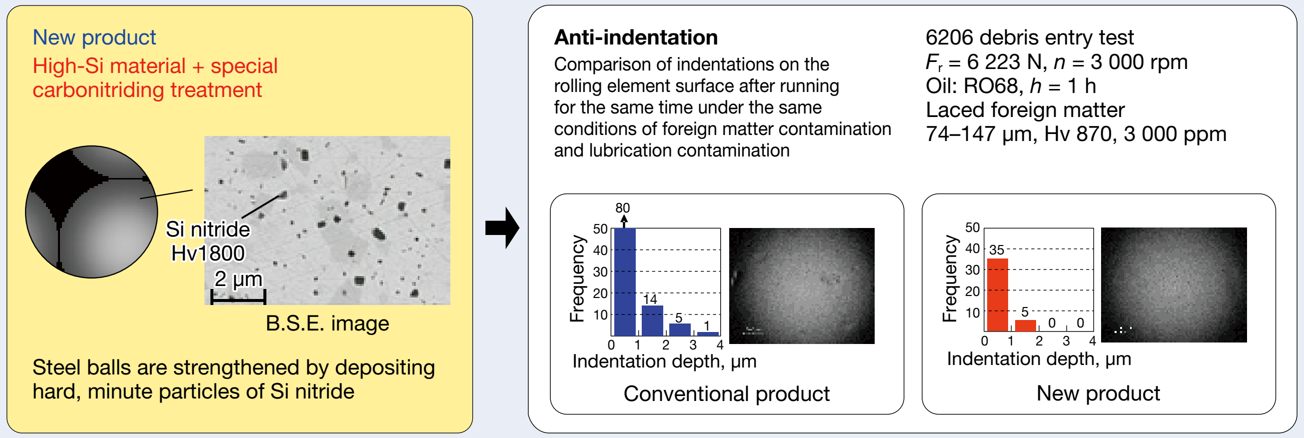

Steel balls are strengthened by depositing hard, minute particles of Si nitride

Fig. 12 Development features

The rolling elements, made from material with higher Si content than typically used quenched and tempered SUJ2, undergo a special carbonitriding treatment. As shown in Figure 12, the rolling element surface is strengthened by depositing super-hard Si nitride, which improves anti-indentation and thus prevents deterioration of the surface texture.

Figure 13 shows the life test results of the new product. They indicate a more than double life extension effect when compared to conventional SUJ2 products. Moreover, the new product can be used in combination with NSK's other life extension (TF) technology, which can further increase the life extension effect depending on the combination used.

Test bearing: 6206
Test conditions
F_r = 6 223 N, n = 3 000 rpm
Oil: RO68, h = 1 h
Laced foreign matter: 74–147 μm, Hv 870, 3 000 ppm

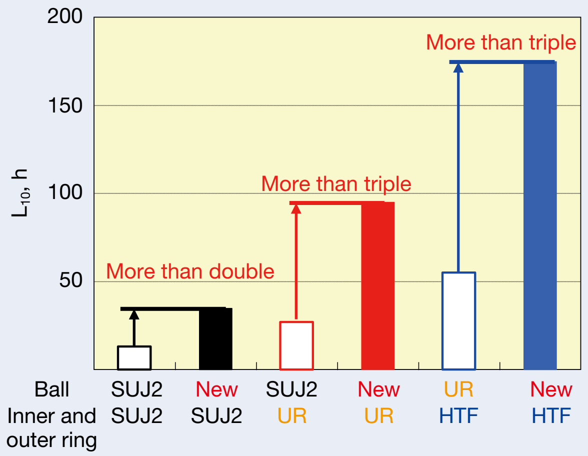

Fig. 13 Life test results

3.3.2 Ultra-long-life planetary shaft (Figure 14)

Planetary shafts used in planetary gears are fixed to a carrier plate using a pin setting method (Figure 15), or the staking-type method (Figure 16). NSK has a broad range of products in its lineup meeting the needs for long service life and resistance under severe conditions, as well as more compact and lightweight units, for each shaft fixation type.

(1) Long-life SUJ2 steel planetary shaft

NSK supplies JIS SUJ2 steel-based products of special heat treatment specifications that have undergone a unique nitrocarburizing process or have a special induction hardening specification that suppresses the thermoplastic bend in a high-temperature environment. Adding adequate residual austenite, carbonitride, compressive residual stress, etc., onto the rolling surface, the former has an improved endurance fatigue strength and is mainly applied to the pinning type. Retaining the equivalent rolling surface layer property to that of special heat treatment specification products, the latter has improved endurance fatigue strength by suppressing the thermoplastic bend in a high-temperature environment and is mainly applied to the staking type.

(2) Ultra-long-life NSK original steel planetary shaft

To meet specifications for use under harsher environments, NSK has developed an ultra-long-life planetary shaft for the pinning fixation type, which has greater endurance fatigue strength than special induction hardening specification products as a result of applying a unique heat treatment process to NSK's original SHX3 steel (high-chrome case-hardening steel). Using NSK's developed steel suited for deteriorated lubrication environments, the new shaft has improved durability owing to a combination of NSK's own heat treatment processes, and it delivers about 2.5 times the endurance fatigue strength (Figure 17)[8].

As SHX3 steel is characteristically predisposed to harden even at around the shaft end, its application has been limited to the pinning type. NSK's new SHX3M steel further optimizes the chemical component of the original steel, and has added it to its portfolio of ultra-long-life planetary shafts for the staking fixation type (Table 3).

3.4 Lower torque

3.4.1 Tapered roller bearing with plastic cage

As a result of striving to lower the torque of tapered roller bearings, NSK has gradually achieved a lowering of torque, such as in the reduction of sliding or rolling friction (Figure 18), as well as downsizing by using life extension technologies.

Fig. 14 Ultra-long-life planetary shaft

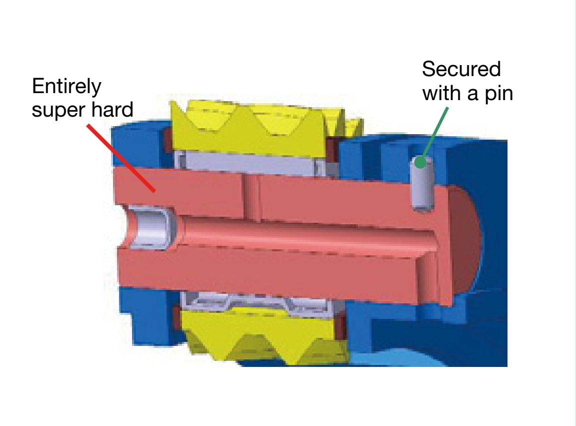

Fig. 15 Set pin

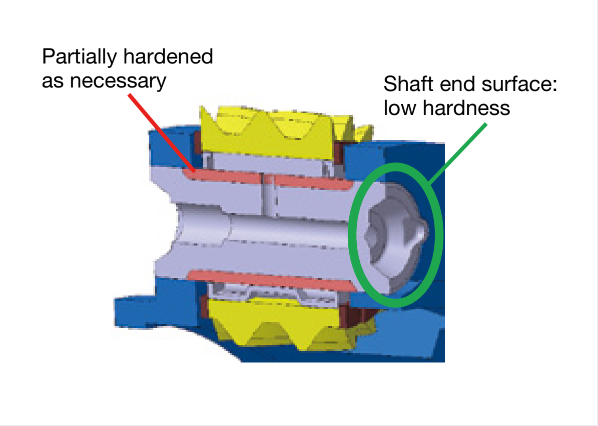

Fig. 16 Staking

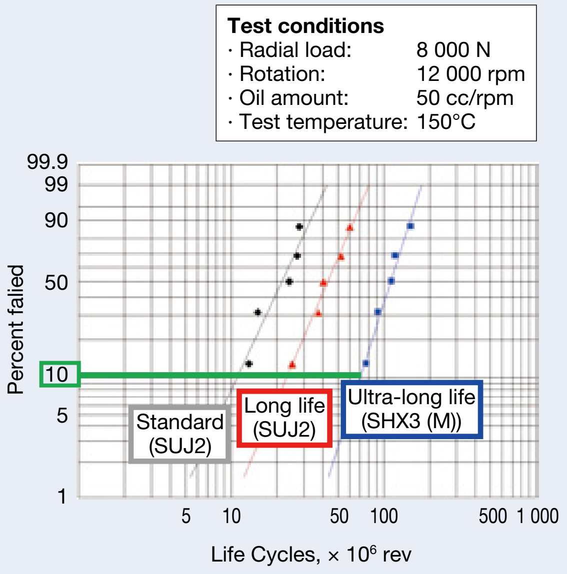

Fig. 17 Life test results[8]

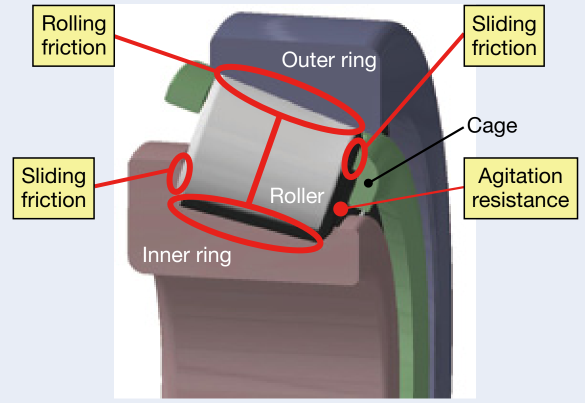

Fig. 18 Torque factors of a tapered roller bearing

Table 3 Planetary shaft product lineup

Fixation Method	Pinning Type	Staking Type
Standard spec (Service life comparison: 1)	JIS SUJ2 steel Quenching/annealing process	JIS SUJ2 steel Induction hardening quenching process
Long life spec (Service life comparison: 1.8)	JIS SUJ2 steel Special thermal process	JIS SUJ2 steel Special induction hardening quenching process
Ultra-long life spec (Service life comparison: 45)	SHX3 (NSK original) steel Special nitrocarburizing process	SHX3M (NSK original) steel Special nitrocarburizing process

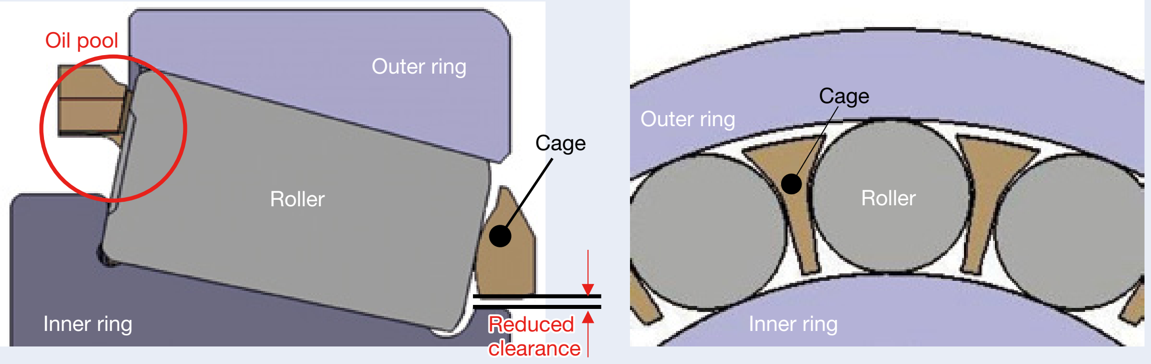

Fig. 19 Cross section of a tapered roller bearing with a plastic cage

To lower the torque even more, NSK developed bearings with improved seizure performance by reducing the agitation resistance of lubrication oil, which is a key driver of torque next to sliding and rolling friction, and by improving the lubrication property.

To reduce the agitation resistance, inflowing lubrication oil must be controlled. As shown in Figure 19, the clearance is narrow between the cage and inner ring front face rib from where the lubrication oil flows in, and the space between the rollers is filled by the cage. Thus, the optimized cage geometry facilitates torque reduction by about 20% (Figure 20)[9]. Additionally, the cage includes an injection-molding processable resin, allowing greater design flexibility.

Tapered roller bearings may face seizure when sliding friction increases at the contact surface between the inner ring large rib and the end face of the roller. Therefore, as shown in Figure 19, an oil pool is outfitted on the cage so that lubrication oil is supplied onto the contact surface of the roller's end face, which is subject to seizure (Figure 21). In unit testing, the new product demonstrated a seizure resistance of about 30% greater than that of a conventional product equipped with an iron cage.

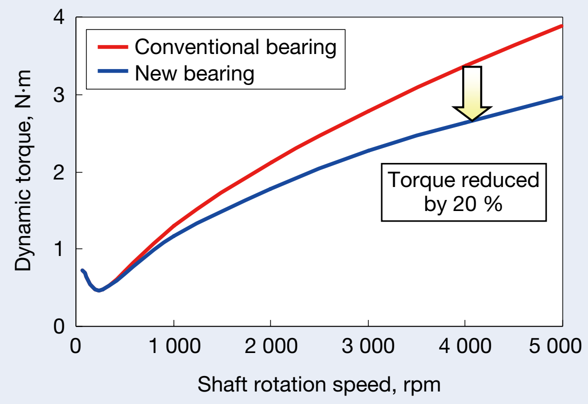

Fig. 20 Frictional torque of a rotating shaft[9]

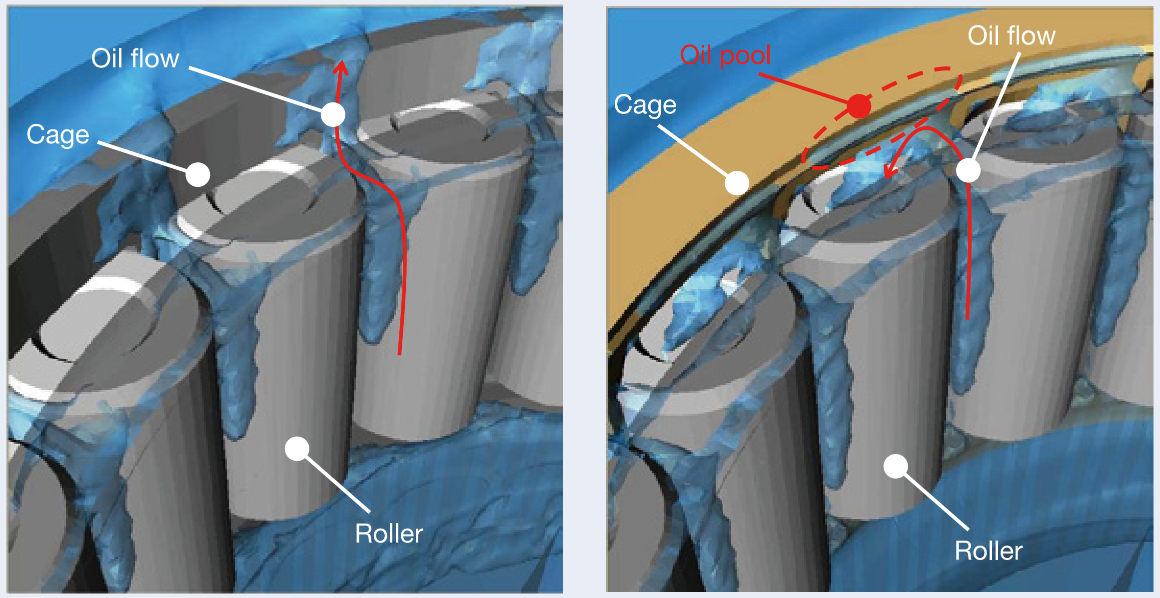

(a) Conventional product

(b) New product

Fig. 21 Oil flow[9]

3.4.2 Thin thrust needle roller bearing for planetary gear side (Figures 22 and 23)

As part of NSK's effort to lower the torque of planetary needle roller bearings, it has introduced friction loss-reduced cages and rollers, including all-roller type cage-and-roller products and compact cage-and-roller products that incorporate life extension technologies[10].

In regards to the mechanical loss in the planetary systems, NSK focused on reducing mechanical loss from moment loading in addition to the aforementioned reduction effort of cage-and-roller products that support the radial meshing load of planetary helical gears. When a planetary gear inclines due to moment load, the roller also rotates with an inclination, which causes friction loss due to the skew force-induced slide between the washer and planetary gear, placed at either end of the gear (Figure 24).

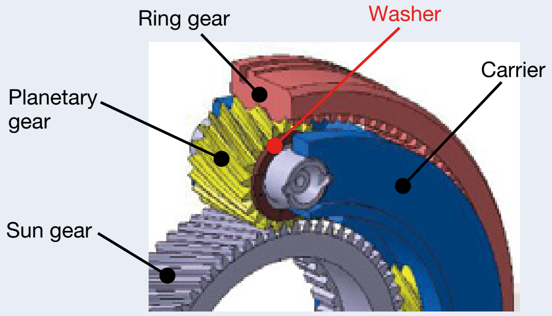

Fig. 22 Planetary mechanism

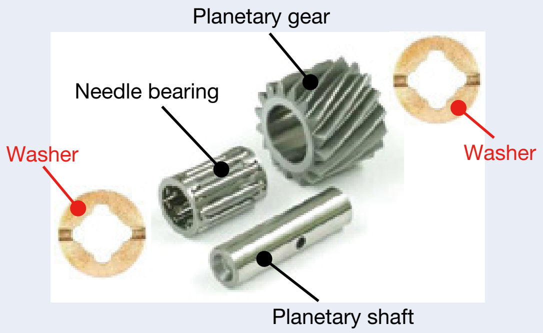

Fig. 23 Components of a planetary gear

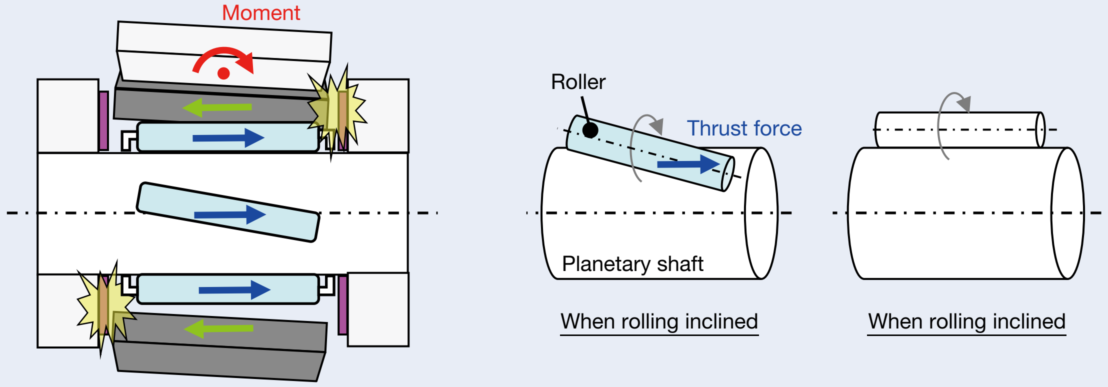

Fig. 24 Torque loss in a planetary gear

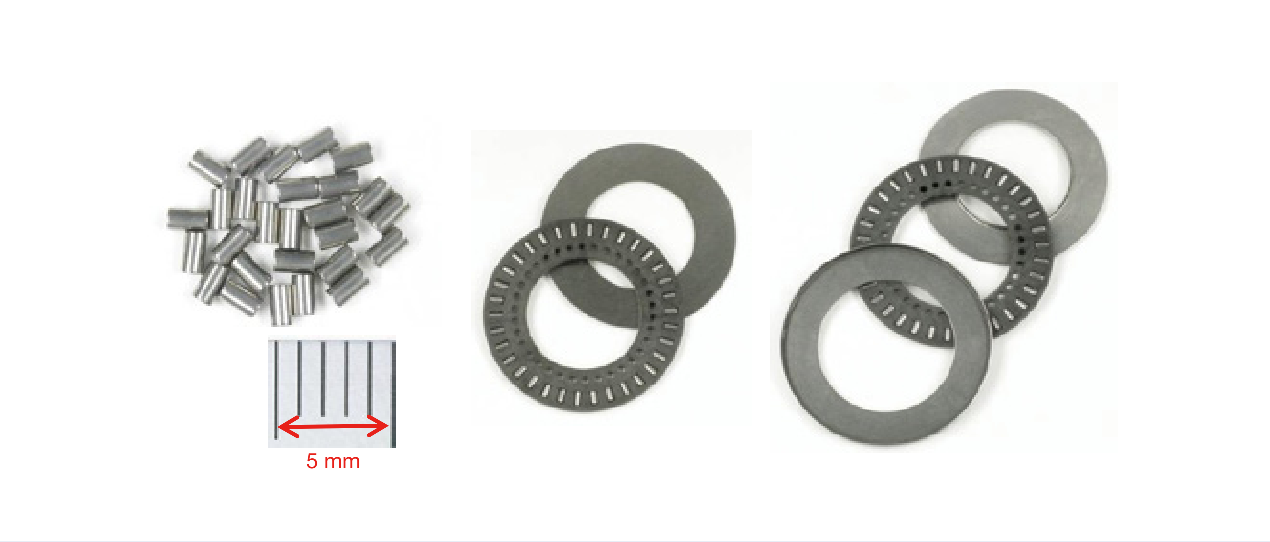

Fig. 25 Thin thrust needle roller bearing

To reduce this sliding friction, NSK developed thin thrust needle roller bearings that can easily replace other washers of the same product dimensions. The combination of the new, world's smallest level needle roller of 1 mm (diameter) × 1.8 mm (length) and a very thin race (Figure 25) of 0.2 mm (thickness) can be used to replace the washer. Moreover, the durability of the new product is guaranteed under high-speed rotation conditions of the planetary gear by including a plastic cage with a lubrication hole. It is expected that use of this bearing will reduce washer friction loss by around 70% (Figure 26).

3.5 Noise reduction (next-generation creep-free bearings)

There are cases in which the bearings for HEV and EV powertrains may receive an input of static load from the gear (i.e., load directed to a certain part) or of uneven eccentric load due to motor rotation (i.e., rotating load: the load with which the direction continuously varies). As for bearings with a loose fit, when such diversified loads are applied as the result of lightweight or high-speed motor rotation, a slip phenomenon of the bearings, known as creep, is very likely to occur. Once this happens, creep is most likely to lead to bearing wear, and their outer housings will eventually lead to noise and vibration.

When a static load is input, there is strain on the outer ring in a circumferential or radial direction, as shown in Figure 27 (a). When the inner ring and rolling element rotate, the strain distribution changes every time the rolling element passes the outer ring, as shown in Figure 27 (b). A part of the outer ring that extends ahead of the rolling element in a circumferential direction is pressed to move in the direction of the rolling element's movement.

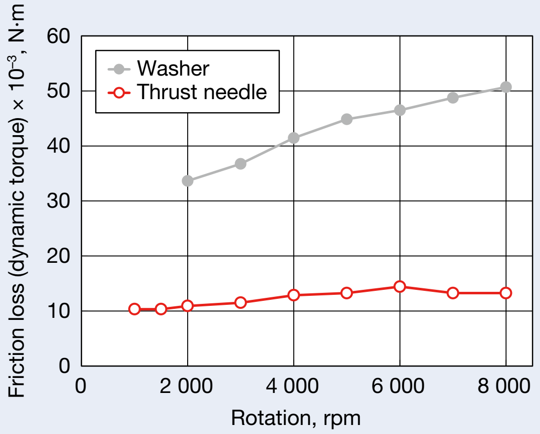

Fig. 26 Dynamic torque measurements

A part of the outer ring that contracts backward, in the rolling element, is pulled in order to move in the direction of the rolling element's movement[11]. This repetition makes the outer ring move in the same direction as that of the rotation of the inner ring, thereby generating creep.

When a radial load (F_r) is applied, as shown in Figure 28, the outer ring comes into contact with the housing that leans in the load direction. For rotating load, the contact face of the outer ring and housing also moves in the same direction, following the rotation of load F_r. Given that the difference between the housing inner diameter and the outer ring's outer diameter is c, the circumferential length difference between the two is πc. When the inner ring rotates one revolution, the outer ring falls behind with a length of πc on the circumference of the housing and moves in the opposite direction of inner ring rotation, generating creep[11].

To prevent creep, it is effective to fix the bearing to the case and/or to apply a Creep-Free Bearing equipped with an O-ring onto the outer ring's outer diameter face. However, fixing the bearing to the housing poses a challenge in terms of cost and assembly. Applying an O-ring to conventional products also presents a challenge in ensuring its oil resistance in a high-temperature oil environment.

NSK has developed next-generation Creep-Free Bearings, where creep from both static load and rotating load is suppressed by optimizing the internal design of the bearings as well as the O-ring dimensions.

To prevent creep caused by static load, the outer ring strain has been suppressed by optimizing the rigidity of the outer ring raceway through analysis. Additionally, for creep caused by rotating load, the creep-prevention effect was enhanced with the elasticity and constant compression of the O-ring, even in a high-temperature oil lubrication environment, made possible by the optimization of the high-temperature oil resistant material of the O-ring outfitted onto the outer ring as well as that of O-ring interference (Figure 29).

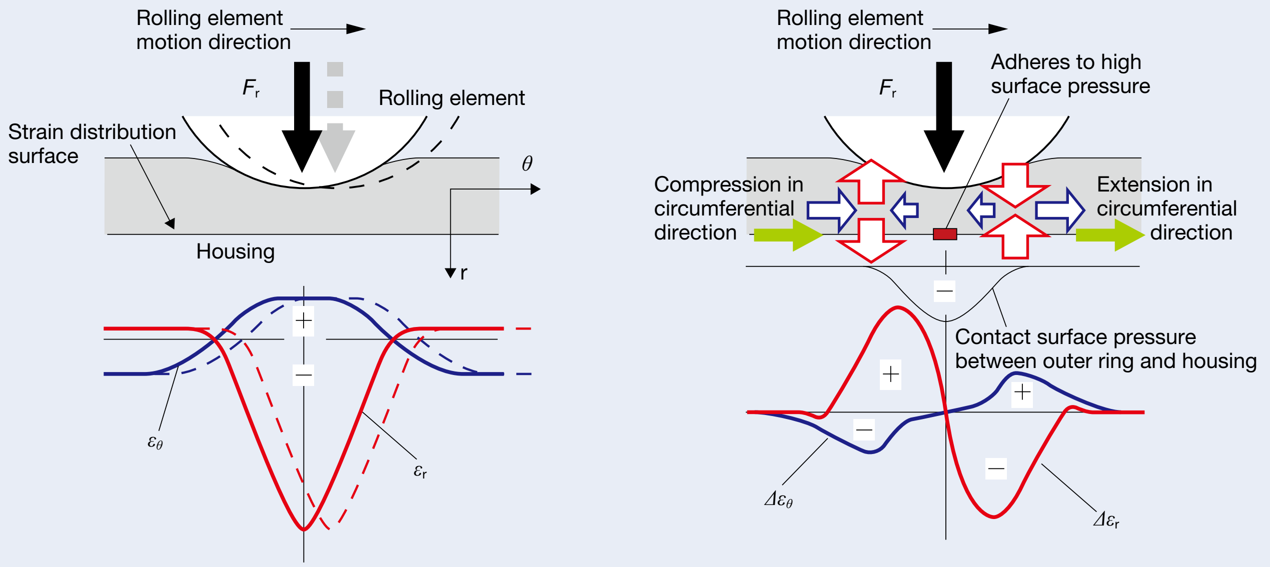

(a) Outer ring strain distribution due to rolling element load

(b) Distribution of strain change in the outer ring when the rolling element is passed

Fig. 27 Generation of outer ring creep due to unidirectional load[12]

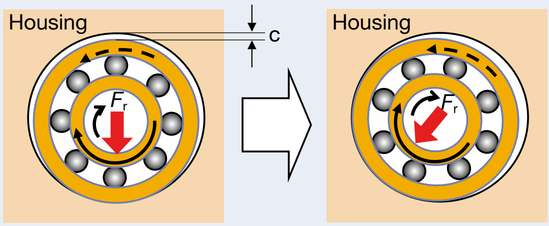

Fig. 28 Generation of outer ring creep due to rotating load[11]

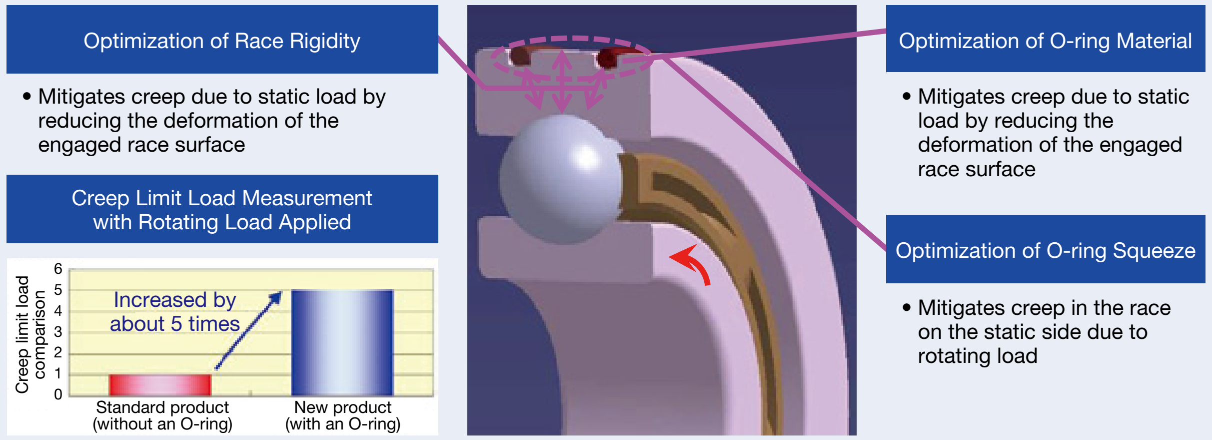

Fig. 29 Features of next-generation creep-free bearings

4. Afterword

This paper introduced the latest technologies for bearings for HEV and EV powertrains, for which efforts have been made to achieve more compact, efficient, electrified, and quieter products.

We will continue to develop new products with a thorough understanding of not just the environments of end users but also their needs, incorporating NSK's core technologies in areas such as tribology, materials, analysis, and mechatronics in order to improve HEV and EV environmental performance, fuel efficiency, and power performance.

References

1) IEA, ETP (Energy Technology Perspectives), 2012.
2) Motor Corporation, "Electronic technical manuals – PRIUS ZVW5#," (CD-ROM) No. SC3220J (2015).
3) H. Takemura and K. Kitamura, "Development of miniature needle bearing for planetary gears with high speed rotation," International Journal of Automotive Engineering, 42–4 (2011) 897–901.
4) S. Urakami, J. Liu, and Y. Matsumito, "Development of ultra-high-speed planetary needle roller bearings," NSK Technical Journal, 680 (2006) 36–41.
5) T. Maejima and T. Tanaka, "Development of ultra-high-speed ball bearing for motors in next-generation hybrid vehicles," NSK Technical Journal, 685 (2012) 2–7.
6) T. Ueda, T. Sakaguchi, N. Seno, S. Okita, and M. Mitamura, "Flaking form of under contaminated lubrication environment—Effect of tangential force on indentation origin flaking," NSK Technical Journal, 685 (2012) 58–60.
7) T. Ueda, N. Seno, and M. Mitamura, "Effect of the rolling element surface texture on indentation origin flaking life," NSK Technical Journal, 685 (2012) 55–57.
8) K. Yamamoto and H. Takemura, "Development of long-life planetary shaft (SHX3 Steel) for planetary gears of automotive transmissions," NSK Technical Journal, 686 (2013) 52–57.
9) T. Saito, H. Maejima, and T. Hiramoto, "Development of new-generation low-frictional-torque tapered roller bearings," NSK Technical Journal, 685 (2012) 8–13.
10) T. Ootsubo and S. Kadokawa, "Trends and new technologies of automatic transmission bearings," NSK Technical Journal, 677 (2004) 46–53.
11) J. Zhan, Y. Sakajiri, H. Takemura, and K. Yukawa, "Outer ring creep of a bearing," NSK Technical Journal, 680 (2006) 13–18.
12) J. Zhan, H. Takemura, and K. Yukawa, "A study on bearing creep mechanism with FEM simulation," 2007 ASME International Mechanical Engineering Congress and Exposition, IMECE2007-41366 (2007).

Takanori Ooshima

Satoshi Masuda

NSK EPS Control Technology

Satoshi Shimokawabe and Tetsuya Kitazume
Steering Technology Center

Abstract

In recent decades, in order to reduce energy consumption and protect the environment, electric power steering (EPS) systems are increasingly used as alternatives to hydraulic power steering systems. Additionally, expectations have grown for EPS as a technology that can help to reduce traffic accidents, as it has a high controllability.

In this paper, we look back on NSK's progressive approach to EPS development. We also discuss the new ACTIVE ON CENTERING control. One concept undergirding NSK EPS control is that EPS is a man-machine interface. This means that EPS is not only an actuator to reduce the steering effort of the driver; it should also be an interface to properly connect driver maneuvers and vehicle movement.

With this concept, NSK has developed the ACTIVE ON CENTERING control. For easy handling when a driver returns the steering wheel to the center position, the control makes assistant force, and the effectiveness of this new control has been confirmed through testing.

1. Introduction

As an environmentally friendly technology, electric power steering (EPS) systems are replacing the once mainstream hydraulic power steering systems. EPS systems use up to 95% less energy compared to their hydraulic counterparts, and they do not require hydraulic oil. In recent years, owing to their excellent controllability, these systems have attracted attention for their potential to evolve further for use as control actuators to support partially automated driving such as for parking or autonomous cruising toward reducing traffic accidents.

NSK has been focused on developing EPS by positioning it not merely as a power-assist unit to reduce the steering effort of the driver but also as a man-machine interface or adequate interactive information-exchange measure to convey the driver's intentions related to vehicle movement and the vehicle's running condition with precision.

In this paper, we will look back on NSK's progressive approach to EPS development and discuss the new ACTIVE ON CENTERING control based on the man-machine interface concept, developed to improve steering wheel returnability.

2. History of NSK EPS

Table 1 summarizes the history of NSK's mass-produced EPS and its evolution toward becoming highly functional.

NSK began developing EPS in the 1980s and subsequently became the world's first company to mass-produce the pinion-type EPS for minicars in 1989. In 1990, NSK started producing the column-type EPS for minicars. In 1995, mass-production was launched for the column-type ESP for the European sports car market, and NSK has since been gradually expanding its business into the area of compact cars and minicars. For more details about its development history and technologies, please see the referenced articles[1].

With heightened environment awareness and more efforts toward environmental preservation, EPS must meet requirements for both high power and high functionality so that many more types of cars can have EPS. Toward more compactness and higher power, NSK developed a column-type EPS with brushless motor[2], which reached 8 500 N rack force, which is loadable onto 2L class passenger cars, and NSK began mass producing this system in 2004.

Development efforts followed for more compact, more functional, and higher power EPS systems, which are being used in cutting-edge vehicles, including hybrid cars and electric vehicles.

Table 1 History of NSK EPS development

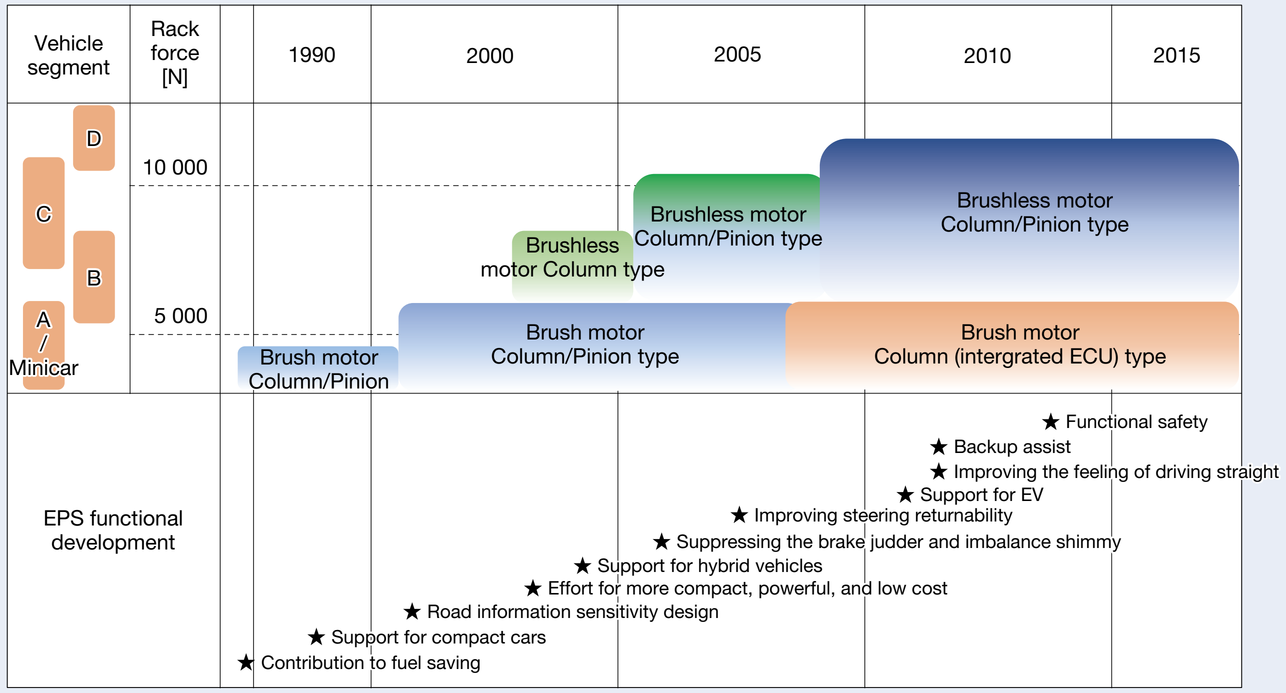

3. Evolution of the EPS Control Technology

EPS has advantages over hydraulic power steering systems in fuel saving and other features. On the other hand, it has disadvantages in steering maneuverability due to increased friction and inertia, mainly caused by the connection of the power-assist motor and reduction gear. For this reason, the first EPS was regarded poorly for its maneuverability.

As the number of vehicle types in which the system can be used increased, more requirements arose in relation to steering maneuverability. In such a situation, NSK developed EPS by positioning it as a man-machine interface. This is based on the concept that EPS should not only reduce the steering effort of the driver, but it should also function as an interface to accurately convey vehicle movement to the driver.

In Japan, there is an old saying that goes: “unity must exist between the rider and the horse.” In this regard, there must be a sense of unity between the rider’s intentions and the horse’s movements, which in turn makes riding more enjoyable. We believe the same thing is applicable to vehicle driving, and this sense of unity can also be applied to lessen driver fatigue and stress, also providing a sense of self-confidence and security, thus leading to safer driving conditions and fewer traffic accidents.

With this in mind, NSK developed a road information sensitivity design method, which it began to mass produce for European compact cars in 2002. The method was received favorably, as the steering provides a sense of unity. For a specific design method, please see the reference3).

Ever since, as per Table 1, NSK has expanded EPS applicable vehicle types through efforts in pursuit of higher power, and NSK has also been providing a secure and safe EPS, with comfortable steering maneuverability, that is based on the man-machine interface concept. It includes active vibration suppression control (Figure 1) to reduce uncomfortable vibration that spreads to the steering wheel due to brake judder or imbalance shimmy. Moreover, pulling compensation control (Figure 2) makes driving more comfortable by reducing operation force in order to maintain straight traveling.

Next we take a look at ACTIVE ON CENTERING control that is based on the aforementioned concept.

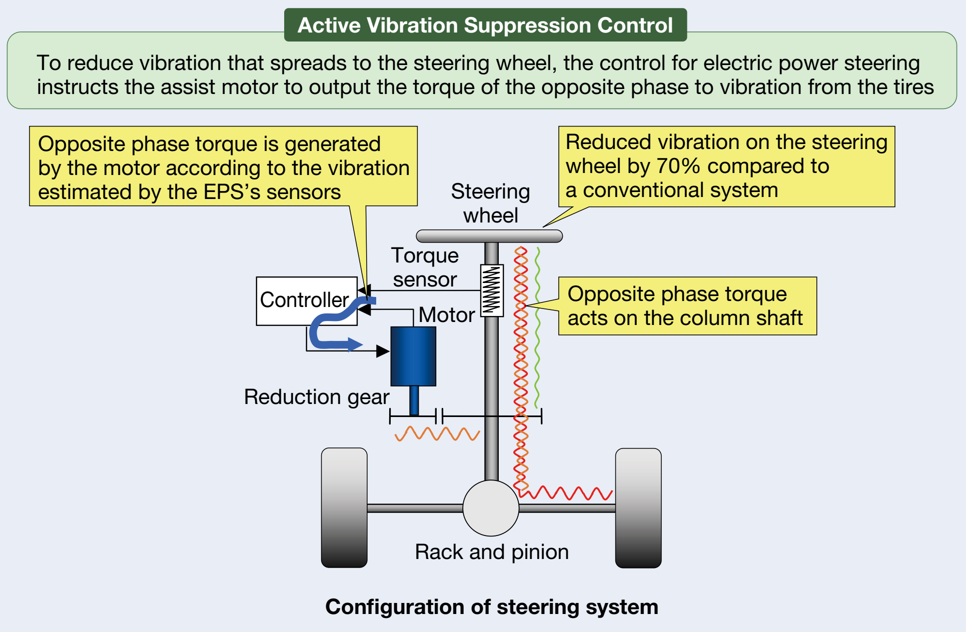

Fig. 1 Active vibration suppression control

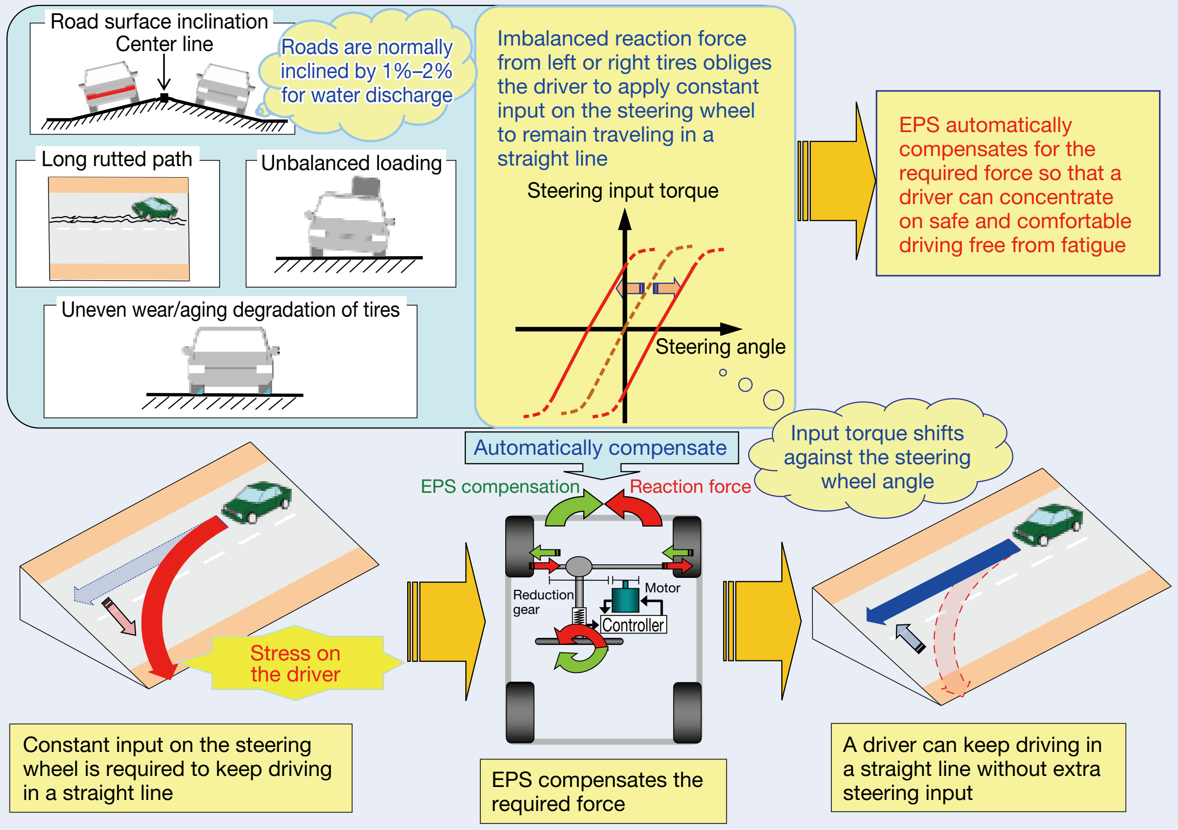

Fig. 2 Pulling compensation control

4. ACTIVE ON CENTERING Control

4.1 Background and aim of development

As previously discussed, a vehicle controlled based on the driver's intention makes driving more comfortable and enjoyable, leading to a sense of self-confidence and security and safety by lessening stress and fatigue.

However, when returning a steering wheel to a center position to go back to a straight traveling state after having steered right or left at an intersection or gone around a curve, there are cases where drivers will find it more difficult to control their vehicle as intended, as well as the driver's intention of vehicle movement compared to turning the wheel from a straight traveling state. This is because the direction of the vehicle and the orientation of the steering wheel are opposite. In addition, even when moving straight ahead, the driver is required to operate the steering wheel to the correct position every time they encounter bumps in the road, come against a crosswind, or need to even slightly adjust vehicle direction.

In such cases, if EPS creates a state where a steering wheel returns properly without requiring a driver's extra concentration to return the steering wheel to the proper position, the driver can continue to engage in safe, comfortable driving free from challenging steering control and the fatigue and stress that result from such repeated efforts to correct the steering. Moreover, the stability achieved by accurate steering wheel returnability and the elimination of unnecessary course correction allows for a more comfortable space for passengers as well.

Focused on that, NSK developed a new control to change EPS assistance so that the steering wheel returns appropriately.

4.2 Features and configuration of the new control

Most steering wheel returnability is determined by the magnitude relationship between the reaction force from the tires and the resistance force, such as the mechanical friction in the path from the tires to the steering wheel. In other words, when frictional resistance is greater than the reaction force from the tires, the steering wheel stops on its way back to the center position. This means that the driver has to return the wheel if they want to drive straight ahead.

NSK has so far been working on reducing friction and improving efficiency for the steering mechanism, and has thus developed a control to compensate the lack in steering wheel returnability. Figure 3 is a control block diagram of conventional active return control. This conventional control has a basic steering return assist configured at each steering angle, allowing weighting setting according to vehicle speed and steering wheel angular velocity, considering the vehicle properties.

On an actual vehicle, in addition to the steering mechanism, the steering wheel angular velocity is influenced by the suspension and other parts, and the reaction force from tires is subject to change depending on vehicle speed, steering angle, road conditions, tire conditions and other factors. Therefore, optimizing steering wheel returnability according to the properties of the vehicle depended on tuning of control parameters during vehicle testing. Another challenge was that the steering return velocity fluctuates up and down, especially when the reaction force from the tires changes up and down.

To address these challenges, NSK developed a new control with the aim of returning the wheel to the center position by taking a stable transition, regardless of the reaction force from the tires or the mechanism's friction magnitude.

Figure 4 is a control block diagram of the ACTIVE ON CENTERING control. In order to not only return the steering wheel to the center position but also to do this with stable transition; that is, smooth steering wheel angular velocity, the control structure is equipped with the active return control developed by NSK. Moreover, it is also equipped with feedback control, having a target steering velocity calculated according to the conditions of the vehicle and the driver's maneuver. By using the feedback control, control output can be adjusted to follow a target steering wheel angular velocity, thus making stable steering wheel return possible even though the reaction force from the tires changes due to varying road conditions.

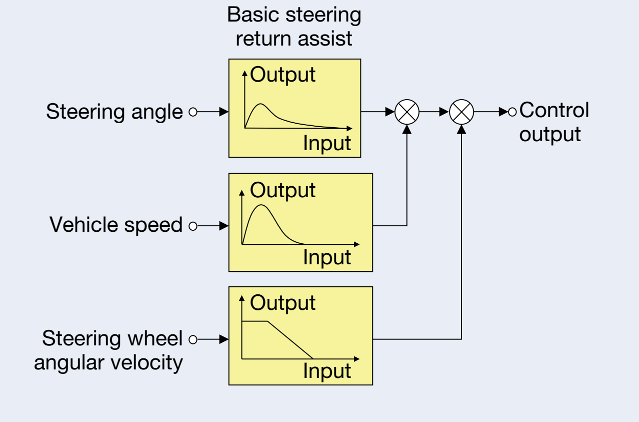

Fig. 3 Conventional active return control

A target steering wheel angular velocity in the ACTIVE ON CENTERING control can be calculated as follows.

So that the control is not dependent on the magnitude of friction, the motion equation of EPS, in which friction is eliminated, is defined in expression (1) below.

$$J\ddot{\theta}+D\dot{\theta}=SAT+T_{\mathrm{m}}+T_{\mathrm{h}} \tag{1}$$

Symbols used here are defined as follows: $\ddot{\theta}$: Steering wheel angular acceleration, $\dot{\theta}$: Steering wheel angular velocity, J: Inertia moment in the EPS system, D: Viscosity coefficient in the EPS system, SAT : Reaction force from tire (self-aligning torque), T_{m}: EPS assistant torque, T_{h}: Driver's torque. Performing a Laplace transform to expression (1) and adjusting the steering wheel angular velocity ($s\theta$) using the Laplacian operator (s) gives expression (2).

$$s\theta=\frac{1}{\frac{J}{D}s+1}\left(\frac{SAT}{D}+\frac{T_{\mathrm{m}}+T_{\mathrm{h}}}{D}\right) \tag{2}$$

Expression (2) reveals that $\frac{1}{\frac{J}{D}s+1}$ has a low pass filter property with $\frac{J}{D}$ as the time constant. Also, on the left side is a steering wheel angular velocity, but the right side presents angular velocity as well. That is, $\frac{SAT}{D}$ on the right side can be interpreted as a steering wheel angular velocity due to the reaction force from tires, and $\frac{T_{\mathrm{m}}+T_{\mathrm{h}}}{D}$ can also be interpreted as a steering wheel angular velocity due to the driver's torque and EPS assistant torque.

The steering wheel angular velocity due to the reaction force from tires $\frac{SAT}{D}$ has only to be set based on the steering wheel angle and vehicle speed in accordance with the desired vehicle properties. As EPS assistant torque (T_{m}) can be estimated from EPS motor current, and the driver's torque (T_{h}) is detected by the EPS torque sensor, a steering angular velocity due to the driver's torque and EPS assistant torque can be calculated by setting the viscosity coefficient D so as to obtain the desired steering characteristics.

Therefore, by configuring the feedback control using the steering wheel angular velocity calculated from expression (2) as the target value, a steering wheel angular velocity can be obtained according to the conditions of the vehicle and the driver's maneuver.

4.3 Evaluation method

To verify the effects of the new ACTIVE ON CENTERING control, NSK evaluated vehicles with the following three viewpoints.

Evaluation 1: Transition of the steering angle and angular velocity after the steering wheel is released

The driver steers to a certain angle while the vehicle is running. After that the steering wheel is released. Steering wheel returnability is evaluated regarding residual steering angle (remaining angle to the center) and transition of the steering wheel angular velocity.

Evaluation 2: Relationship between the driver's torque and steering angle

Evaluation of steering characteristics by plotting steering wheel angle on a horizontal axis and the driver's torque on a vertical axis.

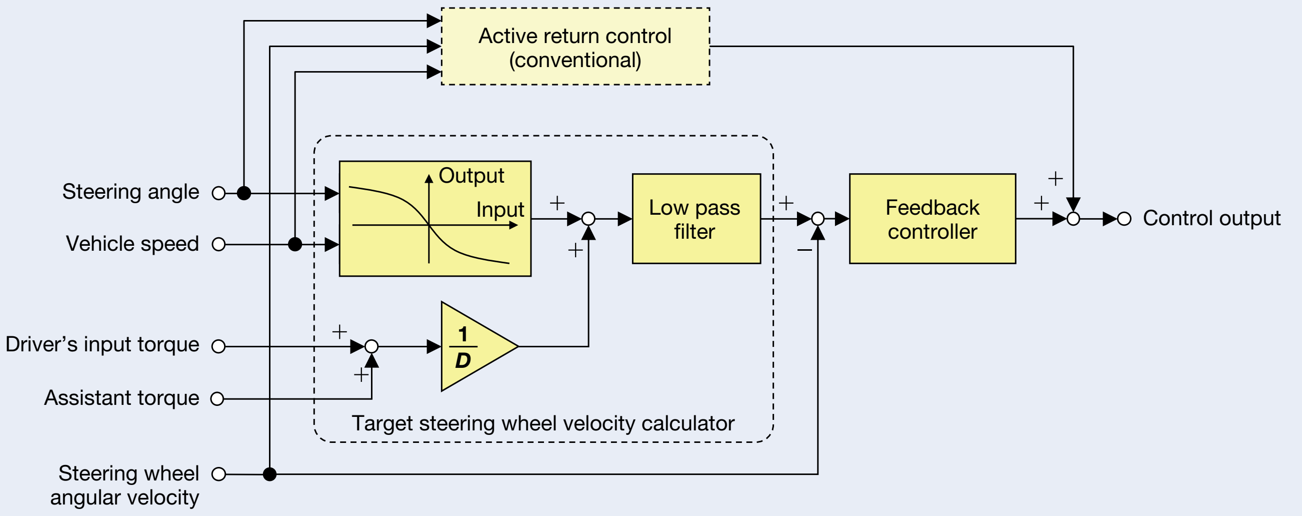

Fig. 4 ACTIVE ON CENTERING control

Evaluation 3: Relationship between the driver's torque and vehicle behavior

Evaluation of steering characteristics by plotting the driver's torque on a horizontal axis and the yaw rate of the vehicle turning on a vertical axis.

Evaluation 1 is generally used to evaluate vehicle steering wheel returnability, which indicates that the smaller the residual steering wheel angle, the less a driver has to turn the steering wheel to return the car to a straight direction. Furthermore, the smoother the change of steering wheel angular velocity, the milder the vehicle behavior or motion.

Evaluation 2 is generally used to plot steering characteristics on a figure in order to present the relationship between the steering angle when a driver turns and the driver's torque which is required while the driver turns the steering wheel.

When considering EPS as a man-machine interface, ease in handling the vehicle and predicting its behavior can be a benchmark. Here, excellent steering performance is defined, whereby the driver's torque is modestly light and the relationship between the steering angle and the driver's torque is linear. This is based on the insight that when the relationship is linear, the driver's torque to turn the wheel does not change abruptly. That is, the driver can turn the wheel smoothly with little unevenness in the steering operation.

Evaluation 3 is a method for plotting steering performance on a figure to present the relationship between the driver's torque and vehicle turn behavior (yaw rate). An excellent steering performance is defined that the vehicle turns in response to the driver's torque and that the relationship is linear. It is based on the insight that when the relationship is linear, vehicle behavior responding to the driver's torque change does not change abruptly; thus the driver can turn the wheel without waste by predicting the change in vehicle behavior easily based on the change in the driver's torque. Moreover, it is based on the insight that the driver is able to perceive vehicle behavior not only from the driver senses of vision and balance but also from the driver's torque.

4.4. Test results

Figures 5 and 6 show the results of Evaluation 1, providing the temporal transition of the steering angle and steering wheel velocity after the steering wheel is released from the positon where it is kept at a fixed angle. The section within the surrounding broken line in Figure 5 corresponds to the time domain for the residual steering angle, which shows that the residual angle is reduced by the ACTIVE ON CENTERING control. Figure 6 also indicates that steering wheel velocity is smooth.

Figure 7 shows the result of Evaluation 2 and the relationship between the steering angle and the driver's torque when the driver turns the wheel right and left up to a certain angle. The steer forward sections in Figure 7 form relatively straight lines with little difference with or without the ACTIVE ON CENTERING control. This means that the ACTIVE ON CENTERING control does not encumber the steering operations of the driver. However, the steer back sections within the surrounding broken lines show that the driver's torque is lessened by the ACTIVE ON CENTERING control and that the relationship between the steering angle and the driver's torque approximates to lines, indicating the driver can feel smoother operation.

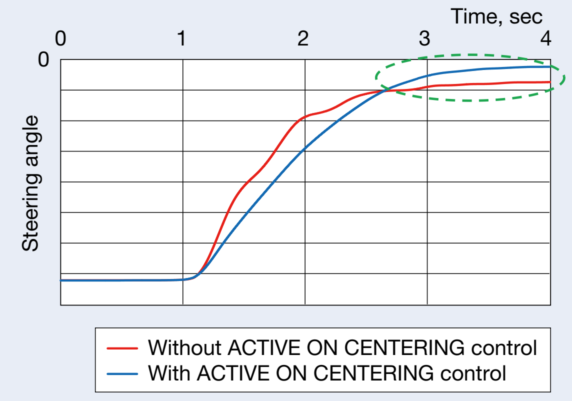

Fig. 5 Vehicle test results: residual steering angle when the steering wheel is released

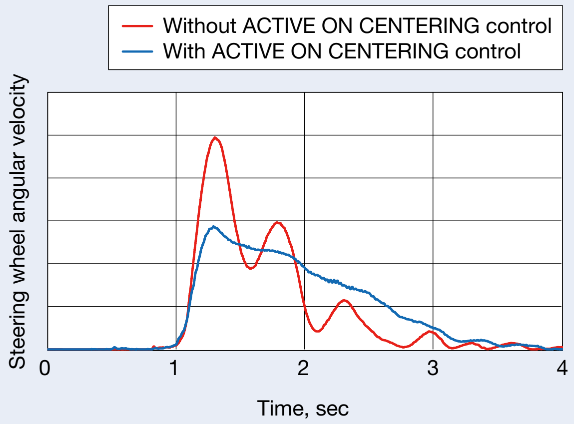

Fig. 6 Vehicle test results: steering wheel angular velocity when the steering wheel is released

Figure 8 shows the result of Evaluation 3 and the relationship between the driver's torque and the vehicle yaw rate when the driver turns the wheel right and left up to a certain angle. As shown by the surrounding broken lines, the relationship between the driver's torque and yaw rate during wheel reversing approximates to the lines, indicating that the driver can easily predict vehicle behavior through the driver's torque.

From these results, NSK has confirmed that steering performance and comfort have improved, owing to the ACTIVE ON CENTERING control with feedback control using the target steering wheel velocity based on expression (2).

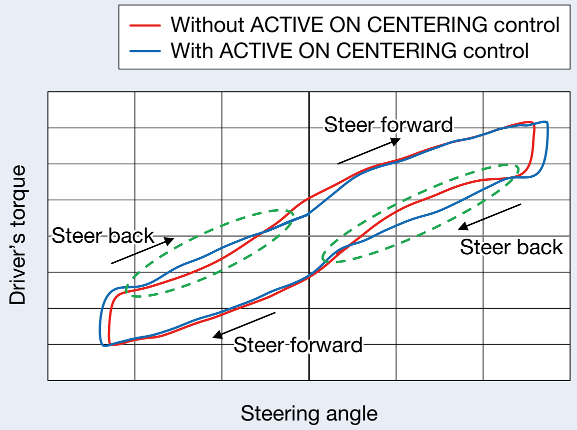

Fig. 7 Vehicle test results: relationship between the steering angle and the driver's torque

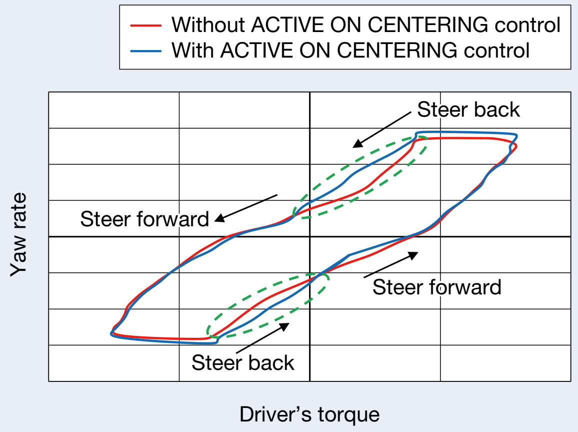

Fig. 8 Vehicle test results: relationship between the driver's torque and the yaw rate

5. Afterword

This paper looks at the history of NSK EPS and introduces NSK EPS control technologies with a particular focus on the ACTIVE ON CENTERING control. The ACTIVE ON CENTERING control's contribution to improving vehicle controllability and comfort is also discussed while presenting the results of vehicle testing.

By continuously positioning EPS as a man-machine interface, NSK is committed to developing technologies while contributing to the evolution of vehicle safety, protection of the environment, and comfort.

References

1) Y. Kouzaki, G. Hirose, S. Sekiya, and Y. Miyaura, "Electric power steering (EPS)," NSK Technical Journal, 667 (1999) 14–22.

2) T. Sakaguchi and S. Endo, "Development of a high-output brushless DC motor for EPS," NSK Technical Journal, 682 (2007) 33–41.

3) S. Endo and H. Kobayashi, "EPS control technology," NSK Technical Journal, 676 (2003) 55–60.

Satoshi Shimokawabe

Tetsuya Kitazume

Development of High-Speed, High-Power Spindles With Automatic Grease Replenishment

Shoichiro Oguri, Yoshifumi Inagaki and Osamu Iwasaki
Industrial Machinery Bearing Technology Center

Abstract

In recent years, significant developments in the aircraft and automotive industries have led to increased demand for high-speed machine tool spindles to increase production efficiency. For this reason, NSK has developed high-speed, high-power spindle units in addition to the NSK standard spindle series. These spindle units use a constant-pressure preload and a rear bearing sleeve with a spiral-groove cooling structure to sustain rotational accuracy. Other features include a grease-replenishing unit to prolong spindle life, a quadruple-seal structure to prevent infiltration of coolant, and a tool-unclamping cylinder.

1. Introduction

To meet increased demand for high-speed machine tool spindles toward increasing production efficiency, ultra-high-speed spindles, such as the 4-million d_mn class, have been developed[1]. An oil lubrication method had conventionally been used for these spindles; however, in light of the increasing number of environmental measures being introduced, as well as the drive to save energy and resources, there is a need to address environmental concerns, such as by reducing the scattering of oil mist, noise, and mass air consumption. To meet these requirements, and to address efforts to contribute to higher production efficiency, NSK has developed and started selling an epoch-making standard, high-speed (wide-range machining) types of grease replenishment built-in motor spindles to reduce environmental impact and increase functionality[2].

Moreover, in recent years there have been significant developments in the aircraft and automotive industries that have led to greater demand for high-speed/high-power component processing machine tool spindles for increased production efficiency.

NSK has therefore developed high-speed/high-power grease replenishment spindles in addition to the NSK standard spindle series.

2. Overview

The new high-speed/high-power type spindles in NSK's product lineup represent NSK's advanced technologies and have been developed based on the standard/high-speed type that has good sales performance. The new spindles (HSK-A63 type), with further improved specifications and a new technology added to the aforementioned existing type achieved the world's highest speed of grease replenishment.

2.1 High-speed/high-power spindle specifications

Table 1 provides the spindle specifications and Figures 1 and 2 show its appearance and dimensions, respectively.

3. High-speed Technology

3.1 Constant-pressure preload method

The conventional standard/high-speed type applies a position preload method combining a front-bearing inner diameter of ϕ70 mm, angular ball bearing DBB, a rear-bearing inner diameter of ϕ55 mm, and angular ball bearing DB. This new spindle has the same inner bearing diameter as in the standard/high-speed type, combining the dual-row front bearing DT and dual-row rear bearing DT, and a constant-pressure preload method is used to apply the preload with a coiled spring. The inner and outer bearing rings are made of SHX material, NSK's special bearing material developed to endure under high-speed rotation conditions (Table 1).

Table 1 Spindle specifications

Installed Position		Horizontal/Vertical
Max. rotation		25 000 rpm
Bearing	Front	ϕ70BNR10 series (SHX)
	Rear	ϕ55BNR10 series (SHX)
Tool holder		HSK-A63
Lubrication		Grease replenishment
Preload method		Spring preload
Coolant function		Through coolant (7MPa)
Output		22/25/30 kW
		(cont./30 min/15%)
Max. torque		80 Nm
		(15%)

Fig. 1 High-speed, high-power spindle with automatic grease replenishment

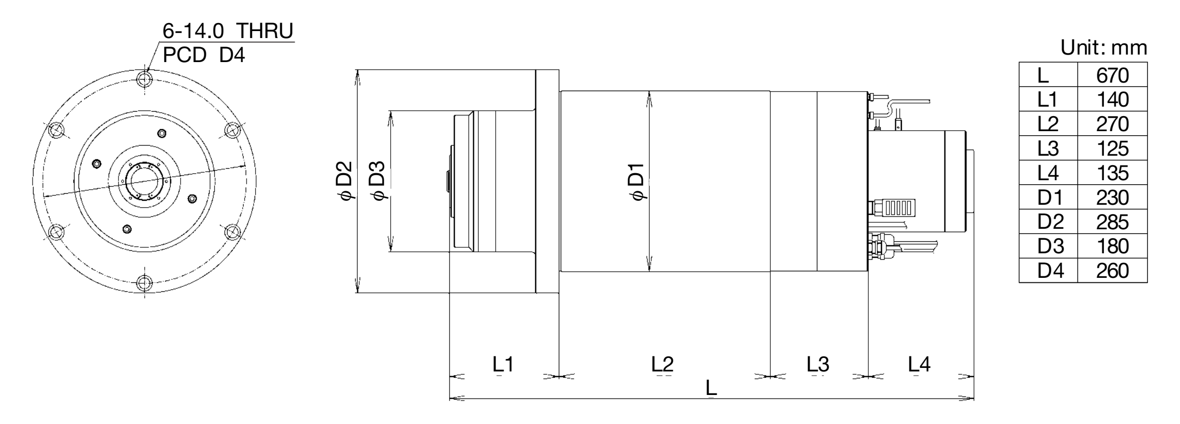

L	670
L1	140
L2	270
L3	125
L4	135
D1	230
D2	285
D3	180
D4	260

Fig. 2 Boundary dimensions

The rear bearing housing has a bearing sleeve that can slide in the axial direction. The sliding structure allows a given pressure to be applied, and the relative heat expansion of the shaft in the housing is to be absorbed backward during operation (Figure 3).

A constant-pressure preload structure, however, raises the following concerns.

- In the so-called upright position, with the cutter on the downside when the machining tool is inserted, the spindle rigidity decreases because the front bearing (fixed side) preload is reduced due to the spindle's shaft weight. As a result, increased vibration can have an impact on machining accuracy (Figure 3).

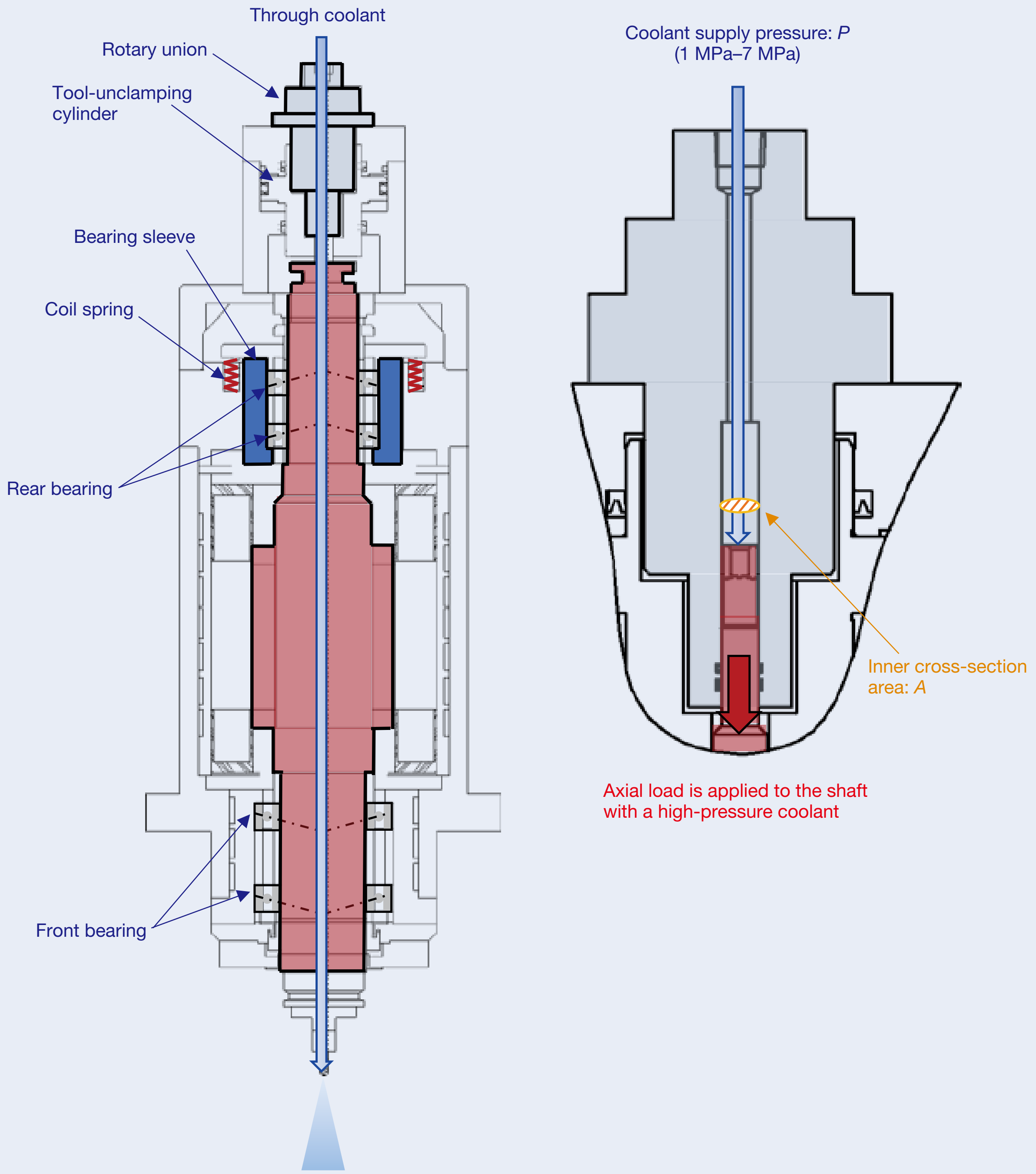

Fig. 3 Structure of the high-speed, high-power spindle

- The new spindle has a through-coolant function. This function is a feature for supplying up to 7.0 MPa of high-pressure coolant to a rotary union, which passes a clamping unit inside the shaft and discharges it from the cutter end. When the high-pressure coolant passes the rotary union, a generated axial load (coolant supply pressure: $P \times A$ [rotary union inner diameter cross-section area]) is applied in the axial direction when passing the clamping unit. It reduces the front bearing preload (fixed side), thus increasing the vibration affects machining accuracy (Figure 3).

Figure 4 shows the two above-mentioned effects on preload change. This indicates that the preload does not change in various conditions, for the rear bearing, but that it reduces the dependence on conditions, as with the front bearing.

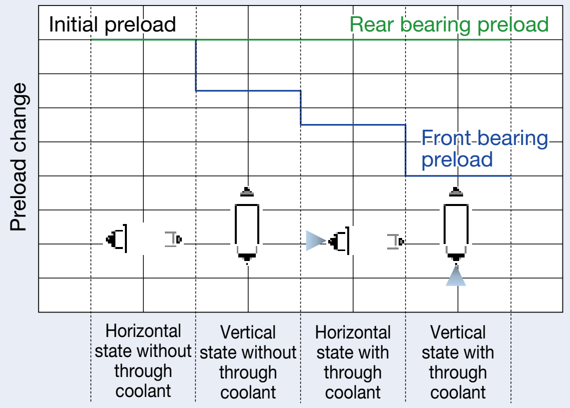

Fig. 4 Preload change due to positioning and through coolant

Those concerns must be prevented because spindles are used in different positions, and through-coolant exerts effect in deep hole drilling and other machining processes. To that end, preload must be considered in regard to the axial load generated by the shaft weight and through-coolant. When preload loading is excessive, the load applied onto the bearing is greater and causes premature heat seizure under conditions in which the preload has not been reduced. Therefore, regarding the balance between vibration and bearing preload, various verification tests were conducted to set the optimal preload for the new spindles.

Figure 5 shows a comparison of the spindle vibration before and after the axial load was taken into account. The vibration value standard was set at 1 μm or less. Under the condition in which axial load was not considered, the vibration value exceeded 1 μm at 20 000 rpm, at a horizontal state with through-coolant. Assuming that an operation is carried out in upright position with through-coolant, preload will reduce further, and vibration is expected to increase. In fact, however, by setting an optimal preload with the axial load taken into account, throughout the entire rotation range, the vibration value was 1 μm or less even in upright position with through-coolant.

Figure 6 shows a comparison of respective temperature rises in front bearing. When preload was set with the axial load taken in to account, temperature rise was approximately 3°C higher at 25 000 rpm. Although increased temperature raises a concern about an adverse impact on grease life, it has been confirmed with the endurance test result of continuous operation that service life is not affected when an appropriate grease replenishment interval is considered. Also, difference in temperature rise can be controlled by changing the condition of housing cooling.

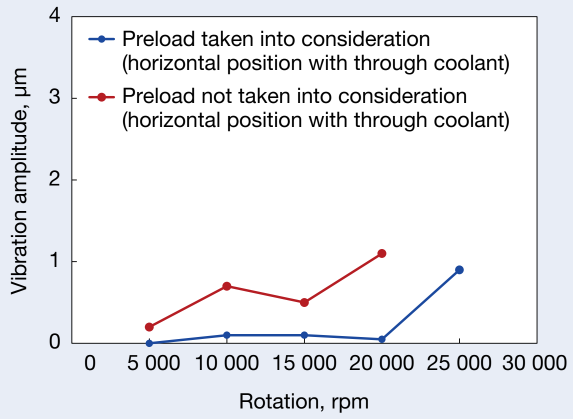

Fig. 5 Comparison of vibration with and without preload

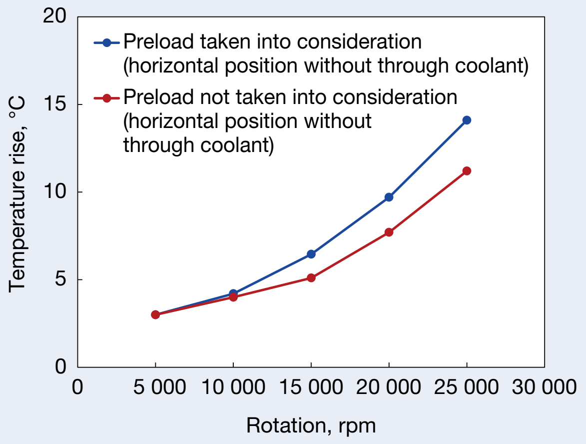

Fig. 6 Comparison of temperature rise with and without preload

3.2 Sleeve-cooling structure

As previously mentioned, the spindles have a structure equipped with a sleeve that can slide the rear bearing part in the axial direction. In most applications, the free-moving rear bearings are smaller in size than the front bearings by one or two ranks. This decreases the bearing $d_\mathrm{m}n$ value, which suppresses the temperature rise, and therefore a cooling mechanism is not added in most cases so as to avoid a complicated structure, considering the impact that the rear-side thermal deformation of the main shaft has on machining accuracy is smaller when compared to the front side.

Among the current high-speed main shafts, many types exceed the maximum rotation of 20 000 rpm in tool taper #40. For example, a rear bearing $d_\mathrm{m}n$ value could exceed 1 or even 1.5 million. Also, types that even exceed a $d_\mathrm{m}n$ value of 2 million are increasing in number, often requiring an efficient cooling mechanism for the rear bearings.

Specifically, in cases where heat generation is greater in the rear bearing of the high-speed shaft, the following problems are possible.

- Bearing inner temperature rises and lubrication oil viscosity decreases. Heat seizure occurs at the rolling contact areas due to insufficient oil film formation.
- Sliding failure occurs due to narrowed clearance in the sliding part (between the sleeve outer diameter and housing inner diameter) caused by the heat expansion difference between the sleeve near a heat source (i.e., rear bearing) and the housing, which has greater heat capacity and is located away from heat source. Thus, a hampered free-moving function produces thermal expansion between the fixed bearing side (front bearing) and the free-moving bearing side (rear bearing), resulting in a tensile load. The load may cause damage to the bearing if it is applied excessively. Or, on the contrary, the released preload may generate an abnormal level of noise and vibration.

The structure of the spindles allows for the cooling sleeve on the outer diameter surface of the sliding part to suppress heat generation in the rear bearing (Figure 7), resulting in the following advantages.

- The provision of the direct cooling mechanism on the sliding part can efficiently cool the free-moving rear bearing, owing to the direct cooling of the bearing sleeve. Therefore, the decreased bearing inner temperature retards the lubricating film deficiency caused by the decreased oil viscosity at the rolling contact areas or cage guide face.
- The cooling of both the housing and sleeve materials makes them shrink uniformly in the radial direction. This prevents slide failure from clogging due to narrow clearance.
- Smoothened oil flow by means of a spiral-groove cooling structure facilitates the uniform cooling of the entire sleeve, thereby preventing cooling-induced distortion. This also prevents the internally engaged bearing from becoming distorted, and so the rotational accuracy of the main shaft does not deteriorate.
- Installing an elastic body near both axial ends of the sliding part can prevent cooling oil leakage. For the body, using a rubber material, such as an O-ring, or a resin material can enhance the damper effect of the pressurized cooling oil and the attenuation property in a high-speed shaft.

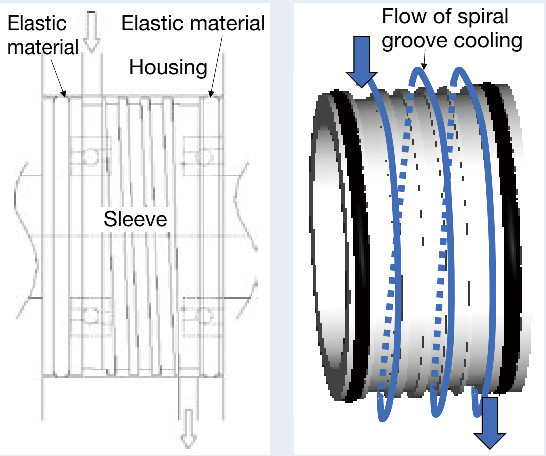

Fig. 7 Spiral groove cooling structure on bearing sleeve

- Even if there is early fretting, abrasive metallic particles are produced from vibration due to high-pitched waviness between the sliding part materials, and the cooling oil removes this fine wear powder. Therefore, no further fretting takes place due to the wear powder acting as an auxiliary agent. (In a conventional sliding structure without a cooling mechanism, deposited wear powder facilitates fretting.) As a result, service life is extended as a main shaft and machining performance improves.

3.3 Grease replenishing lubrication

A grease replenishing lubrication method is used for the spindles that has also been used for conventional standard/high-speed types, and there is a grease replenishment unit attached (Figure 8).

The grease replenishing lubrication is a lubrication method through which a small amount of grease is discharged by a metering piston of the grease replenishment unit, which is carried by outlet pressure through a tube and intermittently supplied to the bearing.

A note of caution in grease replenishment: a high-speed operating bearing replenished with a mass of grease generates heat abnormally because of the increased agitation resistance of grease. Moreover, the service life of grease is reduced due to increased rotational speed and temperature. In the new spindles, as the $d_\mathrm{m}n$ value exceeds the operational record values of conventional standard/high-speed types, the optimal replenishment amount and interval were determined through experiments. Consequently, the replenishment interval for the standard/high-speed types was set at 6 hours per shot, and, for the spindles, at 4 hours per shot.

The faster the rotational speed, the more lubricant is needed, so the discharge interval is not constant but variable, responding to the sensed speed in order to support cases where the number of uses varies depending on machining conditions and to minimize the replenishment of the grease amount (Table 2).

In addition, grease replenishment lubrication needs to discharge grease smoothly as with oil air lubrication. To this end, by means of a discharge spacer, as in the standard/high-speed types, and a deposit groove in the housing, the grease is prevented from depositing inside the bearing.

Fig. 8 Grease replenishment unit (Fine Lube II)

Table 2 Replenishment intervals at various rotational speeds

Rotational speed (rpm)	To 12 009 or slower	12 010 to 14 009 or slower	14 010 to 16 509 or slower	16 510 to 20 009 or slower	20 010 to 25 009 or slower
Replenishment interval/1 shot	28.75 days	5.75 days	27.6 hrs.	6 hrs.	4 hrs.

3.4 Built-in high-power motor

The shortened spindle acceleration time will significantly enhance production efficiency. The new spindles have a built-in high-power motor with a maximum output of 30 kW (intermittent rating of 15%). The motor shortened the acceleration time by 41% at 20 000 rpm when compared with the standard/high-speed types. Incidentally, the acceleration time at 25 000 rpm was 2.8 seconds (Figure 9).

4. Spindle Auxiliary Functions

4.1 Seal structure

Machine tool spindles are used under conditions that are constantly exposed to coolant, and high-speed rotating spindles cannot use contact seals. As a result, coolant flows in a spindle, occasionally resulting in heat seizure. In grease lubrication, in particular, the seal effect is not so good as in oil air lubrication that uses air supply. To solve this problem, the spindles have a quadruple-seal structure that is the same as that used in the standard/high-speed types.

Figure 10 shows the quadruple-seal structure. The first stage is a slinger that has an effect to shake off coolant or chips by rotational centrifugal force so that most of the coolant can be prevented. The second stage is an air seal structure, which prevents coolant infiltration by blowing air from the outer perimeter of the slinger. At the third stage, a labyrinth structure was added, which can be used in cases where a contact seal is unusable due to high-speed rotation. An extended distance from the labyrinth mouth to the bearing prevents coolant from entering the bearing. The fourth stage is a seal spacer, where a rubber seal, intended for use as sealing bearings, is plugged into the bearing system. This compact non-contact seal, requiring no wide space in the axial direction, can shorten axial length.

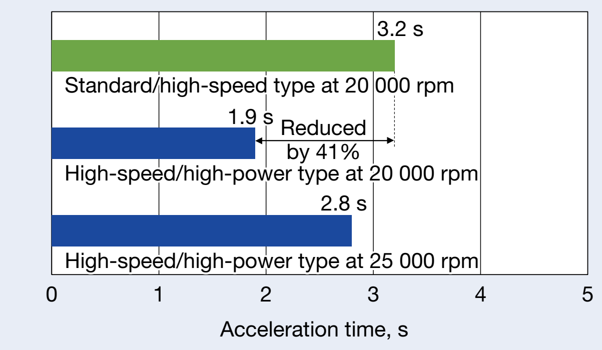

Fig. 9 Acceleration time

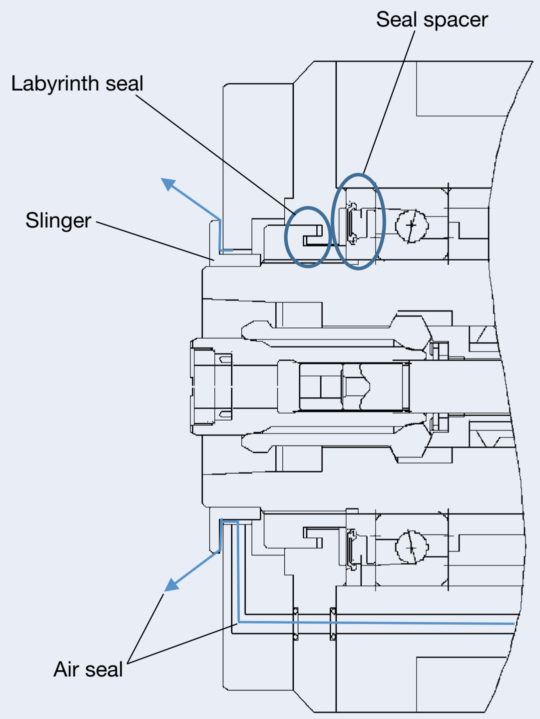

Fig. 10 Quadruple-seal structure

4.2 Tool-unclamping cylinder

The new spindle are equipped with a tool-unclamping cylinder in addition to a tool-clamping mechanism. This simplifies the equipment structure by eliminating the need for a piston cylinder. The hydraulically operated tool-unclamping cylinder is capable of unclamping with the aid of an air hydraulic booster to meet an oil-less requirement.

Furthermore, the unclamping cylinder is outfitted with proximity switches to check four control patters: clamp, unclamp, without tool, and misclamping. Even if a tool holder fails to clamp, or an operation is attempted without a clamp, such a state can be detected by the control (Figures 3 and 11).

5. Afterword

NSK has developed spindles to address market demand, and they have been highly evaluated by those who have used them. The new high-speed/high-power spindles are some of the world's top products, and they contribute to improving production efficiency as well as to mitigating environmental impact, equipped with a grease replenishing lubrication that can further extend service life.

While sharpening our abilities, we will continue to develop new spindles in order to meet market demand.

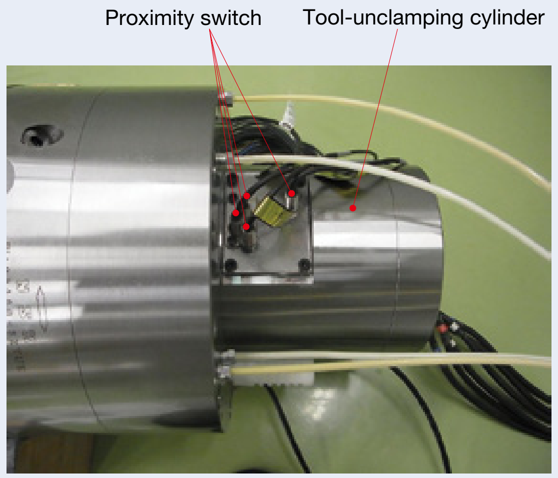

Fig. 11 Tool-unclamping cylinder and proximity switch

References

1) S. Sugita, "Ultra high-speed spindle for machine tools," NSK Technical Journal, 676 (2003) 11–15.
2) M. Aoki and Y. Morita, "Development of a motor spindle for machine tools using grease replenishment lubrication," NSK Technical Journal, 676 (2003) 16–25.

Shoichiro Oguri

Yoshifumi Inagaki

Osamu Iwasaki

Development of a High-Precision Vertical-Axis Table

Toshinori Sato
Linear Technology Center

Abstract

Recent technological progress has led to the creation of three-dimensional semiconductor devices. This development requires manufacturing apparatus and inspection equipment, such as positioning tables, to meet very strict precision demands. NSK previously developed an ultra-precise positioning table for two-dimensional semiconductor devices and is currently developing a three-dimensional precision positioning table to meet these new requirements. In this paper, this new high-precision vertical-axis table is discussed.

1. Introduction

Driving the development of a number of different types of industrial machines used for mass production is the demand for higher performance. Moreover, priority has been placed on advancing this development toward larger capacity, more compactness, lighter weight, greater accuracy, and higher speeds.

Recent technological progress has led to the creation of high-performance, large-capacity three-dimensional semiconductor devices, requiring ever more stringent accuracy in their manufacturing.

On the surface of semiconductor wafers, fine patterns have been formed two-dimensionally; however, a three-dimensional approach has been increasingly used in recent years with the vertical application of lamination layers, which requires a workpiece to be precisely positioned in every three-dimensional direction.

NSK has been developing a table for which precision positioning is also available in a vertical direction by combining a previously developed ultra-precise positioning table and an externally pressurized air bearing.

This paper examines this new high-precision vertical-axis table.

2. Challenges with High Precision

A number of challenges, such as technical problems related to machine components and high costs, have restricted efforts aimed at increasing precision. In addition, various efforts have been made to increase the motion accuracy of moving bodies—for instance, by reducing rolling element passage vibration in the rolling guide, and increasing precision in the machining of guide rails as well as in assembly precision.

Toward even greater precision, NSK has been focused on developing an ultra-precise positioning table with a non-contact two-dimensional (planar) guide equipped with an air bearing. However, to expand its related knowledge to the area of three-dimensional applications involving the vertical direction, an ultra-precise positioning table must be used to solve the following challenges.

- Reducing the adverse effects of tare weight support (precision change due to heat generation)
- Making it compact (low gravity center) to maintain or even reduce the current size
- Lower the cost

3. Structure and Features of the High-precision Vertical-axis Table

Photo 1 shows the new high-precision vertical-axis table, which has the following structure and features.

3.1 Conventional structure

Figure 1 shows the structure of a conventional vertical-axis table. This common structure includes a straight guide bearing placed vertically, which is driven via a central ball screw. The overall height is suppressed by replicating a drive timing belt around a motor. However, because the insufficient belt rigidity and the gap between engaging gears produce a positioning difference in ascent (first leg) and descent (second leg) motions. This structure is prone to the so-called lost-motion.

As for motion straightness, the structure can also provide at best a similar precision to that for the horizontal direction of conventional products.

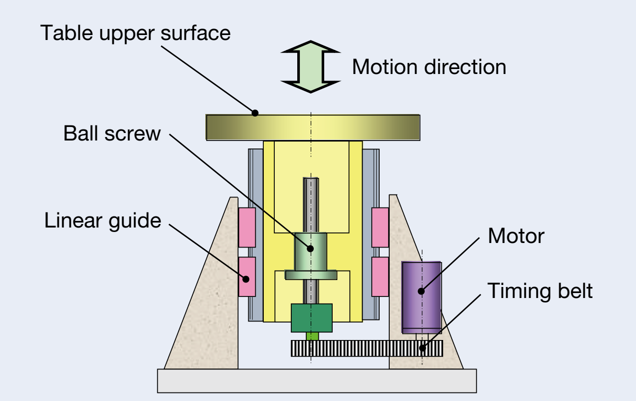

Fig. 1 Structure of a conventional vertical-axis table

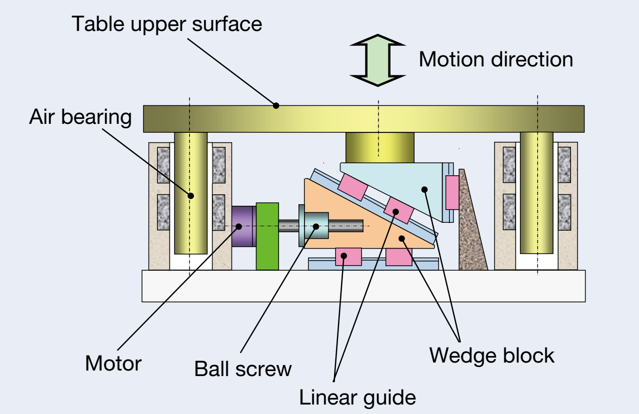

Fig. 2 Structure of the new vertical-axis table

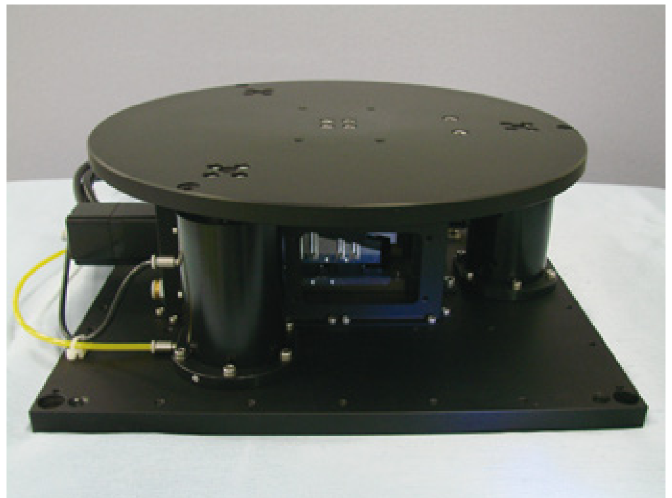

Photo 1 High-precision vertical-axis table

3.2 New structure

Figure 2 shows the structure of the new vertical-axis table. A wedge mechanism with two types of inclined blocks have been incorporated into the drive part, where lateral motion is converted vertically by means of the rolling guides attached in the inclined section. The inclination angle has a retarding effect, enabling smoother motion, with little lost-motion, while also maintaining high rigidity structure.

Three air bearings are positioned around the lifting table to guide the table vertically, and its well-balanced structure facilitates transmission of the drive force of the centrally located wedge mechanism to the gravity position vertically. This enables precise positioning through the ideal straight motion in the vertical direction.

3.3 Vertically guiding bearing

Figure 3 shows the structure of the new air bearing. As shown in Figure 4, the externally pressurized air bearing supports the shaft without contact, and it gains loading capability and rigidity by supplying compressed air from an external air source to the small clearance of a bearing through the air-feed aperture on the bearing. Externally pressurized air bearings are classified according to their air-feed aperture type.

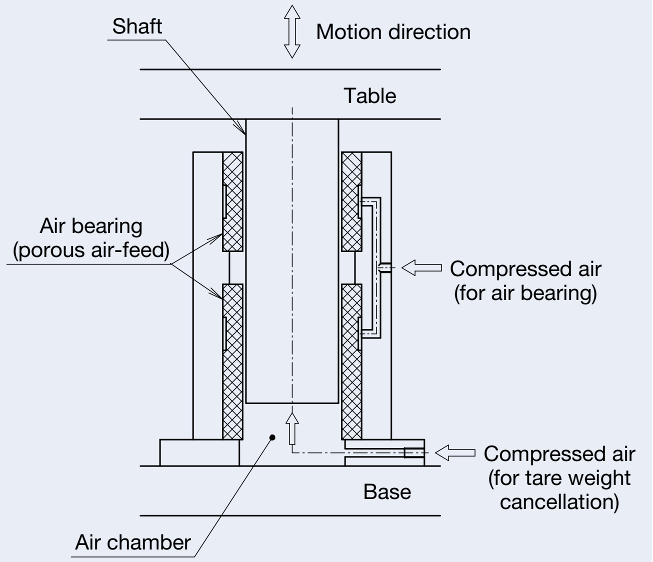

Fig. 3 Structure of the new air bearing

Figure 5 shows different apertures and Figure 6 shows a comparison of loading capability. NSK uses an efficient porous air-feed bearing that has a high loading capacity per unit area.

If for any reason air is not fed or is fed too much, the shaft and bearing make contact, which could result in heat seizure. To prevent this, NSK has used a porous graphite material with excellent lubricity as a solid lubricant.
Its configuration makes for a highly reliable pneumatic bearing, and yet it is compact and light.

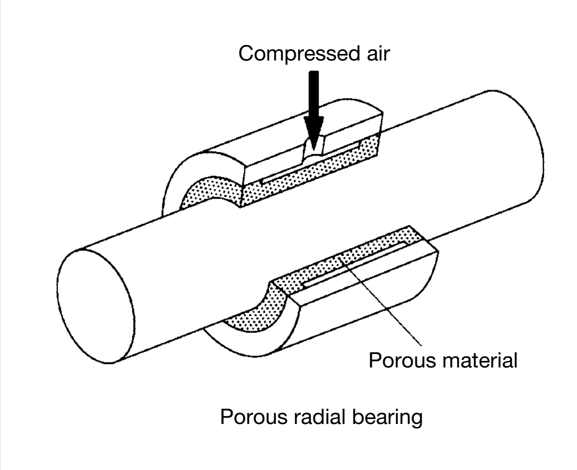

Fig. 4 Structure of the externally pressurized air bearing

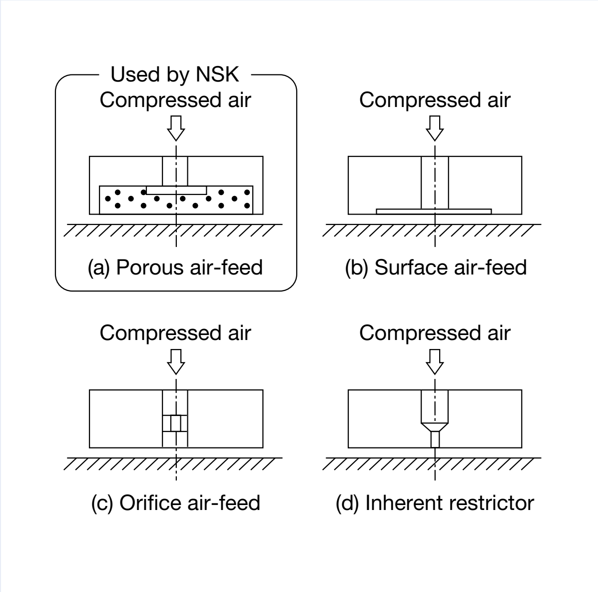

Fig. 5 Air-feed methods

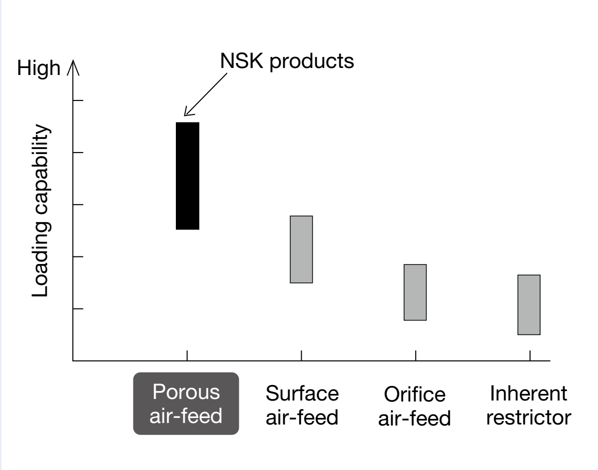

Fig. 6 Comparison of air-feed method performance

3.4 Tare weight cancellation mechanism

A tare weight cancellation mechanism is shown at the bottom of Figure 3. Air bearings have an air chamber at the bottom to accumulate compressed air supplied from outside. The tare weight of a moving body can be structured in a way that allows for cancellation by keeping this internal pressure constant to the level of movable mass. The spatial volume of a cylinder room changes when the movable shaft goes up or down, but the internal pressure can remain constant by means of a precision regulator installed outside.

This can cancel gravitational by tare weight constantly, reducing the load from a feeding mechanism, such as the ball screw or drive motor, and thus the entire structure can become more compact. It can also suppress heat generation, minimizing precision deterioration caused by thermal expansion, which enables higher repeatability even during long hours of operation.

4. Performance of High-precision Vertical-axis Table

The performance of the prototype high-precision vertical-axis table, developed using the afore-mentioned specifications, is described in this section.

4.1 Positional accuracy

Figures 7 and 8 show the pitching and yawing accuracies, respectively, results obtained by converting the attitude change of the table's upper surface into an angle using a laser end-measuring machine at an effective stroke of 3 mm.

In both the pitching and yawing attitudes, the measured values fall far below 1, indicating a good result with little fluctuation.

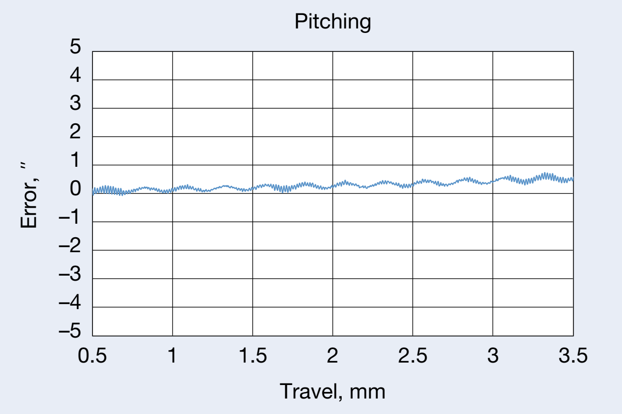

Fig. 7 Pitching

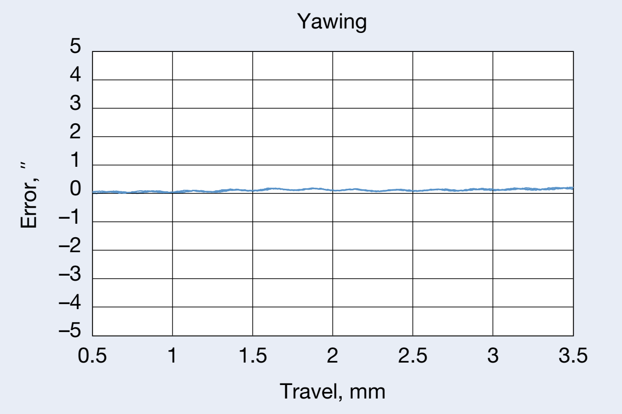

Fig. 8 Yawing

4.2 Straightness repeatability

Figure 9 shows the measurement results of straightness, obtained by three measurements with a laser end-measuring machine as in the attitude accuracy measurement above. The strong inclination of the wave form presents a parallel component due to the installation condition of the mirror reflector during measurement. The variation relative to this ideal straight inclination line corresponds to straightness. The wave form, showing three overlaid measurements, was confirmed to follow the same track across the entire stroke range.

As shown in Figure 10, an enlarged stroke center portion, a slight difference is found among the three measurements. Although the results may have involved various errors caused during the measurements, the repeatability was found to follow a motion trajectory of ±0.1 µm.

A significant improvement has been achieved, considering the conventional method that brought an unstable repeatability at around ±0.2 to 0.5 µm.

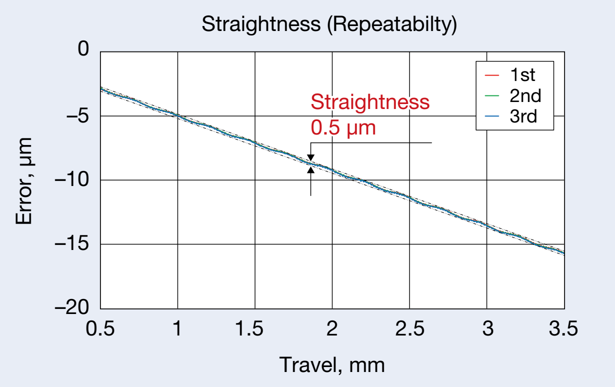

Fig. 9 Straightness

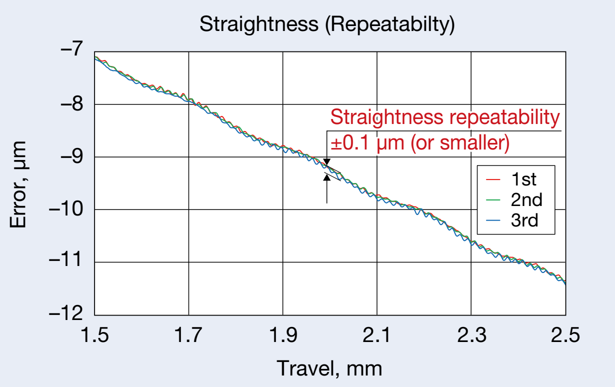

Fig. 10 Straightness repeatability

5. Afterword

The high-precision vertical-axis table using a drive with a wedge mechanism and air bearings for vertical guidance has been described here. This combination has allowed for a high motion accuracy that has not been accomplished using conventional rolling methods, and NSK is confident that it will meet demand for ultra-high precision.

We will continue to develop and refine products by meeting specific requirements from the semiconductor manufacturing equipment and inspection equipment sectors where further micronization is anticipated.

Toshinori Sato

Ball Bearings with Excellent Sealing Performance for Fan Clutches

Automotive engines require a cooling system, which includes a fan clutch located in the front of the engine. The fan clutch controls the heat balance of the cooling water that circulates in the engine block and radiator. Global demand for automobiles has led to a growing need for fan clutches that can be used under harsh conditions and in dusty or muddy/watery environments. Conventional bearings for fan clutches were equipped with the same seals at both sides to facilitate mounting. In recent years, however, vehicles are being used in such harsh conditions that a mass of dust can adhere to areas around the seal on the atmosphere side. This accelerates seal wear, resulting in abnormal noise generation due to dust or mud water that has permeated into the bearing.

NSK has developed high sealing property bearing seals that are superior in dust and mud water tightness, required of seals on the atmosphere side (Photo 1), as described in this article.

1. Applications and Structure

The new bearing seals are used to support fan clutches (Figure 1), which keep engines running at an optimal temperature and also maintain fuel efficiency. There are two types: one for the atmosphere side to prevent dust and mud water and the other for the oil side to prevent silicon oil. The bearings are driven by an engine accessory belt.

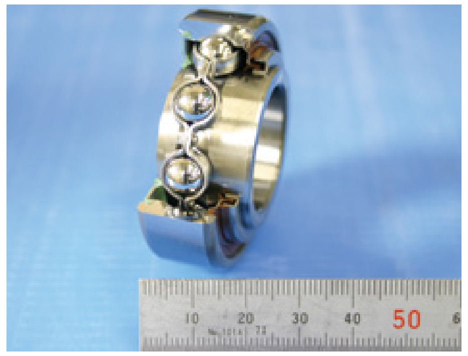

Photo 1 Ball bearing with excellent sealing performance

2. Features

- Resistance against dust and mud water

Figure 2 shows the seal structure, designed with the aim of high sealing performance under harsh conditions. The concept underlying the design was aimed at increasing the number of barriers against sandy dust and mud water by means of installing a slinger and increased seal lips (2-lip ⇒ 3-lip) to prevent foreign objects from entering the bearing.

Figure 3 shows comparative evaluation results of dust resistance and mud water resistance between the new products and conventional products. The results confirm that the new products are about 30 times more resistant to dust and about 8 times more resistant to water.

3. Conclusion

We are confident that incorporating high sealing performance seals in the bearings for fan clutches extends the bearing service life, improves fan clutch reliability, and ultimately leads to more reliable vehicles.

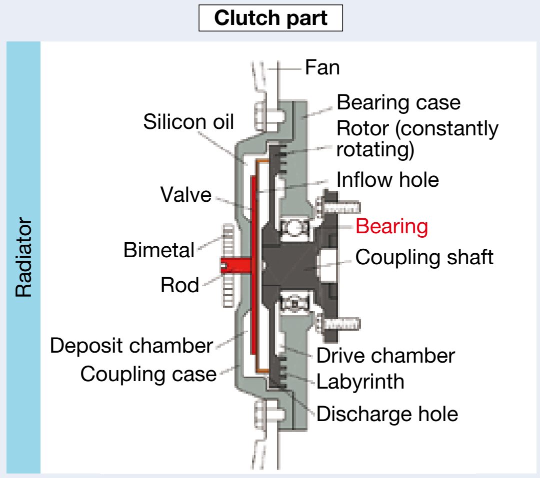

Radiator temperature: High
Valve rotates due to bimetal → Inflow hole opens
→ Silicon oil flows in the drive chamber due to centrifugal force
→ Rotational torque increases
→ Case-attached fan rotates
⇒ Radiator cools

Radiator temperature: Low
Valve rotates due to bimetal → Inflow hole closes
→ Silicon oil in the drive chamber returns due to centrifugal force to the deposit chamber through the discharge hole
→ Rotational torque decreases → Fan slows down
⇒ Radiator stops cooling

Fig. 1 Fan clutch structure

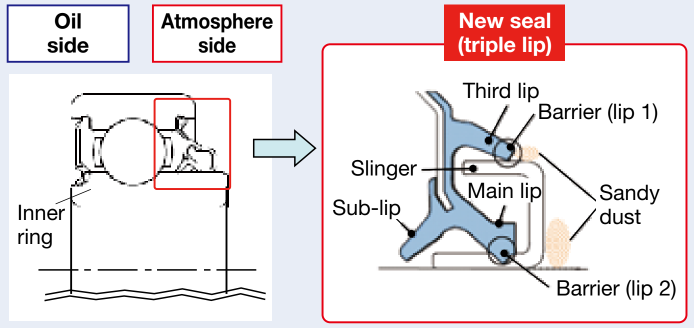

Fig. 2 Seal structure

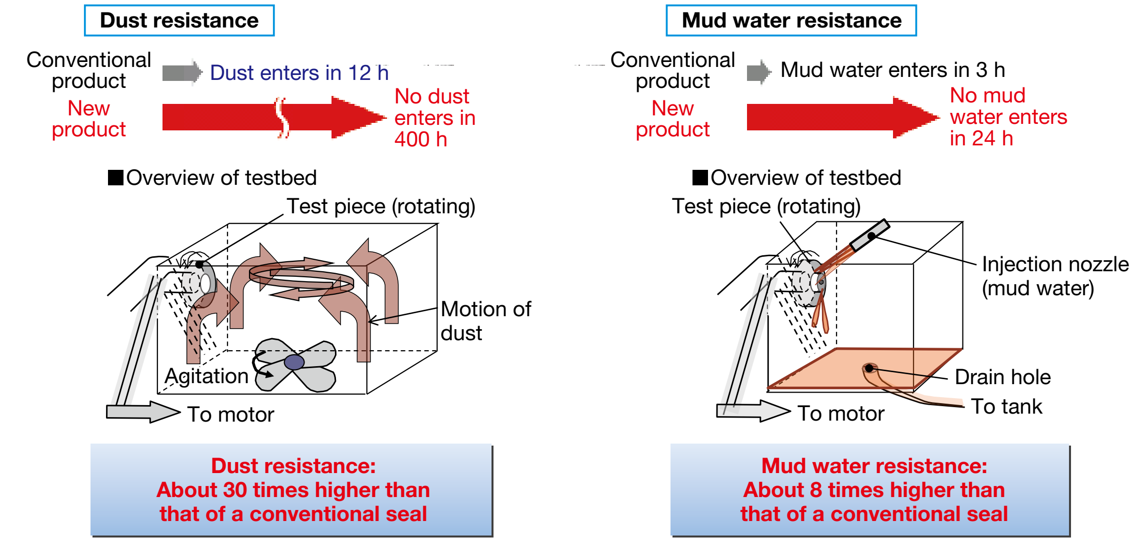

Dust resistance: About 30 times higher than that of a conventional seal

Mud water resistance: About 8 times higher than that of a conventional seal

Fig. 3 Seal performance test results

New Ball Bearing with a Retainer Plate for Automobile Transmissions

A trend to improve fuel efficiency in automobiles has led to continuous demand for higher mechanical efficiency and more compact, lightweight transmission systems (TMs). NSK developed and introduced ball bearings with a retainer plate that allows for an overall shorter TM (Photo 1). In recent years, demand for TMs has been growing, especially in newly developing countries. However, with conventional plates, automated mounting onto the bearing outer ring is difficult. What arose was the strong possibility that supply would barely be able to keep up with demand. NSK's new ball bearing with a retainer plate not only increases productivity by automating plate mounting and due to plate load capacity; they also make it possible to meet the demand for diversified plate geometry. The structure and features of the bearing are described here.

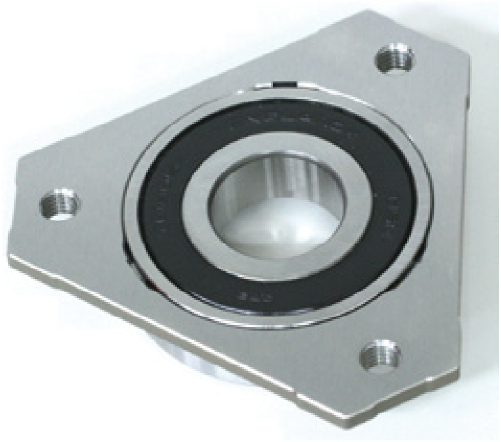

Photo 1 Ball bearing with a retainer plate for automobile transmissions

1. Structure and Specifications

The product consists of two parts: a bearing that has an outer ring with stepping (Figure 1 (a)) and a new retainer plate with a bore that is outfitted with slotting (Figure 1 (b)). When mounting the plate onto the outer ring, tab is formed by a press machine. The plate can be automatically mounted onto the outer ring and also has a non-separable structure (Figure 1 (c)).

2. Features

(1) Improvement of productivity by automated mounting

Due to the structure of conventional products, automated mounting was difficult when using a specially shaped snap ring to secure the plate to the outer ring. The new product allows for automated mounting, owing to its structure, while forming tab by press machine.

(2) Improvement of plate load capacity

The higher the engine torque, the heavier the bearing load. As a result, the plate tightening load increases, which boosts the stress applied to the outer ring stepping. In conventional products equipped with a snap ring groove, increasing the fillet radius is difficult. The new product can be outfitted with an enlarged corner of an outer ring stepping by eliminating a snap ring groove. Thus, with reduced stress, the bearing can withstand greater tightening load (Figure 2).

(3) Structure accommodating various plate geometries

In view of increasing demand for more compact TMs and their diversified layout, some conventional products with a plate fixing snap ring may not exhibit compatibility between plate strength and bearing mountability. The product accommodates various plate geometries by using press die to place the plate tab at the optimal location.

3. Applications and Potential Results

The new bearings are intended mainly for use as the shaft support of automotive transmission, especially manual transmission (MT) and dual clutch transmission (DCT).

The new product has achieved a more compact, lightweight TM by shortening the TM's overall length by the thickness of the retainer plate (approximately 4 mm). Moreover, a reduction of TM vibration caused by the snap ring, by eliminating axial gap, is expected (Figure 3).

4. Conclusion

By enhancing conventional ball bearings with a retainer plate, the new ball bearing with a retainer plate adequately meets the increasing demand in the growing TM market. Continuous efforts are needed to make more compact, lightweight TM support bearings, for which demand is increasing in Europe and China.

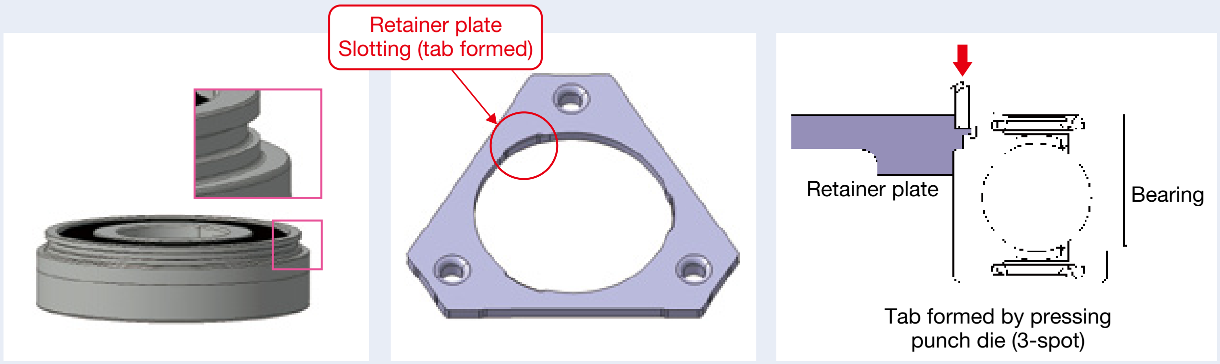

(a) Bearing (b) Retainer plate (c) Mounting method

Fig. 1 Structure of the new retainer plate

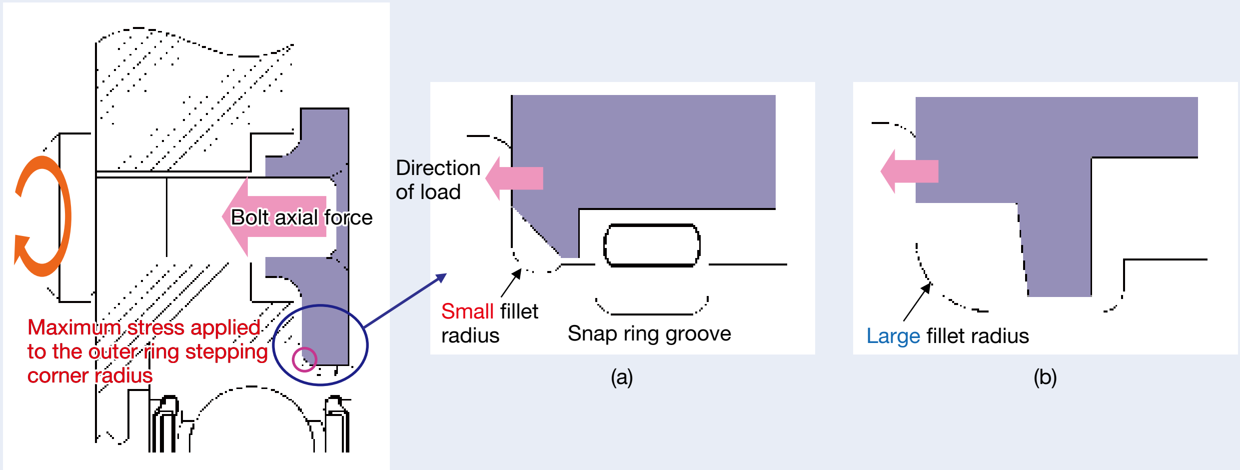

The fillet radius cannot be enlarged in order to allow for a snap ring groove, which holds the snap ring (Figure 3 (a)).
The fillet radius can be enlarged by eliminating a snap ring groove (Figure 3 (b)).

Fig. 2 Structure with improved plate load capacity

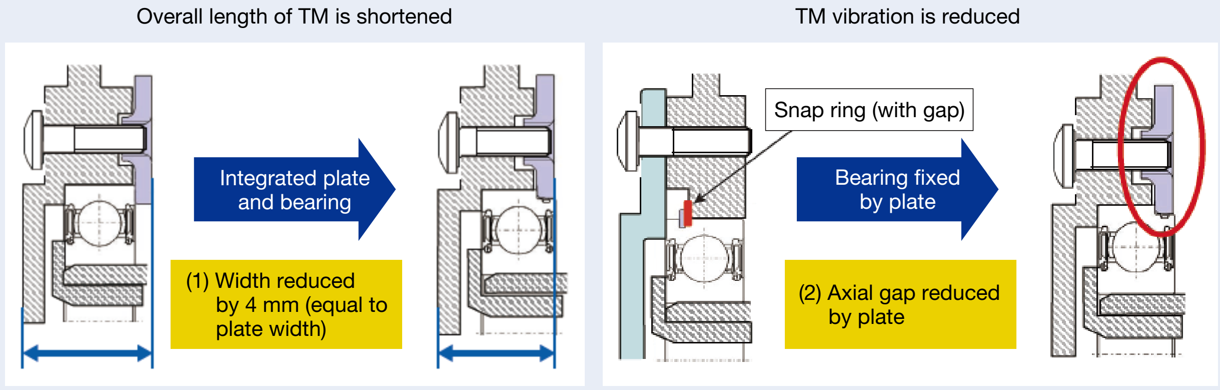

Fig. 3 Effects on transmission

The World's Lightest* Electric Power Steering System

A strong international movement is underway to control CO_2 emissions and strengthen global environmental conservation, and European countries have launched stricter exhaust gas regulations such as Euro6. Against this backdrop, the role of automotive electric power steering (EPS) is becoming increasingly important.

While developing its EPS systems, NSK has focused on improving environmental performance, not only for safety but also for making automobiles lighter, more compact, and more fuel-efficient. NSK recently developed the world's lightest* EPS system equipped with a column-type tilt mechanism for adjusting the steering vertical angle. In this article, we describe the system, which enhances both safety and operational sustainability.

1. Features

The weight of the EPS system (Figure 1) was reduced by 13% compared to that of a conventional EPS by using more compact components in the gear box: a torque sensor, reduction gear, as well as the gear box itself. Moreover, safety has been enhanced as a result of the initial test of the torque sensor's monitoring function, which enables the EPS to continue operating even when battery supply capacity is low during an idle reduction.

2. Advantages of the New EPS

(1) Weight reduction (Figure 2)

- Torque sensor: Mechanical components were downsized by optimizing the design of the sensor mechanism structure. However, sensitivity, as a trade-off, tended to decrease. Therefore, the compatibility of downsizing and necessary sensitivity was realized by optimizing the mechanical structure and redesigning the electro-magnetic circuit. Consequently, functionality was improved and weight was reduced by 24% compared to that of a conventional product, following ECU interface and sensor assembly process steps.
- Reduction gear: Surface pressure and other contact conditions were analyzed when the contact area on the gear teeth moves according to the meshing that changes (Figure 3). Contact stress was reduced by optimizing the tooth profile, and the gear diameter was reduced by implementing an NSK design method. The weight could therefore be decreased by 32% compared to that of a conventional component.
- Gear box: Controlling the blowhole in die casting increased both strength and stretch, thereby reducing wall thickness while also retaining rigidity. To avoid deteriorated metal flow, possibly the result of the thinned wall, metal flow/solidification analysis (Figure 4) was conducted in addition to conventional structure analysis. This was done to increase casting quality and optimize the shape of the thin wall, and an overall 23% reduction in weight, compared to that of a conventional component, was achieved.

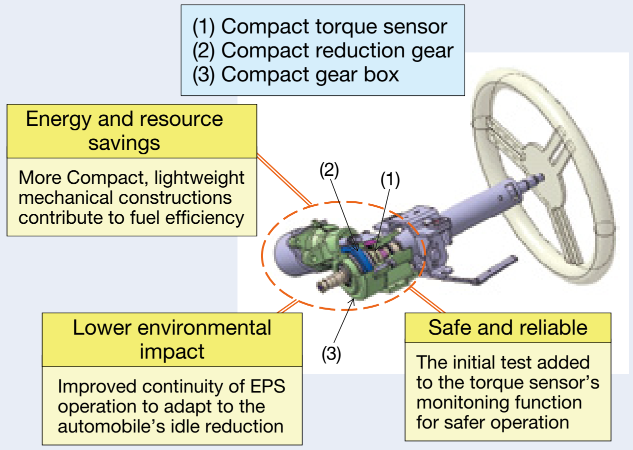

Fig. 1 The world's lightest* column-type EPS system equipped with a tilt mechanism

Part		Weight reduction	
Torque sensor	Shaft	▲19%	▲24%
	Coil	▲49%	
	Sleeve	▲40%	
Reduction gear		▲32%	
Gear box		▲23%	
EPS: Total		▲13%	

Fig. 2 Weight reduction

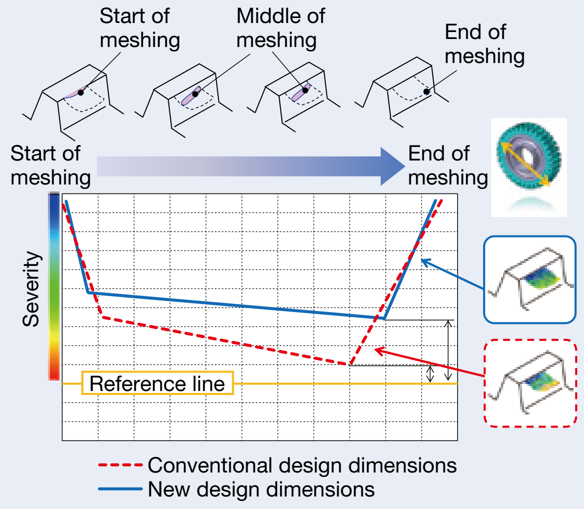

Fig. 3 Analysis of worm and reduction gear meshing

(2) Improving operational continuity during an idle reduction

A battery's power feeding capability is low during an idle reduction, as the generation of electricity or charge from the engine stops. To address this, the drive voltage of the torque sensor was lowered so that the EPS would continue to operate, even when battery power feeding decreased (Figure 5).

(3) Enhancing safety

Until recently, torque sensors in EPS systems have been used to monitor functionality. NSK has made it possible to perform the initial test to monitor the torque sensor's monitoring function and check if it is operating normally (Figure 6). This has enhanced the safety of the EPS system.

3. Application

The product can be utilized in compact or midsize cars, driven in regions around the world, as a column-type EPS.

4. Conclusion

Due to its lightness and better utilization for an idle reduction feature, NSK's new ESP system, the world's lightest*, equipped with a column-type tilt mechanism, allows for energy and resource savings, while its new initial testing function contributes to both safety and security.

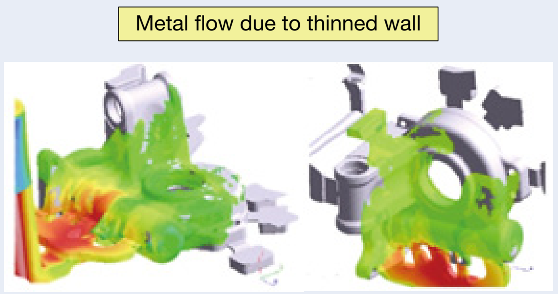

Fig. 4 Casting analysis

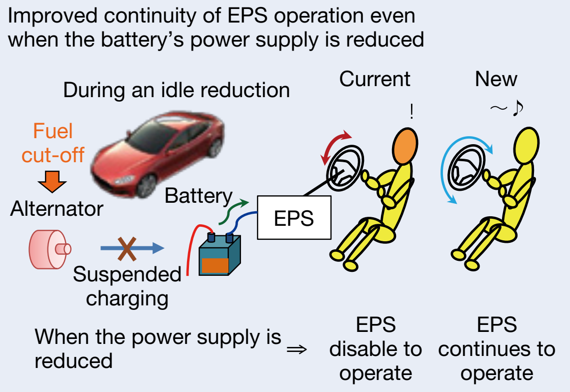

Fig. 5 Utilization for an idle reduction

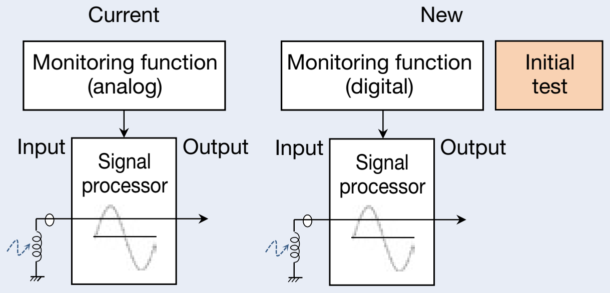

Fig. 6 Addition of the initial test with the torque sensor's self monitor

---

*According to NSK's research

spaceaCRYO: New High-Performance Ceramic Ball Bearings for Liquefied Gas Pumps

Cargo depots and tankers have pumps for receiving or transporting liquefied gas. In recent years, demand has been growing for liquefied natural gas and larger plants, leading to the need for bearings with longer service life in pumps for stable operations. Besides longer life, these bearings must meet a new requirement for electric corrosion resistance because inverter-controlled motors are increasingly being used to boost pump efficiency. To that end, as a material for the rolling element (balls) of the bearing, ceramics are preferred to conventional stainless steel due to their excellent wear resistance and insulation. However, conventional ceramic materials (silicon nitrides) have little temperature expansion, just one-fourth of that of the inner/outer rings (stainless steel), which may cause fluctuation in bearing clearance, depending on the degree to which the temperature changes. Therefore, bearings had to be chosen according to their initial clearance for each liquefied gas at different temperatures.

This article discusses NSK's new high-performance ceramic ball bearings for liquefied gas pumps, spaceaCRYO (Photo 1), which, with only one clearance, can be used for all types of liquefied gases.

1. Construction, Structure, and Specifications

Figure 1 shows the configuration of the new bearings. The outer and inner rings are made of stainless steel whereas the new ceramic material with excellent wear resistance and insulation is used for the rolling element (balls), and a special resin material with excellent self-lubrication capability is used for the cage. Different from conventional ceramic material (silicon nitrides), the new ceramics used for the rolling element have a similar linear expansion coefficient to that of the outer/inner ring materials, and so there is little temperature-induced fluctuation in the internal clearance.

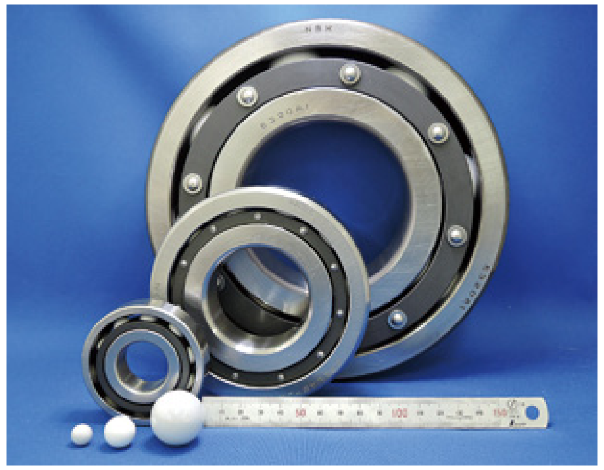

Photo 1 spaceaCRYO: new high-performance ceramic ball bearings for liquefied gas pumps

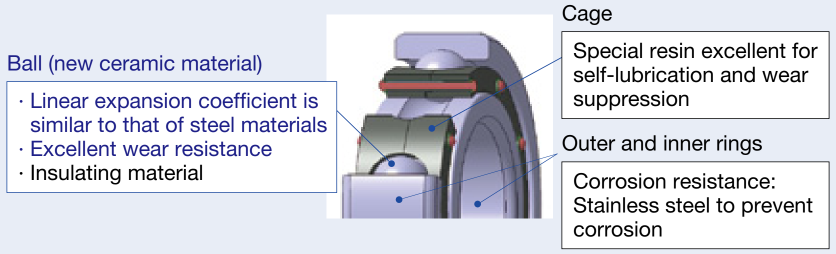

Fig. 1 Bearing configuration

2. Features

(1) Just one bearing type can be used for each kind of liquefied gas, as the fluctuation in the bearing internal clearance is minor in a wide temperature range. Figure 2 shows the relationship between temperature and internal clearance.

(2) The maintenance period can be extended, as its wear resistance is superior to that of stainless-steel ball bearings. Figures 3 and 4 show the results of a rotation test in liquid nitrogen and a four-ball wear test in water, respectively.

(3) Damage due to electric corrosion can be avoided, as the balls are made of a ceramic insulating material.

Table 1 shows the effectiveness of the developed products as related to (1) to (3) above.

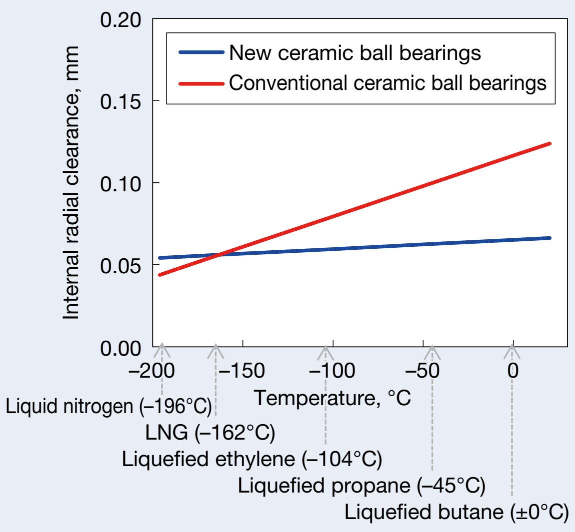

Fig. 2 Change in internal radial clearance of ball bearing 6314 based on temperature

Table 1 Effectiveness of new bearings

Required Function for Bearings	Stainless-steel Ball Bearings	Conventional Ceramic Ball Bearings	New Ceramic Ball Bearings
Low vibration in a wide temperature range ⇒ Minor fluctuation in clearance	○	×	○
High speed, long life ⇒ Wear resistance	△	○	○
Electric corrosion resistance ⇒ Insulation property	×	○	○

3. Applications

The new bearings can be used not only in various pumps for liquefied gases, including liquefied natural gas, but can also be used as a means of improving pump reliability.

4. Conclusion

Ahead of other manufactures, NSK has developed various bearings for liquefied gas pumps and attained a high level of trust in the market. We remain committed to furthering stable operations and the extension of the maintenance period of liquefied gas pumps.

Test bearing: Angular ball bearing (outer diameter: ϕ62 mm, inner diameter: ϕ25 mm, width: 17 mm)
Test condition: 6 000 rpm
Soaked in liquid nitrogen (–196°C)

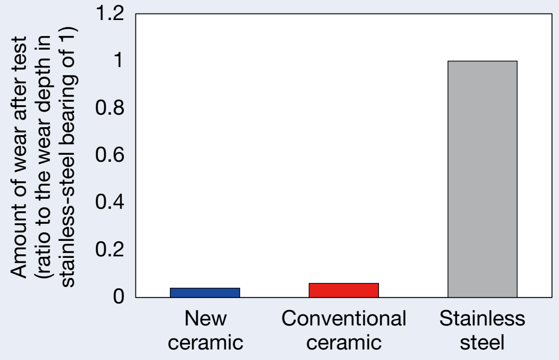

Fig. 3 Comparison of wear in liquid nitrogen

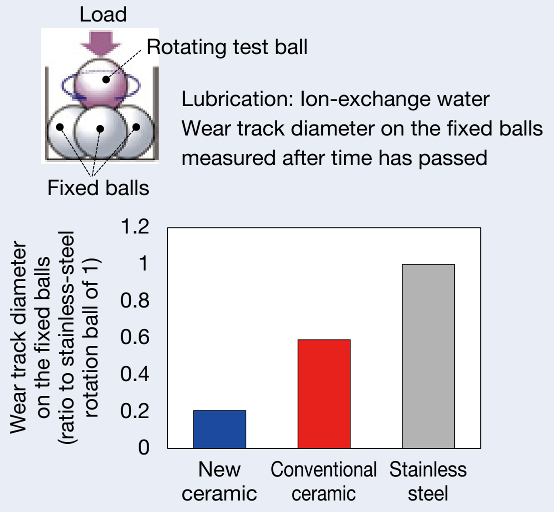

Fig. 4 Four-ball wear test in water

Spherical Roller Bearings Featuring High Reliability and Excellent Sealing Performance for Conveyor Pulleys in Mines

The downtime of mine conveyors that are from a few kilometers to 20 km in length has a significant impact on productivity, whether this is due to failure or maintenance work. Therefore, these facilities must be reliable enough to sustain stable operations for 24 hours a day throughout the year, even when under harsh conditions and exposed to dust.

In these conveyor pulleys, spherical roller bearings with a high load capacity are generally used to absorb axial deflection. There are two types of spherical roller bearings: the open type (without a seal) and the closed type (with a seal). The first is more common; though, it can cause premature bearing damage due to foreign object infiltration, whereas the second type must deal with improper mounting because of the need for seal space to maximize seal performance and its inability to facilitate the measurement of clearance when mounting bearings onto a facility. To solve these problems, NSK developed spherical roller bearings featuring high reliability and excellent sealing performance, which are the same size as conventional bearings, demonstrate sufficient sealing performance, and achieve a long service life (Photo 1).

1. Features

(1) Full compatibility with conventional bearings (open type)

The new products are in compliance with an ISO dimension and can replace conventional bearings of the same size (Figure 1).

(2) Extended life materials

Load capacity has improved and the internal bearing design has become more compact as a result of using an NSK material in the inner and outer rings and applying a special heat treatment process. This has brought load capacity equal to or even greater than that of conventional products while ensuring seal space, whereas the size is the same. In addition, our field test of conventional products and the newly developed bearings revealed that only the former had flaking and the latter was not damaged. Figure 2 shows a comparison of service lives, including the remaining life of the developed product.

(3) A high sealing performance technology

Using a seal with a garter spring and time-proven measures against foreign matter achieved a high sealing effect. Figure 3 shows a comparison of foreign matter found inside the internal bearing after performing the same field test, as described in (2) above.

(4) A bolt-fastening type seal holder

Flaking or heat seizure damage caused by improper mounting clearance can be prevented since the clearance measurement can be performed by removing the seal when mounting the bearing.

2. Specifications

Figure 4 shows the specifications of the new spherical roller bearings.

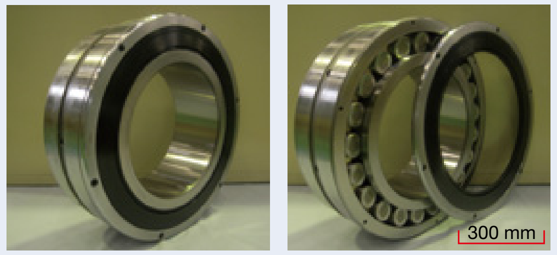

Photo 1 Spherical roller bearings featuring high reliability and excellent sealing performance for conveyors

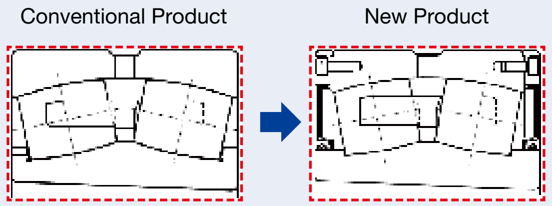

The new and conventional products have the same dimensions

Fig. 1 Cross sections of a conventional bearing and a new bearing

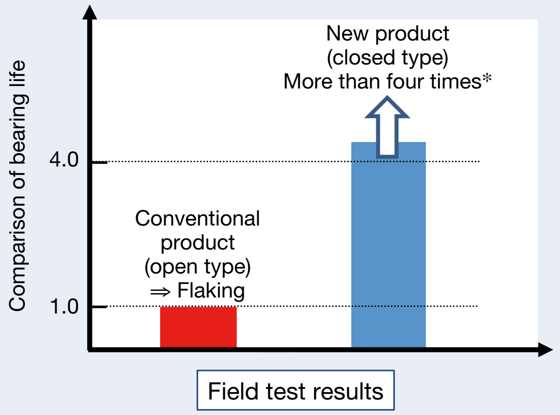

*Including estimated remaining life based on fatigue analysis after a field test

Fig. 2 Comparison of bearing life

3. Applications

The new bearings are suitable for use in mine conveyor pulleys where they are needed for sustaining stable operation under harsh conditions and are exposed to dust. The bearings are available in the sizes listed in Tables 1 and 2.

4. Conclusion

The new bearings will boost mining operation productivity by extending service life by more than four times that of conventional products, even under harsh conditions.

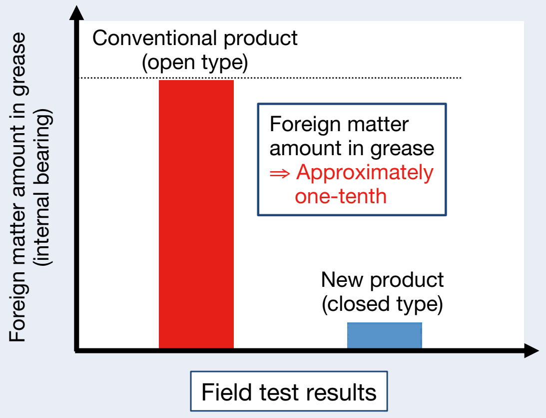

Fig. 3 Comparison of particles in grease

Table 1 231 Series product lineup

Basic number	Inner diameter (mm)	Outer diameter (mm)	Width (mm)	Basic number of a conventional product (open type)
HTF170SLE316	170	280	88	23134K
HTF180SLE316	180	300	96	23136K
HTF190SLE316	190	320	104	23138K
HTF200SLE316	200	340	112	23140K
HTF220SLE316	220	370	120	23144K
HTF240SLE316	240	400	128	23148K
HTF260SLE316	260	440	144	23152K
HTF280SLE316	280	460	146	23156K
HTF300SLE316	300	500	160	23160K
HTF320SLE316	320	540	176	23164K
HTF340SLE316	340	580	190	23168K
HTF360SLE316	360	600	192	23172K
HTF380SLE316	380	620	194	23176K
HTF400SLE316	400	650	200	23180K
HTF420SLE316	420	700	224	23184K
HTF440SLE316	440	720	226	23188K

Table 2 222 Series product lineup

Basic number	Inner diameter (mm)	Outer diameter (mm)	Width (mm)	Basic number of a conventional product (open type)
HTF120SLE226	120	215	58	22224K
HTF130SLE226	130	230	64	22226K
HTF140SLE226	140	250	68	22228K
HTF150SLE226	150	270	73	22230K
HTF160SLE226	160	290	80	22232K

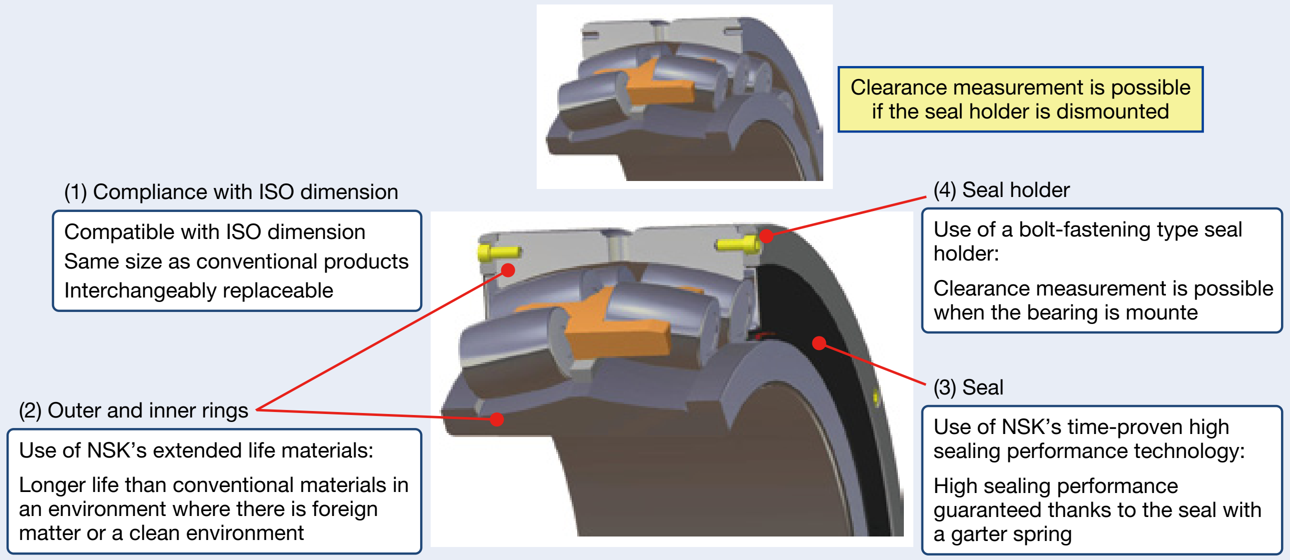

Fig. 4 Specifications of the new bearing

Ball Bearings for Ultra-High-Speed Rotary Motors

Amid a recent trend for more compact and lighter products in the domestic vacuum cleaner sector, air suction fans have been downsized to the extent that the current diameter is as small as one-third of a conventional product. Fan motors are required to rotate faster than ever to empower those small-diameter fans so that they maintain sufficient suction power. Therefore, their bearings must meet a high-speed rotation requirement. Consequently, their specifications for $d_m \cdot n$ value, i.e., a high-speed rotation property (rolling element pitch diameter [mm] × rotation number [rpm]), need to endure an operation in the million range, which is 1.5 times more than that of a conventional product (Figure 1).

To meet such high-speed specifications for bearings, NSK has released ball bearings for ultra-high-speed rotary motors (Photo 1), which achieve a $d_m \cdot n$ value that goes beyond the million range. These bearing incorporate optimally designed dedicated cages made of a high-strength material and are described in this article.

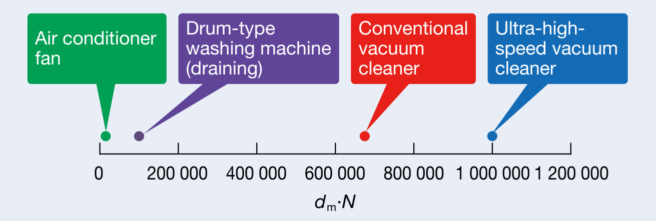

Fig. 1 Example of the $d_m \cdot N$ value of bearings used in home appliances

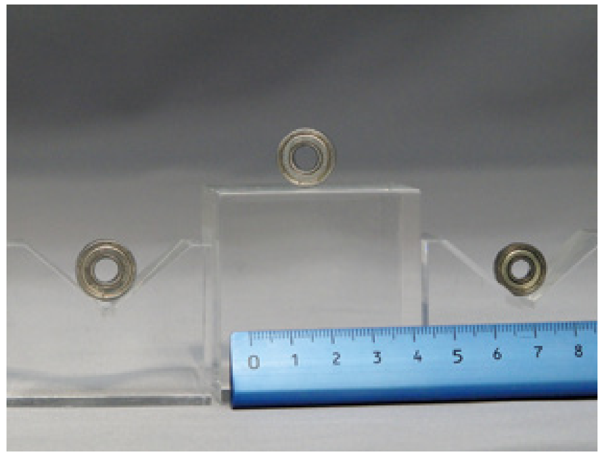

Photo 1 Ball bearings for ultra-high-speed rotary motors

1. Construction, Structure, and Specifications

In conventional designs, high-speed rotation-induced centrifugal force deforms cages, resulting in wear or rupture caused by interference with other components (Photo 2).

The cages of the new bearings are made of a high-strength material that was developed with an optimized design based on FEM analysis. As a result, they meet the operational requirement of the million range of the $d_m \cdot n$ value (Figure 2).

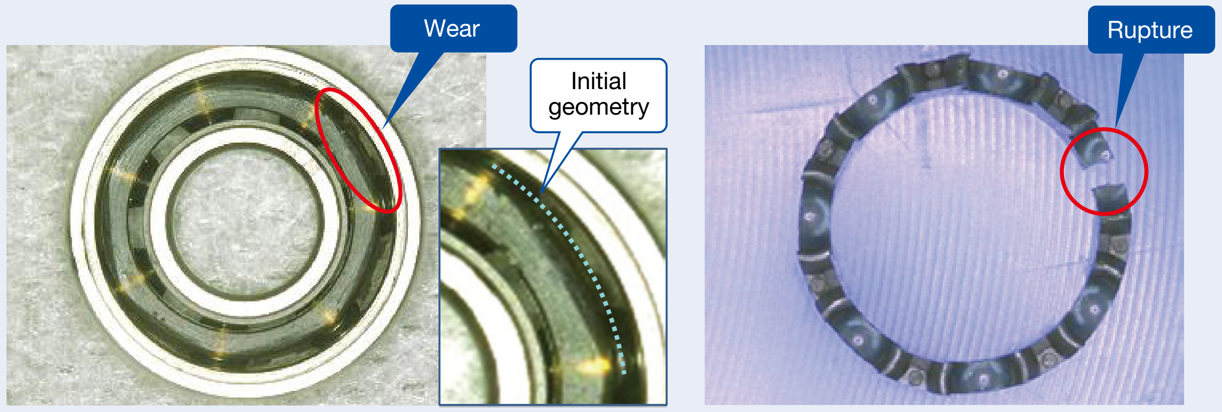

Photo 2 Conventional bearing

2. Features

The high-rigidity cages made of a high-strength material with optimized geometry allow for the bearings to endure an operation in the million range of the $d_m \cdot N$ value (Photo 3).

3. Applications

To achieve ultra-high speed rotation, the developed products are suitable for use in the fan motors of compact, lightweight vacuum cleaners with high suction power as well as in high-speed rotary motors that operate in the million range of the $d_m \cdot N$ value.

4. Conclusion

We have introduced ball bearings for ultra-high-speed rotary motors, which were developed for use in motors of vacuum cleaners. We remain committed to developing products to meet emerging trends in the areas of home electric appliances for better comfort, health, and energy savings.

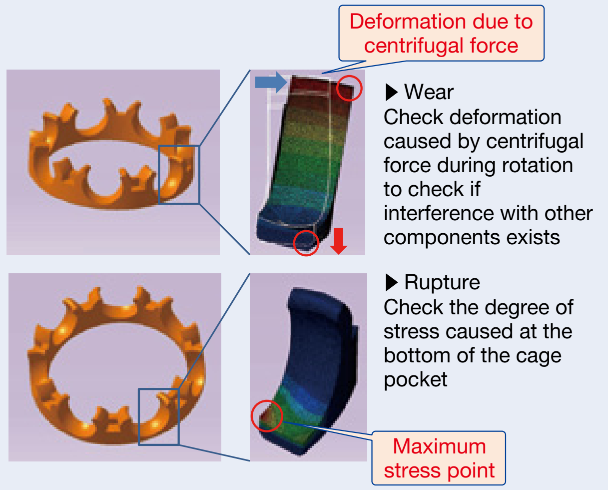

Fig. 2 FEM analysis results

Test conditions
Test bearing: 696
Rotation number: 100 000 rpm
$d_m \cdot N$: 1.05 million
Operation pattern: Rotation for 10 min. and pause for 5 min.

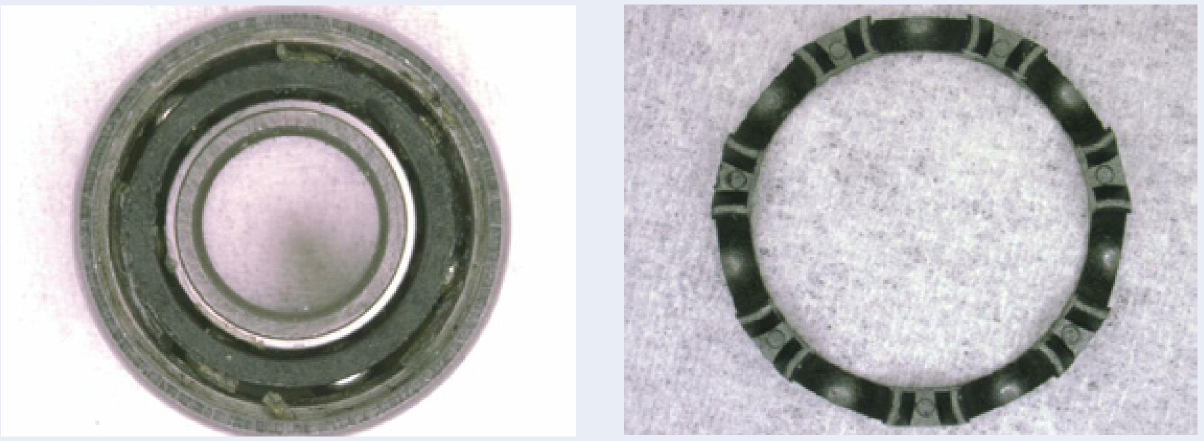

Photo 3 Ultra-high-speed durability test results

ROBUSTSHOT Bearings: Direct Lubrication Angular Contact Ball Bearings for Machine Tool Spindles

In recent years, there has been growing demand for high-speed main spindles for machine tools as manufacturers work to improve machining efficiency. Another growing need for promoting efficiency in productivity is to support 5-axis machines that are capable of processing complex configuration workpieces without performing a tooling change. For the 5-axis machine tool spindles, of which spindles and tables rotate, demand is rising to shorten the axial length of the spindles so as to meet the requirement for conserving space by shortening the turning radius, as well as the power saving-oriented requirement for reducing turning inertia and weight.

To meet these needs, NSK has developed a series of ROBUSTSHOT direct lubrication angular contact ball bearings, which are superior to conventional bearings for machine tool spindles in terms of high-speed rotation, low heat generation, and high rigidity (Photo 1), as described in this article.

1. Bearing Specifications

ROBUSTSHOT bearings have a circumferential oil groove around the outer ring and communicating oil holes around the groove in the axial direction. These specifications are common to all ROBUST series bearings with an inner diameter of $\phi30$ mm to $\phi120$ mm (Figure 1).

Photo 1 ROBUSTSHOT bearing

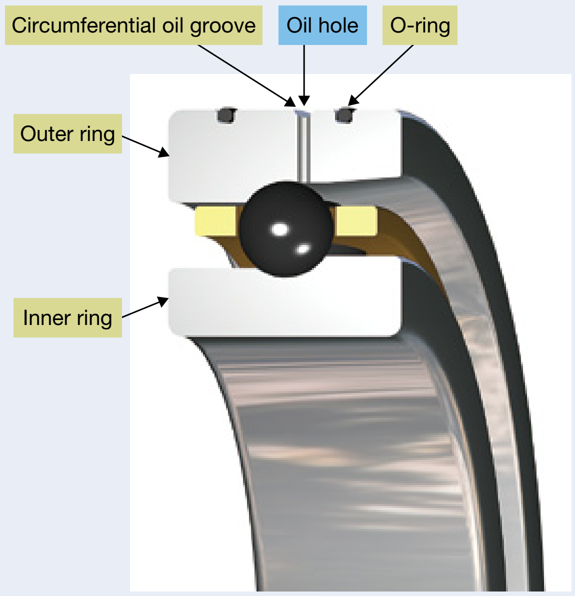

Fig. 1 Cross-section of a ROBUSTSHOT bearing

2. Features

(1) More reliable lubrication

In conventional oil-air lubrication fed from the side face, the lubricating oil supply is impeded by an air curtain caused by the high-speed rotation of the inner ring or cage. In contrast, ROBUSTSHOT bearings facilitate a stable high-speed operation with improved lubricating ability, owing to the direct lubricating oil supply from the outer ring (Figure 2).

(2) Downsizing of the spindle

A lubrication spacer, previously indispensable for side face feeding lubrication-type bearings, is no longer used. Therefore, the width of the spacer can be reduced. This also reduces the main spindle length (Figure 3), which in turn downsizes its turning space and thereby ensures a larger machining area. Furthermore, the shortened main spindle length also leads to weight reduction and higher critical speed.

3. Applications

The new ROBUSTSHOT bearings can be used for machine tool main spindles that operate in a high-speed range, in which oil lubrication is applied and the previous ROBUST series can be replaced.

4. Conclusion

Compared to conventional side face feeding lubrication-type bearings, the new ROBUSTSHOT bearings further improve lubrication performance in the high-speed range and also allow for downsizing of the main spindle. Consequently, NSK is confident that using these bearings will contribute to a higher level of productivity.

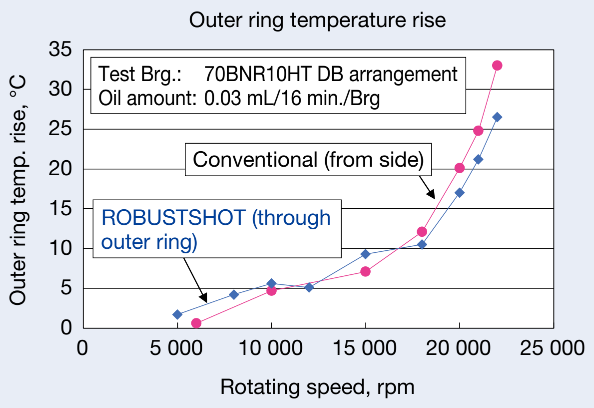

Fig. 2 Comparison of outer ring temperature rise

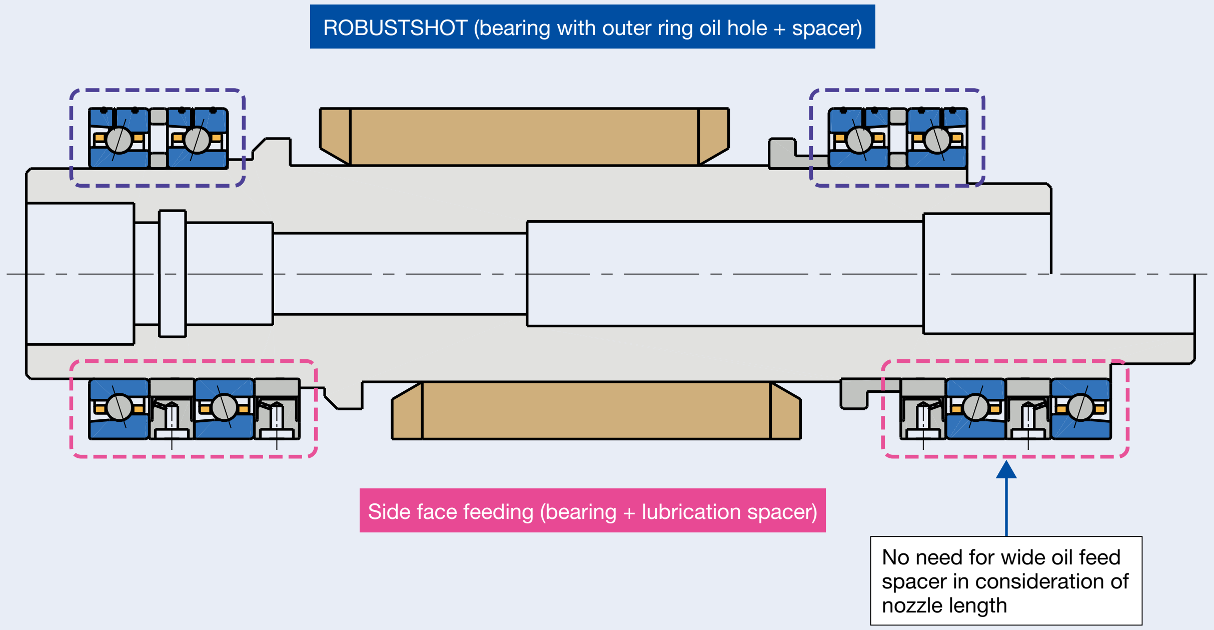

Fig. 3 Downsizing of the spindle

Ultra-Large Ball Screws

Although ball screws are versatile in their use, especially when it comes to injection molding machines and press machines, the drive method of each shaft has been shifting from hydraulic to electric using ball screws and rotary motors due to the improvement and stabilization of product quality, the optimization of productivity, and other reasons. However, in the injection molding of large products, including automobile bumpers and instrument panels, where very heavy loads are applied onto individual drive shafts, ball screws with a conventional load capacity cannot ensure sufficient product life. Thus, drive methods, such as the hydraulic drive method and electrohydraulic hybrid method*, have been used up to recently.

NSK has recently developed ultra-large ball screws (Photo 1) with far greater load capacity than that of ball screws for high load drive, which are applicable to a range where the hydraulic or hybrid method are used. Switching from a hydraulic system to an electric system leads to these advantages.

- Improved accuracy for molded pieces
- Reduction in the defective rate of the molded pieces by improving controllability and responsiveness
- High-functionality molding and an expanded application range
- Reduced running costs (the electricity cost is half to one-third lower than that for a hydraulic system)
- Improved safety and environment at production sites

Photo 1 New ultra-large ball screw

1. Features

By using NSK's originally developed nut thread grinder and high precision measurement techniques, the overall grindable nut length has been extended, resulting in the following advantages.

(1) High capacity

Service life is at least 2.8 times longer than that of a conventional large ball screw (Figure 1).

(2) Load bearing

Permissible axial load is at least 1.3 times more than that of a conventional large ball screw (Figure 1). A single shaft can bear a maximum of 200 tons of load.

(3) Full variations

Optimal lead is selectable for each shaft diameter.

Ball screw specifications: ϕ200, lead 32 mm

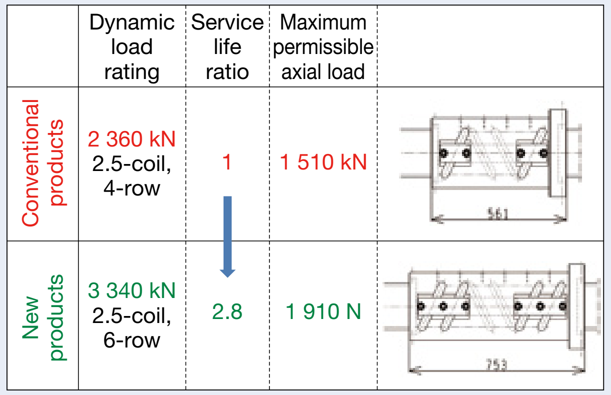

	Dynamic load rating	Service life ratio	Maximum permissible axial load
Conventional products	2 360 kN 2.5-coil, 4-row	1	1 510 kN
New products	3 340 kN 2.5-coil, 6-row	2.8	1 910 N

Fig. 1 Comparison of specifications between conventional ball screws and new ball screws

2. Specifications

- Table 1 shows specifications of general models.
- Table 2 provides the lineup (combination of shaft diameter and lead).
- The ball holding piece NSK S1 is used to prevent the contention of balls.
- The HTF-SRE method for high-speed specifications can be used in cases where the permissible rotating speed is exceeded (permissible $d{\cdot}n$ value: 100 000).
- The load bearing option with an improved permissible axial load is also available.
- Tolerance class: JIS Ct7 class
- Axial clearance: 0.050 mm or less

3. Applications

The new products are suitable for use in machines for electric injection molding, servo press, broaching, die-casting and others, which have to meet requirements for a high capacity and load bearing.

Table 1 Specifications of general models

Model	Lead (mm)	Shaft diameter (mm)	Nut length (reference value) (mm)	Basic load rating (kN)		Permissible axial load (kN)	Permissible rotating speed (rpm)
				Dynamic rating	Static rating		
HTF14025-21-S1	25	140	743	2 500	9 820	1 102	500
HTF16025-20-S1	25	160	743	2 640	11 000	1 276	437
HTF14030-17.5-S1	30	140	761	2 660	9 520	1 047	357
HTF16030-17.5-S1	30	160	761	2 840	10 900	1 356	312
HTF20030-17.5-S1	30	200	791	3 210	13 900	1 823	250
HTF14032-15-S1	32	140	753	2 880	9 480	1 095	357
HTF16032-15-S1	32	160	753	3 020	10 700	1 412	312
HTF20032-15-S1	32	200	753	3 340	13 700	1 910	250

Table 2 Lineup (combination of shaft diameter and lead)

Unit: mm

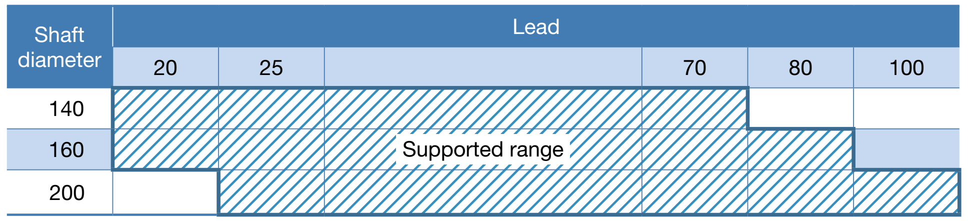

Shaft diameter	Lead					
	20	25		70	80	100
140	▨	▨	▨	▨		
160	▨	▨	▨ Supported range	▨	▨	
200		▨	▨	▨	▨	▨

4. Conclusion

As grinding ball screws, the new ultra-large ball screws boast the world's top class load capability. By using them with tandem nuts (a method for boosting load capacity by connecting nuts) or using multiple ball screws, it is now possible to replace them with existing hydraulic or hybrid systems in order to support a high-load range operation.

NSK will continue to develop and release products that are needed for facilitating the electrification of various types of equipment.

Reference

1) NSK catalog, "Ultra-large ball screws with the world's top class load capacity," CAT. NO. JSP-160215.

---

*Indicates cases where both hydraulic and electric systems are used in the respective shafts of injection machines (e.g., injection shaft, mold clamping shaft, and ejector shaft), for there is no clear definition of a hybrid system. This includes, for example, cases in which the injection shaft is hydraulic but the clamping shaft is electric.

Worldwide Sales Offices

P: Phone F: Fax ☆: Head Office

NSK LTD.-HEADQUARTERS, TOKYO, JAPAN

Nissei Bldg., 1-6-3 Ohsaki, Shinagawa-ku, Tokyo 141-8560, Japan
INDUSTRIAL MACHINERY BUSINESS DIVISION-HEADQUARTERS
P: +81-3-3779-7227 F: +81-3-3779-7644
AUTOMOTIVE BUSINESS DIVISION-HEADQUARTERS
P: +81-3-3779-7189 F: +81-3-3779-7917

●Africa

South Africa:

NSK SOUTH AFRICA (PTY) LTD.

SANDTON 25 Galaxy Avenue, Linbro Business Park, Sandton 2146, South Africa
P: +27-11-458-3600 F: +27-11-458-3608

●Asia and Oceania

Australia:

NSK AUSTRALIA PTY. LTD.

MELBOURNE ☆ 100 Logis Boulevard, Dandenong South, Victoria, 3175, Australia
P: +61-3-9765-4400 F: +61-3-9765-4466

SYDNEY Suite A315, 20 Lexington Drive, Bella Vista, New South Wales, 2153, Australia
P: +61-2-9839-2300 F: +61-2-8824-5794

BRISBANE 1/69 Selhurst Street, Coopers Plains, Queensland 4108, Australia
P: +61-7-3347-2600 F: +61-7-3345-5376

PERTH Unit 1, 71 Tacoma Circuit, Canning Vale, Western Australia 6155, Australia
P: +61-8-9256-5000 F: +61-8-9256-1044

New Zealand:

NSK NEW ZEALAND LTD.

AUCKLAND 3 Te Apunga Place, Mt. Wellington, Auckland 1060, New Zealand
P: +64-9-276-4992 F: +64-9-276-4082

China:

NSK (SHANGHAI) TRADING CO., LTD.

JIANGSU No.8 NSK Rd., Huaqiao Economic Development Zone, Kunshan, Jiangsu, China (215332)
P: +86-512-5796-3000 F: +86-512-5796-3300

NSK (CHINA) INVESTMENT CO., LTD.

JIANGSU ☆ No.8 NSK Rd., Huaqiao Economic Development Zone, Kunshan, Jiangsu, China (215332)
P: +86-512-5796-3000 F: +86-512-5796-3300

BEIJING Room 1906, Beijing Fortune Bldg., No.5 Dong San Huan Bei Lu, Chao Yang District,
Beijing, China (100004)
P: +86-10-6590-8161 F: +86-10-6590-8166

TIAN JIN Room 06, 09F The Exchange Tower 2, No. 189 NanJing Road, Heping District,
Tianjin, China (300050)
P: +86-22-8319-5030 F: +86-22-8319-5033

CHANGCHUN Room 902-03, Changchun Hongwell International Plaza, No.3299 Renmin Street,
Changchun, Jilin, China (130061)
P: +86-431-8898-8682 F: +86-431-8898-8670

SHENYANG Room 1101, China Resources Building, No. 286 Qingnian Street,
Heping District, Shenyang Liaoning, China (110004)
P: +86-24-2334-2868 F: +86-24-2334-2058

DALIAN Room 1805 Xiwang Tower, No.136 Zhongshan Road,
Zhongshan District, Dalian, Liaoning, China (116001)
P: +86-411-8800-8168 F: +86-411-8800-8160

NANJING Room A1 22F, Golden Eagle International Plaza, No.89 Hanzhong Road, Nanjing,
Jiangsu, China (210029)
P: +86-25-8472-6671 F: +86-25-8472-6687

FUZHOU Room 1801-1811, B1#1A Class Office Building, Wanda Plaza, No.8 Aojiang Road,
Fuzhou, China (350009)
P: +86-591-8380-1030 F: +86-591-8380-1225

WUHAN Room 1110, New World International Trade Tower I, No.568 Jianshe Road, Wuhan,
Hubei, China (430000)
P: +86-27-8556-9630 F: +86-27-8556-9615

QINGDAO Room 802, Farglory International Plaza, No.26 Xianggang Zhong Road, Shinan District,
Qingdao, Shandong, China (266071)
P: +86-532-5568-3877 F: +86-532-5568-3876

GUANGZHOU Room 1011-16, Yuexiu Financial Tower, No.28 Zhujiang Road East, Zhujiang
New Town, Guangzhou, Guangdong, China (510627)
P: +86-20-3817-7800 F: +86-20-3786-4501

CHANGSHA Room 1048, 10/F, Zhongtian Plaza, No.766 WuyiRoad, Changsha, Hunan, China (410005)
P: +86-731-8571-3100 F: +86-731-8571-3255

LUOYANG Room 1108, Fangda Hotel, 6 XiYuan Road, LuoYang HeNan, China (471003)
P: +86-379-6069-6188 F: +86-379-6069-6180

XI'AN Room 1007, B Changan Metropolls Center88 Nanguanzheng Steet, Xi'an, Shanxi,
China (710068)
P: +86-29-8765-1896 F: +86-29-8765-1895

CHONGQING Room 2306, Unit B, No.137, Keyuan 2nd Road, Jiulongpo District, Chonqing,
China (400039)
P: +86-23-6806-5310 F: +86-23-6806-5292

CHENGDU Room1117, Lippo Tower, No.62 North Kehua Road, Chengdu, Sichuan, China (610041)
P: +86-28-8528-3680 F: +86-28-8528-3690

NSK CHINA SALES CO., LTD.

JIANGSU No.8 NSK Rd., Huaqiao Economic Development Zone, Kunshan, Jiangsu, China (215332)
P: +86-512-5796-3000 F: +86-512-5796-3300

NSK HONG KONG LTD.

HONG KONG ☆ Suite 705, 7th Floor, South Tower, World Finance Centre, Harbour City, T.S.T,
Kowloon, Hong Kong, China
P: +852-2739-9933 F: +852-2739-9323

SHENZHEN Room 624-626, 6/F, Kerry Center, Renminnan Road, Shenzhen, Guangdong, China
P: +86-755-25904886 F: +86-755-25904883

Taiwan:

TAIWAN NSK PRECISION CO., LTD.

TAIPEI ☆ 11F., No.87, Song Jiang Rd., Jhongshan District, Taipei City 104, Taiwan
P: +886-2-2509-3305 F: +886-2-2509-1393

TAICHUNG 3F. -2, No. 540, Sec. 3, Taiwan Blvd., Xitun Dist., Taichung City 407, Taiwan
P: +886-4-2708-3393 F: +886-4-2708-3395

TAINAN 5F. No.8, Daye 1st Rd., Southern Taiwan Science Park, Tainan City 741,
Taiwan
P: +886-6-505-5861 F: +886-6-505-5061

TAIWAN NSK TECHNOLOGY CO., LTD.

TAIPEI ☆ 11F., No.87, Song Jiang Rd., Jhongshan District, Taipei City 104, Taiwan
P: +886-2-2509-3305 F: +886-2-2509-1393

TAICHUNG 10F-3, No.925, Sec.4, Taiwan Blvd., Xitun Dist., Taichung City 407,
Taiwan
P: +886-4-2358-2945 F: +886-4-2358-7682

TAINAN 5F. No.8, Daye 1st Rd., Southern Taiwan Science Park, Tainan City 741,
Taiwan
P: +886-6-505-5861 F: +886-6-505-5061

India:

NSK INDIA SALES CO.PVT.LTD.

CHENNAI ☆ TVH Beliciaa Towers, 2nd Floor, Block I No.71/1, MRC Nagar Main Road, MRC
Nagar, Chennai-600 028, Tamil Nabu, India
P: +91-44-2847-9600 F: +91-44-2847-9601

GURGAON Unit No-202, 2nd Floor, Block-A, Iris Tech Park, Sector-48, Sohna Road,
Gurgaon-122018, Haryana, India
P: +91-124-4104-530 F: +91-124-4104-532

MUMBAI 321, 'A' Wing, Ahura Centre, 82, Mahakali Caves Road, Andheri (East), Mumbai
-400 093, India
P: +91-22-2838-7787 F: +91-22-2838-5191

Indonesia:

PT. NSK INDONESIA

JAKARTA Summitmas II, 6th Floor, Jl. Jend Sudirman Kav. 61-62, Jakarta 12190, Indonesia
P: +62-21-252-3458 F: +62-21-252-3223

Korea:

NSK KOREA CO., LTD.

SEOUL Posco Center (West Wing) 9F, Western-wing, 440, Teheran-ro, Gangnam-gu,
Seoul, 135-777, Korea
P: +82-2-3287-0300 F: +82-2-3287-0345

Malaysia:

NSK BEARINGS (MALAYSIA) SDN. BHD.

SHAH ALAM ☆ No. 2, Jalan Pemaju, U1/15, Seksyen U1, Hicom Glenmarie Industrial Park,
40150 Shah Alam, Selangor, Malaysia
P: +60-3-7803-8859 F: +60-3-7806-5982

PRAI No.24, Jalan kikik, Taman Inderawasih, 13600 Prai, Penang, Malaysia
P: +60-4-3902275 F: +60-4-3991830

JOHOR BAHRU 88 Jalan Ros Merah 2/17, Taman Johor Jaya, 81100 Johor Bahru, Johor, Malaysia
P: +60-7-3546290 F: +60-7-3546291

IPOH Gr. Floor, 89 Jalan Bendahara, 31650 Ipoh, Perak, Malaysia
P: +60-5-2555000 F: +60-5-2553373

Philippines:

NSK REPRESENTATIVE OFFICE

MANILA 8th Floor The Salcedo Towers 169 H.V. dela Costa St.,
Salcedo Village Makati City, Philippines 1227
P: +63-2-893-9543 F: +63-2-893-9173

Singapore:

NSK INTERNATIONAL (SINGAPORE) PTE LTD.

SINGAPORE 238A, Thomson Road, #24-01/05, Novena Square Tower A, Singapore 307684
P: +65-6496-8000 F: +65-6250-5845

NSK SINGAPORE (PRIVATE) LTD.

SINGAPORE 238A, Thomson Road, #24-01/05, Novena Square Tower A, Singapore 307684
P: +65-6496-8000 F: +65-6250-5845

Thailand:

NSK BEARINGS (THAILAND) CO.,LTD.

BANGKOK 26 Soi Onnuch 55/1 Pravet Subdistrict, Pravet District, Bangkok 10250, Thailand
P: +66-2320-2555 F: +66-2320-2826

Vietnam:

NSK VIETNAM CO., LTD.

HANOI Techno Center, Room 204-205, Thang Long Industrial Park, Dong Anh District,
Hanoi, Vietnam
P: +84-4-3955-0159 F: +84-4-3955-0158

NSK REPRESENTATIVE OFFICE

HO CHI MINH CITY Suite 307, Metropolitan Building, 235 Dong Khoi Street, District 1,HCMC, Vietnam
P: +84-8-3822-7907 F: +84-8-3822-7910

Worldwide Sales Offices

P: Phone F: Fax ☆: Head Office

●Europe

United Kingdom:

NSK EUROPE LTD. (EUROPEAN HEADQUARTERS)

MAIDENHEAD Belmont Place, Belmont Road, Maidenhead, Berkshire SL6 6TB, U.K.
P: +44-1628-509-800 F: +44-1628-509-808

NSK UK LTD.

NEWARK Northern Road, Newark, Nottinghamshire NG24 2JF, U.K.
P: +44-1636-605-123 F: +44-1636-605-000

France:

NSK FRANCE S.A.S.

PARIS Quartier de l'Europe, 2 Rue Georges Guynemer, 78283 Guyancourt, France
P: +33-1-30-57-39-39 F: +33-1-30-57-00-01

Germany:

NSK DEUTSCHLAND GMBH

DUSSELDORF ☆ Harkortstrasse 15, D-40880 Ratingen, Germany
P: +49-2102-4810 F: +49-2102-4812-290

STUTTGART Liebknechtstrasse 33, D-70565 Stuttgart-Vaihingen, Germany
P: +49-711-79082-0 F: +49-711-79082-289

WOLFSBURG Tischlerstrasse 3, D-38440 Wolfsburg, Germany
P: +49-5361-27647-10 F: +49-5361-27647-70

Italy:

NSK ITALIA S.P.A.

MILANO Via Garibaldi 215, Garbagnate Milanese (Milano) 20024, Italy
P: +39-299-5191 F: +39-299-025778

Netherlands:

NSK EUROPEAN DISTRIBUTION CENTRE B.V.

TILBURG De Kroonstraat 38, 5048 AP Tilburg, Netherlands
P: +31-13-4647647 F: +31-13-4647648

Poland:

NSK REPRESENTATIVE OFFICE

WARSAW Ul. Migdalowa 4/73, 02-796, Warsaw, Poland
P: +48-22-645-1525 F: +48-22-645-1529

Russia:

NSK POLSKA SP. Z O.O.

SAINT-PETERSBURG Office I 703, Bldg 29, 18th Line of Vasilievskiy Ostrov, Saint-Petersburg, Russia, 199178
P: +7-812-332-5071 F: +7-812-332-5072

Spain:

NSK SPAIN S.A.

BARCELONA C/Tarragona, 161 Cuerpo Bajo, 2a Planta, 08014, Barcelona, Spain
P: +34-93-289-2763 F: +34-93-433-5776

Turkey:

NSK RULMANLARI ORTA DOGU TIC. LTD. STI.

ISTANBUL 19 Mayis Mah. Ataturk Cad., Ulya Engin Is Merkezi No: 68 Kat. 6, P.K. : 34736,
Kozyatagi-Istanbul, Turkey
P: +90-216-477-7111 F: +90-216-477-7174

United Arab Emirates:

NSK BEARINGS GULF TRADING CO.

DUBAI JAFZA View 19, Floor 24 Office LB192402/3, PO Box 262163, DownTown Jebel Ali,
Dubai, UAE
P: +971-4-804-8207 F: +971-4-884-7227

●North and South America

United States of America:

NSK AMERICAS, INC. (AMERICAN HEADQUARTERS)

ANN ARBOR 4200 Goss Road, Ann Arbor, Michigan 48105, U.S.A.
P: +1-734-913-7500 F: +1-734-913-7511

NSK CORPORATION

ANN ARBOR 4200 Goss Road, Ann Arbor, Michigan 48105, U.S.A.
P: +1-734-913-7500 F: +1-734-913-7511

NSK PRECISION AMERICA, INC.

FRANKLIN ☆ 3450 Bearing Drive, Franklin, Indiana 46131, U.S.A.
P: +1-317-738-5000 F: +1-317-738-5050

SAN JOSE 780 Montague Expressway, Suite 505, San Jose, California, 95131, U.S.A.
P: +1-408-944-9400 F: +1-408-944-9405

NSK LATIN AMERICA, INC.

MIAMI 3470 NW 82nd Avenue Suite 625, Miami FL 33122, U.S.A.
P: +1-305-477-0605 F: +1-305-477-0377

Canada:

NSK CANADA INC.

TORONTO ☆ 5585 McAdam Road, Mississauga, Ontario, Canada L4Z 1N4
P: +1-905-890-0740 F: +1-800-800-2788

MONTREAL 2150-32E Avenue Lachine, Quebec, Canada H8T 3H7
P: +1-514-633-1220 F: +1-800-800-2788

VANCOUVER 3353 Wayburne Drive, Burnaby, British Columbia, Canada V5G 4L4
P: +1-877-994-6675 F: +1-800-800-2788

Argentina:

NSK ARGENTINA SRL

BUENOS AIRES Garcia del Rio 2477 Piso 7 Oficina "A" (1429) Buenos Aires-Argentina
P: +54-11-4704-5100 F: +54-11-4704-0033

Brazil:

NSK BRASIL LTDA.

SAO PAULO ☆ Rua 13 de Maio, 1633-14th Andar-Bela Vista-CEP 01327-905 São Paulo, SP, Brazil
P: +55-11-3269-4700 F: +55-11-3269-4720

BELO HORIZONTE Rua Ceara 1431-4th andar-sala 405-Funcionarios Belo Horizonte-MG, Brazil
30150-311
P: +55-31-3274-2591 F: +55-31-3273-4408

JOINVILLE Rua Blumenau, 178-sala 910-Centro Joinville-SC, Brazil 89204-250
P: +55-47-3422-2239 F: +55-47-3422-2817

PORTO ALEGRE Av. Cristovão Colombo, 1694-sala 202-Floresta Porto Alegre-RS, Brazil 90560 001
P: +55-51-3346-7851 F: +55-51-3222-2599

RECIFE Av. Conselheiro Aguiar, 2738-6th andar-conj. 604-Boa Viagem Recife-PE, Brazil 51020-020
P: +55-81-3326-3781 F: +55-81-3326-5047

Peru:

NSK PERU S.A.C.

LIMA Av. Enrique Palacios, N 360 Oficina 311, Miraflores, Lima, Perú
P: +51-1-652-3372 F: +51-1-638-0555

Mexico:

NSK RODAMIENTOS MEXICANA, S.A. DE C.V.

MEXICO CITY ☆ Av. Presidente Juarez No.2007 Lote 5, Col. San Jeronimo Tepetlacalco,
Tlalnepantla, Estado de Mexico, Mexico, C.P.54090
P: +52-55-3682-2900 F: +52-55-3682-2937

MONTERREY Av. Ricardo Margain 575, IOS Torre C, Suite 516, Parque Corporativo Santa
Engracia, San Pedro Garza Garcia, N.L. Mexico, C.P.66267
P: +52-81-8000-7300 F: +52-81-8000-7095

<As of February 2017>
For the latest information, please refer to the NSK website.
www.nsk.com

NSK Ltd. has a basic policy not to export any products or technology designated as controlled items by export-related laws. When exporting the products in this brochure, the laws of the exporting country must be observed. Specifications are subject to change without notice and without any obligation on the part of the manufacturer. Every care has been taken to ensure the accuracy of the data contained in this brochure, but no liability can be accepted for any loss or damage suffered through errors or omissions. We will gratefully acknowledge any additions or corrections.

Motion & Control

No. 28 June 2017

Published by NSK Ltd.

Eco-awareness and reliability in motion

NSK used environmentally friendly printing methods for this publication.

CAT. No. ETJ-0028 2017 C-6 Printed in Japan